공학박사 학위논문

Development of TAPINS Code for Thermal-hydraulic Analysis of Integral Pressurized Water Reactor, REX-10

일체형 가압경수로 **REX-10**의 열수력 해석을 위한

TAPINS 코드 개발

2013 년 **2** 월

서울대학교 대학원

에너지시스템공학부

이 연 건

Development of TAPINS Code for Thermal-hydraulic Analysis of Integral Pressurized Water Reactor, REX-10

일체형 가압경수로 **REX-10**의 열수력 해석을 위한
TAPINS 코드 개발

지도교수 김 응 수

이 논문을 공학박사 학위논문으로 제출함
2012 년 10 월

서울대학교 대학원
에너지시스템공학부
이 연 건

이연건의 박사 학위논문을 인준함
2012 년 12 월

위 원 장	이 은 철	**(인)**
부위원장	김 응 수	**(인)**
위　　원	주 한 규	**(인)**
위　　원	박 군 철	**(인)**
위　　원	정 영 종	**(인)**

Abstract

Development of TAPINS Code for Thermal-hydraulic Analysis of Integral Pressurized Water Reactor, REX-10

Yeon-Gun Lee

Department of Energy System Engineering

The Graduate School

Seoul National University

REX-10 is a small pressurized water reactor with integral design to provide the small-scale electricity generation and the nuclear district heating. It is a fully-passive small modular reactor (SMR) in which the coolant flow is driven by natural circulation, the RCS is pressurized by the steam-gas pressurizer, and the decay heat is removed by the PRHRS. To confirm design decisions and analyze the transient responses of an integral PWR such as REX-10, a thermal-hydraulic system code named TAPINS (Thermal-hydraulic Analysis Program for INtegral reactor System) is developed in this study. The TAPINS is verified and validated with various benchmark problems and experiments, including the integral effect tests (IETs) performed in a scaled apparatus of REX-10.

The TAPINS basically consists of mathematical models for the reactor coolant

system, the core, the once-through helical-coil steam generator, and the built-in steam-gas pressurizer. The TAPINS hydrodynamic model is a one-dimensional four-equation drift-flux model which takes into account the non-equilibrium effect of two-phase flow phenomena. In particular, a dynamic model of the steam-gas pressurizer to estimate the transient behavior of pressurizer containing the non-condensable gas is suggested in this study and incorporated into the TAPINS. The TAPINS includes the proper heat transfer coefficient correlations and the heat conduction model to predict the time-dependent heat transport in a fully-passive integral reactor. The field equations are discretized by the semi-implicit finite-difference scheme on the staggered grid meshes to assure the numerical stability and the fast computation speed. The difference equations are solved by using the Newton Block Gauss Seidel (NBGS) method in which the fundamental unknowns are determined from 5×5 linear matrix for each mesh cell.

Various steady-state and transient analyses are carried out for verification and validation of the TAPINS. The TAPINS is verified by the simple mass and energy conservation problem and the natural circulation problem. The validation works are performed with experiments on the pressurizer insurge transients, subcooled boiling, critical flow, and pipe blowdown. To generate the IET data for code validation, an experimental program is conducted in the RTF (REX-10 Test Facility) which is a scaled-down integral facility of REX-10 by 1/50. The TAPINS calculation results are compared to the test data on the steady-state natural circulation, core power transients, and loss-of-feedwater event conducted in the RTF. In addition, the TAPINS is applied to the thermal-hydraulic simulation of the reference reactor, REX-10. The transient behaviors of REX-10 when encountered to a reactivity insertion accident and an increase in feedwater flow event are

predicted by the TAPINS and compared to results from the TASS/SMR.

From the V&V results, it is revealed that the TAPINS can provide the reliable prediction on thermal-hydraulic phenomena in an integral reactor on natural circulation. In particular, the TAPINS can contribute to an improved prediction on the non-equilibrium effect of two-phase flow and the transient response of the steam-gas pressurizer.

Keywords

REX-10, Fully-passive integral PWR, TAPINS code, Drift-flux model, Steam-gas pressurizer model, RTF (REX-10 Test Facility), Code V&V

Student Number: 2007-21260

List of Contents

List of Tables

List of Figures

Chapter 1

Introduction

1.1 Background and Motivation

1.1.1 Integral Pressurized Water Reactors

The substantial amount of R&D that has been carried out on SMRs around the world reveals the strong desire for an innovative and reliable nuclear system. Moreover, the application range of these nuclear reactors is no longer restricted to electricity generation. As a flexible and cost-effective energy alternative, SMRs have become one of the preferred options for non-electrical applications such as seawater desalination, ship propulsion, heat supply stations and so on. The most promising SMR candidates to be deployed include B&W mPower, NuScale, Westinghouse SMR, and SMART as shown in Fig 1.1 (OECD/NEA, 2011). The currently available advanced SMRs are listed in Table 1.1 (IAEA, 2011).

Note that most of these upcoming SMRs employ an integral layout of the reactor coolant system; all major components such as core, pressurizer, steam generator are housed in the reactor pressure vessel. Besides its multi-purpose applicability, the integral reactor is favorable in terms of safety as the possibility of system depressurization is lowered by localizing the radioactive coolant in one reactor vessel (IAEA, 1995). Since no large primary penetrations of the reactor vessel or large loop piping exist in an integral pressurized water reactor (iPWR), the potential risk arising from the large-break loss-of-coolant-accident (LBLOCA) is eliminated by design.

It is broadly true that the nuclear societies have focused on the numerical and experimental studies of thermal-hydraulics on a loop-type large-scale nuclear power plant (NPP). Accordingly, a thermal-hydraulic system code and an integral effect test for integral PWRs are rarely found. Most studies on an integral PWR have been biased toward the conceptual or preliminary design and the numerical analyses using conventional system codes. Though major concepts of integral PWRs are based on the proven technologies from conventional ones, it is required to establish an analysis system to assess the design decisions and simulate RCS responses of integral PWRs as well as figure out the major thermal-hydraulic phenomena and the safety features related with the new reactors.

1.1.2 Thermal-hydraulic System Code for Integral PWR

In describing the thermal-hydraulic behavior of an integral PWR, one may use commercial system codes such as RELAP5 (Ransom et al., 2001a), RETRAN-3D (Paulsen et al., 1998), and CATHARE (Emonot et al., 2011), which have reached a high degree of maturity through extensive qualifications. However, these generic codes do not always incorporate the mathematical models for system components of integral PWRs. In practice, the RELAP5 and RETRAN-3D do not have the models of a helically coiled steam generator and an in-vessel pressurizer with a non-condensable gas, respectively. In addition, it is not easy for users to modify and supplement the required models in the source codes due to their complex structures.

Uncertainty of these generic computational tools based on the best-estimate approach is another issue steadily raised. Notwithstanding the huge amounts of financial and human resources invested, the results predicted by the conventional codes are still affected by errors (Petruzzi and D'Auria, 2008). A typical problem is associated with user effect (Askan et al., 1993). The code user has to build up a detailed noding diagram which maps the whole system to be calculated into the frame of a one-dimensional thermal-hydraulic network. Furthermore, a large number of options available to select appropriate models, correlations or specific multipliers have to be chosen by user. This "open strategy" for flexibility in the thermal-hydraulic simulations passes much responsibility to the code user, causing considerable uncertainties in the prediction results by the major existing system codes with high generality. If one develops a system code optimized for a specific type of reactor, the uncertainty arising from user effect can be reduced.

A thermal-hydraulic system code specifically for an integral reactor is hardly found. One exception is the TASS/SMR code developed by Korea Atomic Energy Research Institute (KAERI). It is a system analysis code to simulate all relevant thermal-hydraulic phenomena in the RCS during operational transient and design basis accident of SMART (Chung et al. 2012). In order to simulate the design characteristics of SMART, the TASS/SMR incorporates relevant specific models such as the helical-coil steam generator model and the condensate heat exchanger model in the passive residual heat removal systems (PRHRS). The TASS/SMR adopts four governing equations on the mass, momentum and energy conservation of mixture, and the mass conservation of non-condensable gas. However, since the field equation of the TASS/SMR is based on the homogeneous equilibrium model (HEM), there may be some restrictions on some transients in which the non-homogeneous or non-equilibrium effects are dominant.

1.1.3 IET Facility for Integral PWR

For the loop-type reactor, the nuclear society has been accumulating much experience in design and operation of a conventional PWR, with conducting the large-scale IETs to assess the safety of NPPs in the process. For the conventional PWR, more than fifteen IET have been performed around the globe, including LOFT, BETHSY, Semiscale and so on. These IET are essential to model the nuclear and thermal-hydraulic phenomena on transient and accidental situations.

On the other hand, the experimental program for an integral PWR is quite uncommon. The features of the representative IET facilities for an integral PWR are listed in Table 1.2. VISTA (Experimental Verification by Integral Simulation of Transients and Accidents) is to experimentally verify the system design and performance of the SMART-P (Choi et al., 2006). Scaling ratios are 1:1 in height and 1:96 in volume with respect to the SMART-P. Even though the VISTA is an IET facility for the integral reactor, note that the major components in the primary system are connected by loop piping for easy installation of instrumentation and simple maintenance. The VISTA encompasses the gas pressurizer in which high concentration of nitrogen gas is maintained in upper volume.

OSU MASLWR is an IET facility scaled to model the steady-state and the transient operation of the MASLWR under full pressure and full temperature conditions and to assess the passive safety systems under transient conditions

(Reyes et al., 2007). It is scaled at 1:3 length scale, 1:254 volume scale and 1:1 time scale. The OSU MASLWR has an integral RCS configuration and the core flow is driven by natural circulation. The pressurizer of the OSU MASLWR is the conventional steam pressurizer equipped with internal heaters. Most of testing programs officially reported are to investigate the blowdown transients caused by an inadvertent actuation of the automatic depressurization system (ADS).

Besides, KAERI and Babcock & Wilcox are building the integral test facilities named SMART-ITL and IST, respectively, but the fully-fledged testing programs are yet to begin. Note that both the VISTA and the OSU MASLWR are the scaled facility of an integral reactor equipped with an active system even for normal operation. The SMART-P utilizes the reactor coolant pump (RCP) for the forced convection of the coolant, and the MASLWR regulates the system pressure by controlling the heaters in the pressurizer. That is, the conventional IETs on an integral reactor cannot provide the proper data for the integral PWRs operated in the passive way. Therefore, one has to perform extensive IETs to substantiate the new concepts the RCS behavior of an integral reactor operated in a passive manner and produce code validation data for iPWR.

1.2 Description of REX-10

REX-10 is a small integral-type PWR suggested by Seoul National University (SNU). The aim of the REX-10 development program is to achieve a more stable, efficient, area-independent system operation and energy production (Lee et al., 2012). The design goals of REX-10 include implementing high levels of inherent safety into the reactor design to enhance the public acceptance of an innovative system, and attaining non-proliferation during all processes of construction and operation. In particular, much emphasis is placed on the assurance of passive safety features for REX-10 at the design stage. The schematic diagram of REX-10 is depicted in Fig. 1.2.

REX-10 is designed to generate the rated output of 10 MW at a low pressure (2.0 MPa) compared to conventional reactors. It is an integral-type small PWR which contains the primary components inside the reactor vessel. This layout eliminates the possibility of system depressurization by LBLOCA by virtue of the absence of large-diameter pipelines. In addition, as the coolant circulates by gravity-driven free convection without a RCP, all safety issues associated with the failure of the RCP can be eliminated.

The major design parameters of REX-10 are listed in Table 1.3. A cylindrical reactor vessel with a height of 5.715 m houses the core, CRDM, pressurizer, and steam generator. Placed at the bottom of the reactor pressure vessel are the 9×9 heterogeneous Th/UO_2 fuel assemblies that are used to achieve an ultra-long fuel cycle of up to 20 years on the basis of the Seed-Blanket Unit (SBU) design. This thorium-based fuel has a major benefit in aspect of the intrinsic proliferation resistance since ^{232}U, formed along with the bred ^{233}U, and its daughter isotopes emit intensive alpha and gamma radiation, hindering the access to nuclear fuel. A total of 37 assemblies with an active height of 0.8 m are composed of fuel bundles enriched to 20 w/o. In REX-10, the intrinsic feedback capability is enhanced by refusal from soluble boron control, while excess reactivity is dealt with by burnable poison and control rods. The long riser region above the core provides sufficient head for the free convection of fluid.

The gaseous mixture volume in the upper part of the reactor pressure vessel above the coolant level is referred to as the built-in steam-gas pressurizer. It is the most distinguishing component of REX-10 and represents the progress in incorporating passive features into the integral reactor system (Lee et al., 2009). In normal operation, the saturation vapor corresponding to the temperature of the hot fluid in RCS is maintained in the gas region by establishing the dynamic equilibrium with liquid region, and mixed with the non-condensable gas like nitrogen. The once-through steam generator of REX-10 consists of helical tubes wrapped around the entire annulus between the core barrel and the reactor pressure vessel. The primary coolant flows downward across the tube bundles to evaporate the coolant on the tube-side. Flowing in the opposite direction, the secondary feedwater enters into the helical coil in a subcooled state; by the time it leaves the coil, it has turned into saturated steam.

The containment of REX-10 is filled with water and buried underground. The large amount of water in the containment can serve not only as a barrier against the release of radioactive material from the reactor system but also as a heat sink under accident conditions (Lim, 2010). Engineered safety systems of REX-10 are illustrated in Fig. 1.3. As a representative safety system prepared for REX-10, the PRHRS removes the decay heat in the event of reactor shutdown. Automatically put into action by the trip signal, the PRHRS condenses vapor from the steam generator by means of natural circulation through a heat exchanger, which is located higher than the S/G and submerged in the water of containment building.

1.3 Objectives and Scope

The objectives of this study are to develop a system analysis code for thermal-hydraulic simulation of integral reactors and perform code V&V. REX-10, which is an object of interest in this study, is a fully-passive integral PWR in which the coolant flow is driven by natural circulation, the system pressure is regulated by a built-in pressurizer with non-condensable gas, and the decay heat is removed by the actuation of PRHRS after reactor shutdown. The thermal-hydraulic system code is developed for verification of the reactor design and the safety performance of REX-10. As a unique contribution of this study, a dynamic model of the steam-gas pressurizer is newly proposed and incorporated into the developed code for better prediction on the transient response of the pressurizer in the presence of the non-condensable gas. A series of IET are conducted in a scaled apparatus of REX-10 and the produced unique data are used for code validation. The outline of this study is described in Fig. 1.4. The research scopes are summarized as follows:

Development of TAPINS: A system analysis code named TAPINS (Thermal-hydraulic Analysis Program for INtegral reactor System) is developed to assess the design decisions and predict transient behaviors of integral PWRs. On the basis of the four-equation drift-flux model, the numerical solver of governing equations is programmed using the semi-implicit difference scheme. Component modeling is also carried out to predict the transient performance of major system components. A dynamic model for the steam-gas pressurizer is newly proposed to predict the pressurizer responses in the presence of non-condensable gas, and the numerical solution method for the pressurizer model is suggested. In addition, the heat transfer package for the shell-side and tube-side of the helical-coil steam generator as well as the heat conduction model for tube bundles are established. The incorporated hydrodynamic models of the TAPINS are applied to the thermal-hydraulic phenomena of importance: natural circulation, saturated or subcooled boiling heat transfer, blowdown, chocked flow, core reactivity feedback and so forth.

IET in RTF (REX-10 Test Facility): A series of experiments are performed in a scaled apparatus of REX-10 named RTF. The RTF is specially equipped with the steam-gas pressurizer which maintains nitrogen in the gaseous mixture. Not only the change in core power transients but also the design basis accidents of integral reactors including the LOFW (loss-of-feedwater) event are experimentally investigated. The generated data from this IET program are used to validate the TAPINS.

TAPINS verification and validation: In order to confirm the applicability of the TAPINS for integral PWRs, the code V&V is conducted with a couple of benchmark problems and experiments. The TAPINS is verified with the mass and energy conservation problem and the natural circulation problem. The assessment matrix for code validation is prepared, ranging from the simple steady-state boiling tests to the integral test problem investigated in this study. The prediction results of the TAPINS are compared with the experimental data. For some of the validation problems, the calculation results of the TASS/SMR are also used for comparison so that the characteristics of the TAPINS can be exhibited. From the comparison results, it is verified whether the TAPINS can provide reliable prediction on the performances and the transients of REX-10 on natural circulation.

Chapter 2 presents the hydrodynamic models of the TAPINS, including the field equations, constitutive relations and component models. In Chapter 3, the numerical solution method of the TAPINS is described. The code verification and validation results are covered in Chapter 4, with particular emphasis on the IETs performed in this study. The selected analysis results for the prototypical REX-10 are provided in Chapter 5.

Table 1.1 Currently available advanced SMRs

SMR	Reactor Type	Designer, Country	Output, MWe
KLT-40S	PWR	OKBM Afrikantov, Russia	35×2
CAREM	Integral PWR	CNEA, Argentina	27
SMART	Integral PWR	KAERI, Republic of Korea	100
NuScale	Integral PWR	NuScale Power Inc., USA	45×12
mPower	Integral PWR	B&W, USA	180×2
Westinghouse SMR	Integral PWR	Westinghouse, USA	225
IMR	Integral PWR	MHI , Japan	350
AHWR	PHWR	BARC, India	284
4S	Na cooled FR	Toshiba, Japan	10
HPM	Pb-Bi cooled FR	HPG Inc., USA	25×N

Table 1.2 IET facilities for integral PWR

	RTF	VISTA	OSU MASLWR
Institute	SNU (Korea)	KAERI (Korea)	OSU (USA)
Reference Rx.	REX-10	SMART-P	MASLWR
Scaling ratio (H/V)	1:1 / 1:50	1:1 / 1:96	1:3 / 1:254
Type of circulation	Natural	Forced	Natural
Configuration	Integral RCS	Loop-type RCS	Integral RCS
Full pressure	2.0 MPa	14.7 MPa	11.4 MPa
Pressurizer type	Steam-gas PRZ	Gas PRZ	Steam PRZ
S/G type	Helical coil S/G	Helical coil S/G	Helical coil S/G
Main focusing	SBLOCA & LOFW	PRHRS	ADS blowdown

Table 1.3 Major design parameters of REX-10

Parameters	Design Value
General information	
Reactor type	Integral PWR
Reactor power (MW)	10
Service years (yr.)	20
Reactor coolant system	
Cooling mode	Natural circulation
Operating pressure (MPa)	2.0
Design pressure (MPa)	3.0
Core inlet / outlet Temp. (^{o}C)	165.0 / 200.0
Mass flow rate (kg/s)	64.9
Fuel and reactor core	
Fuel type	9×9 Square FA
Fuel material	Hetero Th/UO_2
No. of fuel assembly	37
No. of fuel rods (/FA)	72
Effective height (m)	0.8
Steam generator	
Type	Helical coil HX
Feedwater mass flow (kg/s)	4.47
Feedwater temperature(^{o}C)	120.0
Steam temperature (^{o}C)	142.0 (sat. steam)
Steam pressure (MPa)	0.4
Reactor Vessel and Pressurizer	
Vessel outer diameter (m)	2.272
Core barrel diameter (m)	1.607
Vessel height (m)	4.588+1.127 (PRZ)
Pressurizer type	Steam-gas PRZ
Non-condensable gas	Nitrogen

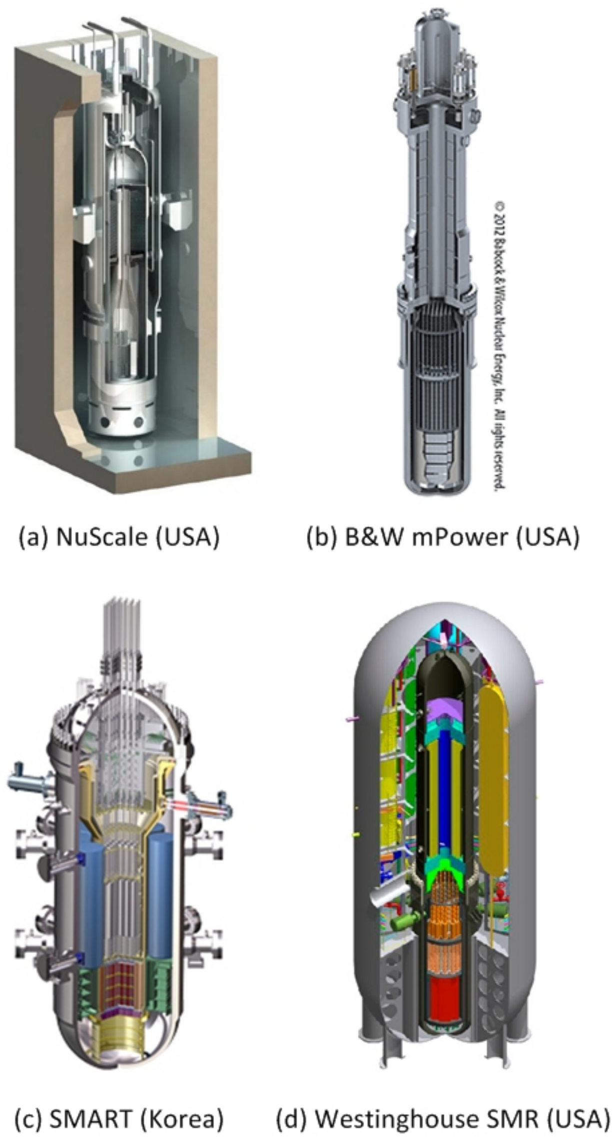

Figure 1.1 Integral-type SMRs

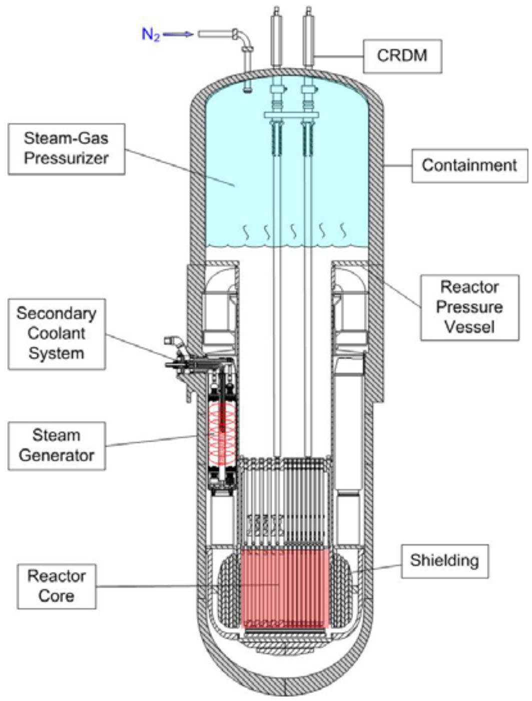

Figure 1.2 Schematic diagram of REX-10

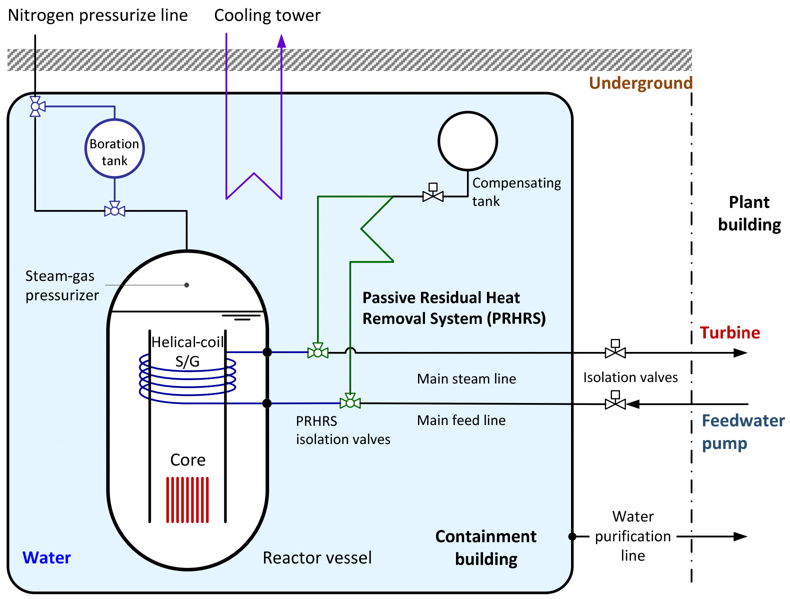

Figure 1.3 Engineered safety systems of REX-10

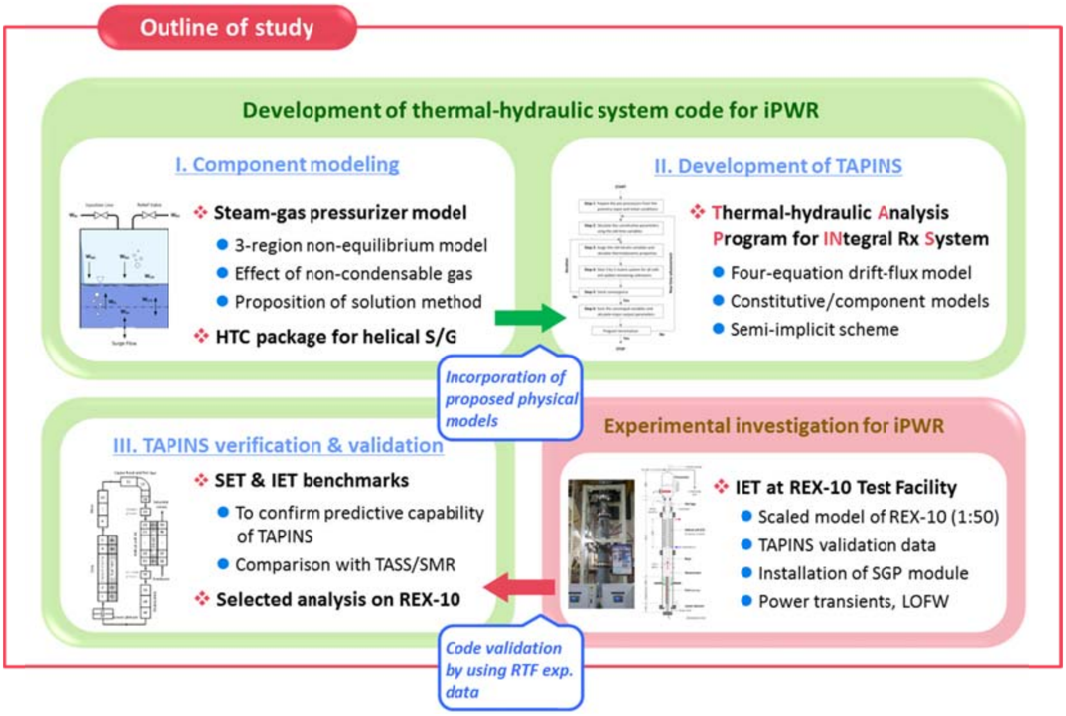

Figure 1.4 Outline of the study

Chapter 2

Hydrodynamic Models of TAPINS

2.1 Code Design

To estimate the transient behavior of integral PWRs under during off-normal conditions, a thermal-hydraulic system code named TAPINS is developed in this study. When developing a thermal-hydraulic analysis code, one has to design the fundamental concept and frame of code prior to programming the software. Then proper models and correlations required for the code can be determined. As stated above, the analysis object of the research herein is a fully-passive integral PWR in which, in a passive manner, the reactor is normally operated and the accidents are mitigated as well. The TAPINS code is designed so that the safety performance and the transient behaviors of the fully-passive integral PWR can be simulated. Figure 2.1 describes the procedure of designing the fundamental frame of the TAPINS in this study.

The reference reactor typifying fully-passive integral PWRs is set to REX-10 in this study. The reactor transients of interest encompass not only those caused by the changes in core power or the variation of the heat transport in the helical-coil S/G and so on, but also the design basis accidents (DBAs) of integral PWRs. By design, these integral reactors can eliminate the occurrence of the LBLOCA arising from the rupture of a large pipeline penetrating through the reactor pressure vessel. However, the loss-of-feedwater accident, in which the heat removal by the secondary system completely vanishes, is a feasible event to threat the safety of integral PWRs. In addition, the break occurred at the small pipeline connected to the pressurizer vessel, such as the nitrogen injection line, may result in the hypothetical discharge of coolant and the system depressurization. In this study, therefore, the final analysis scope is set to LOFW and SBLOCA of integral PWRs. The thermal-hydraulic phenomena expected in these DBAs of an integral reactor include: natural circulation, vapor generation caused by subcooled boiling or blowdown, transient heat transport in the helical-coil S/G, pressure response of the steam-gas pressurizer to surge flow, chocked flow and so on.

In selecting the hydrodynamic model, the principle is that one should choose the least complicated model which accommodates the phenomena of interest (Wulff, 1992). Unlike the conventional NPPs where long horizontal pipelines are located outside the reactor pressure vessel, the primary system of integral PWRs mostly consist of vertical channels. Thus, the four-equation drift-flux model is selected as field equations of the TAPINS since it can take into account the non-equilibrium effects of two-phase flow and provide highly accurate prediction for a vertical channel, especially in bubbly and slug flow regimes. Then the constitutive relations for two-phase flow regime map, interfacial heat transfer coefficient, wall friction, and drift velocity have to be established for closure. A critical flow model to calculate the discharge rate through a rupture is also required.

For thermal-hydraulic analyses of integral PWRs, the mathematical models for major system components typified by the core, the steam-gas pressurizer, and the helical-coil S/G are also needed. Since the multi-dimensional power profile is not essential, the point kinetics model, which is the simplest dynamic model for neutronics, seems to be appropriate in calculating the time-dependent core power in conjunction with the convective heat transfer coefficients for heat transport into coolant. To predict the effect of non-condensable gas on the pressure response of integral PWRs, a dynamic model for the steam-gas pressurizer is also required. In addition, the heat transfer package for the shell-side and the tube-side of helically-coiled tubes according to boiling regions has to be employed.

2.2 Features of TAPINS

One can define the TAPINS as a one-dimensional analysis code specified for passive integral PWRs on natural circulation. As aforementioned, the scope of code is determined from the requirement that the TAPINS should have predictive capability for DBAs of integral PWRs, which are investigated in the experimental works in this study. By developing the analysis code optimized for an integral reactor, the uncertainty arising from user effect is expected to be greatly reduced as well.

It has to be clarified that prior mission is to develop an easy-to-use and fast-running system code for integral reactors. The system code for integral PWRs has to essentially deal with the solution of the balance equations for the steam-liquid two-phase mixtures supplemented by the constitutive correlations to cover the range of parameters expected in the reactor of interest. The TAPINS basically consists of mathematical models for the basic conservation laws of fluid and the special components in an integral PWR. Especially, the modeling of new integral components such as the once-through steam generator and the built-in pressurizer, which serves as the main computational challenges in the analyses of an integral reactor, is carried out, and the developed models are incorporated into the code. The TAPINS is written in FORTRAN 90 and easily executed on a PC. Its code architecture supports the optimal calculation for reactor systems with the integral configurations.

Code structure of the TAPINS is depicted in Fig. 2.2. The TAPINS consists of a couple of large blocks divided by the function in the calculation. The subroutine **InpReader** reads all data from the input file and checks for some probable errors. From the stored data, the subroutine **SetSys** prepares the pre-processors required to the computation by defining the fundamental variables for the core and S/G and allocating the geometric data to the dynamic arrays. The temperature distribution of the primary circuit is initialized and the steady-state heat conduction solution is found for the fuel rods and the S/G helical tubes in the subroutine **IniCndtn**. The subroutine **Hydromod** is the main module of the TAPINS to facilitate solution of transient problems. It contains the subroutines to advance the solutions for the reactor kinetics, the hydrodynamic model, the helical coil S/G model, the steam-gas pressurizer model, the heat conduction equations and so on. Various constitutive relations support to solve the hydrodynamic model, including the state relationships, the vapor generation model, the wall friction correlation, etc.

In developing the TAPINS, significant emphasis is placed on achieving user convenience in preparing the input file for practical applications. It intends to minimize the engineering labor and time required to write the input by reducing, if possible, the number of input data fields which must be filled in by the user. When performing a simulation of a nuclear system, one can easily encounter a situation where a component or section is divided into a framework of equidistant nodes. In that case, depending on the kind of system code, the user may be required to enter the same figures repeatedly, as many times as the number of nodes.

On the other hand, the input module of the TAPINS divides the RCS of the integral reactor into six subsections: core, riser, upper head, helical-coil steam generator, downcomer, and lower plenum. By receiving only the number of nodes for each subsection, the TAPINS can nodalize them with geometrically identical control volumes, if the user chooses this option for convenience, and perform automatic node numbering. This indicates that the user can avoid unnecessary repetition in building up the node diagram. Of course, it is possible to assign the detailed input data corresponding to individual nodes for elaborated analyses.

2.3 Field Equations

A general transient two-phase flow problem can be formulated by using a two-fluid model or a drift-flux model, depending on the degree of dynamic coupling between the phases (Ishii, 2010). The two-fluid model is the most generally used model in most major existing thermal-hydraulic system codes. Since the two-fluid model introduces the separate momentum and energy conservation equations for each phase, however, one can be commonly confronted with the difficulties associated with mathematical complication and numerical instabilities caused by improper choice of interfacial interaction terms. On the other hand, in the drift-flux model, the motion of the two-phase mixture is expressed by the mixture momentum equation, and the relative motion between the phases is taken into account by a kinematic constitutive equation. Instead of adopting the separate balance equations for each phase, the drift-flux model describes the dynamics of the two phases in a view of mixture momentum conservation, greatly reducing the difficulties associated with the two-fluid model.

The TAPINS employs the four-equation drift-flux model as field equations. It has been widely reported that the drift-flux model can provide highly accurate predictions on the two-phase phenomena of the bubbly or the slug flow regime in the vertical channels. Unlike the loop-type conventional PWR, almost the whole flow channels in the primary system is vertically oriented in the integral PWR. In addition, since transients associated with the loss of significant amounts of coolant are eliminated by design in integral PWRs, it is expected that the highly voided flow such as annular flow or mist flow is rarely encountered. Thus it is believed that the four-equation drift-flux model is properly applicable to a wide-range of thermal-hydraulic phenomena in an integral PWR.

The four-equation drift-flux field equations for a two-phase mixture consist of two mass conservation equations, one momentum conservation equation, and one enthalpy energy equation. A one-dimensional model is obtained by integrating the three-dimensional model over a cross sectional area and then introducing proper mean values (Hibiki et al., 2003). The average mixture density is given by:

$$\rho_m = (1-\alpha)\rho_l + \alpha\rho_v \tag{2.1}$$

Then, the mixture velocity and the mean mixture enthalpy are weighted by the density as:

$$v_m = \frac{(1-\alpha)\rho_l v_l + \alpha\rho_v v_v}{\rho_m} \tag{2.2}$$

$$h_m = \frac{(1-\alpha)\rho_l h_l + \alpha\rho_v h_v}{\rho_m} \quad (2.3)$$

The vapor drift velocity is defined as the velocity of the dispersed phase with respect to the volume center of the mixture:

$$\overline{V_{gj}} = v_v - j = (1-\alpha)\cdot v_r \quad (2.4)$$

The TAPINS utilized the following forms of four partial differential equations:

Mixture continuity equation

$$\frac{\partial \rho_m}{\partial t} + \frac{\partial}{\partial z}\left(\rho_m v_m\right) = 0 \quad (2.5)$$

Vapor mass conservation equation

$$\frac{\partial}{\partial t}\left(\alpha\rho_v\right) + \frac{\partial}{\partial z}\left(\alpha\rho_v v_m\right) + \frac{\partial}{\partial z}\left[\frac{\alpha\rho_v\rho_l v_r}{\rho_m}\right] = \Gamma_g \quad (2.6)$$

Mixture momentum equation

$$\frac{\partial}{\partial t}\left(\rho_m v_m\right) + \frac{\partial}{\partial z}\left(\rho_m v_m^2\right) + \frac{\partial}{\partial z}\left[\frac{\alpha\rho_v\rho_l}{(1-\alpha)\rho_m} v_r{}^2\right] = -\frac{\partial P}{\partial z} - \rho_m g_z - \frac{f_m}{2D}\rho_m v_m \left|v_m\right| \quad (2.7)$$

Mixture enthalpy-energy equation

$$\begin{aligned}\frac{\partial}{\partial t}\left(\rho_m h_m\right) + \frac{\partial}{\partial z}\left(\rho_m h_m v_m\right) + \frac{\partial}{\partial z}\left[\frac{\alpha\rho_v\rho_l}{\rho_m}\Delta h_{gf} v_r\right] \\ = \frac{q_w^{"}\xi_h}{A} + \frac{\partial P}{\partial t} + \left[v_m + \frac{\alpha(\rho_l - \rho_v)}{\rho_m} v_r\right]\frac{\partial P}{\partial z}\end{aligned} \quad (2.8)$$

In the above field equations, the covariance terms, the normal components of the stress tensor in the axial direction, and the mixture-energy dissipation terms are not included since they are negligible. Note that this model can accommodate the non-equilibrium effect by incorporating the mass conservation equation for the vapor which accounts for the rate of phase change. The vapor generation rate due to phase change is expressed as (Ransom et al., 2001a):

$$\Gamma_g = \Gamma_{ig} + \Gamma_w = -\frac{H_{ig}(T_s - T_v) + H_{if}(T_s - T_l)}{h_v^* - h_l^*} + \Gamma_w \qquad (2.9)$$

In addition, the effects of the mass, momentum, and energy diffusion associated with the relative motion between the phases appear explicitly in terms of the drift velocity.

For closure of the field equations, the constitutive relations are needed for wall heat source, wall friction, relative velocity between the phases, and the vapor generation rate as well as the equation of state as presented in Chapter 2.3.

2.4 Constitutive Relations

2.4.1 State Relationships

To make a mathematically complete set with the four field equations and the constitutive relations, the equation of state for each phase is also needed. In the TAPINS, the vapor phase is assumed saturated, and density, temperature, and other saturation properties are called from the steam table (PROPATH GROUP, 2001) in terms of the pressure and the phasic enthalpy as:

$$\rho_l = \rho_l(P,\ h_l) \qquad (2.10)$$

$$T_l = T_l(P,\ h_l) \qquad (2.11)$$

$$\rho_v = \rho_v^s(P) \tag{2.12}$$

$$T_v = T^s(P) \tag{2.13}$$

$$T_s = T^s(P) \tag{2.14}$$

In the numerical scheme employed in the TAPINS, all unknowns appearing in the difference equations, except for the primitive variables, are expressed as the functions of the independent state variables. For the linearized definition, several state derivatives are used in the numerical scheme. All the desired first derivatives of thermodynamic properties are derived from the Bridgman's table (1961) in terms of the isobaric specific heat, the volumetric coefficient of expansion and the isothermal compressibility expressed as:

$$C_p = \left(\frac{\partial h}{\partial T}\right)_P \tag{2.15}$$

$$\beta_P = \frac{1}{\upsilon}\left(\frac{\partial \upsilon}{\partial T}\right)_P \tag{2.16}$$

$$\beta_T = -\frac{1}{\upsilon}\left(\frac{\partial \upsilon}{\partial P}\right)_T \tag{2.17}$$

The required first partial derivatives are given by:

$$\left(\frac{\partial \rho}{\partial P}\right)_h = \frac{\beta_T}{\upsilon} - \frac{\beta_P(\beta_P T - 1)}{C_p} \tag{2.18}$$

$$\left(\frac{\partial \rho}{\partial h}\right)_P = -\frac{\beta_P}{C_p \upsilon} \tag{2.19}$$

$$\left(\frac{\partial h}{\partial P}\right)_T = \upsilon(1 - \beta_P T) \tag{2.20}$$

$$\left(\frac{\partial h}{\partial T}\right)_P = C_p \tag{2.21}$$

$$\left(\frac{\partial T}{\partial P}\right)_h = \frac{\upsilon(\beta_P T - 1)}{C_p} \tag{2.22}$$

The derivative of saturation temperature with respect to pressure is calculated by the Clasius-Clapeyron equation. The derivatives for vapor, which is in saturated state, are obtained by linear interpolation.

While the vapor phase is assumed saturated in the TAPINS, the liquid can be either subcooled or superheated. The temperature of metastable liquid is obtained by using a Taylor series expansion about the saturation value as:

$$T \approx T^s(P) + \left(\frac{\partial T}{\partial h}\right)_P \left[h - h^s(P)\right] = T^s(P) + \frac{h - h^s(P)}{C_p} \tag{2.23}$$

It is a constant pressure extrapolation. On the contrary, for the specific volume, the extrapolation along a constant temperature line is used for the superheated liquid.

2.4.2 Interphase Heat and Mass Transfer

The thermal non-equilibrium effects are accommodated in the drift-flux model by a constitutive equation for phase change that specifies the rate of mass transfer per unit volume. The vapor generation term appearing in the RHS of Eq. (2.6) consists of the mass transfer due to the interface energy exchange in the bulk and the mass transfer by heat transfer in the thermal boundary layer near the wall. Since the vapor is assumed saturated, Eq. (2.9) is reduced to:

$$\Gamma_g = -\frac{H_{if}(T_s - T_l)}{h_v^* - h_l^*} + \Gamma_w \tag{2.24}$$

Here, the terms in the denominator is as following:

$$h_v^* = h_v^s \tag{2.25}$$

$$h_l^* = \frac{1}{2}\left[\left(h_l^s + h_l\right) - \eta \cdot \left(h_l^s - h_l\right)\right] \tag{2.26}$$

where

$$\begin{aligned} \eta &= \ \ 1 \quad \text{for } \Gamma_{ig} \geq 0 \\ &= -1 \quad \text{for } \Gamma_{ig} < 0 \end{aligned}$$

Thus, the interphase heat transfer coefficient and the mass transfer rate per unit volume near a wall are needed to calculate the rate of phase change.

Since the interphase heat transfer coefficient depends on the two-phase flow regime, the proper flow retime map has to be incorporated into the code. In the TAPINS, both vertical and horizontal volume flow regime map are implemented in the same way as RELAP5. In addition, the interphase heat transfer correlations for liquid employed in the RELAP5 are adopted in the TAPINS as summarized in Table 2.1. The code calculates the coefficients in the interfacial mass transfer in the bulk fluid according to the state of liquid (subcooled or superheated) and the two-phase flow regime. Note that, to prevent the discontinuity or very rapid changes of the interphase heat transfer coefficient, a couple of smoothing techniques are incorporated in the TAPINS.

The mass transfer rate per unit volume near a wall is calculated by the Lahey method (1978) as following:

$$\Gamma_w = \frac{q'' A_w}{V(h_g^{'} - h_f^{'})}\mathrm{Mul} \tag{2.27}$$

The multiplier denotes the fraction of the boiling heat flux which causes steam generation. It is defined as:

$$\mathrm{Mul} = \frac{h_l - h_{cr}}{(h_l^s - h_{cr})(1+\varepsilon)} \tag{2.28}$$

where h_{cr} and ε are the critical enthalpy for net voids and the pumping term, respectively. The critical enthalpy is calculated by the Saha-Zuber correlation (1974) as:

$$\begin{aligned} h_{cr} &= h_l^s - 0.0022\frac{q'' D_h C_{pf}}{k_f} \qquad Pe < 70,000 \\ &= h_l^s - 154\frac{q''}{G} \qquad\qquad\quad Pe > 70,000 \end{aligned} \tag{2.29}$$

The pumping term is defined by:

$$\varepsilon = \frac{\rho_l \left[h_l^s - \min(h_l,\ h_l^s) \right]}{\rho_v h_{fg}} \tag{2.30}$$

The rate of phase change near a wall is calculated only when the positive (boiling) or negative (condensation) heat flux exists.

2.4.3 Wall Friction

In the TAPINS, the Darcy friction factor is computed from correlations for laminar and turbulent flows with interpolation in the transition regime. When the Reynolds number is less than 2200, the laminar friction factor is calculated by:

$$f = \frac{64}{\mathrm{Re}} \tag{2.31}$$

For Re larger than 3000, the turbulent friction factor is given by the Zigrang-Sylvester approximation (1985) to the Colebrook-White correlation as:

$$\frac{1}{\sqrt{f}} = -2\log_{10}\left\{\frac{\varepsilon}{3.7D} + \frac{2.51}{\mathrm{Re}}\left[1.14 - 2\log_{10}\left(\frac{\varepsilon}{D} - \frac{21.25}{\mathrm{Re}^{0.9}}\right)\right]\right\} \tag{2.32}$$

The friction factor in the transition region between laminar and turbulent flows is computed by reciprocal interpolation. The two-phase friction multiplier, which correlates two-phase friction losses to single-phase pressure losses, is calculated either by the homogeneous equilibrium model or Jones' correlation (Todreas and Kazimi, 1990).

2.4.4 Drift Velocity

In the drift-flux model, as aforementioned, the dynamics of the two-phase flow is formulated in terms of the mixture center-of-mass velocity (v_m) and the drift velocity specifying the relative velocity between phases. Since the relative velocity is included in the field equations to take account of the diffusion effect by relative motion between phases, proper selection of the correlation for the drift velocity is of great importance.

In the TAPINS, the Chexal-Lellouche model (1992) is used as a kinematic constitutive equation to predict the drift velocity. The Chexal-Lellouche slip model is applicable for a much wider range of conditions and more detailed in its representation than any other correlations. The model eliminates the need to know the two-phase flow regime. In addition, it is validated against the vast amount of data to cover the co-current or counter-current flows in vertical and horizontal channels. From the Chexal-Lellouche model, not only the distribution parameter (C_0) and the drift velocity but also each phasic velocity can be obtained.

The distribution parameter is expressed as:

$$C_0 = \frac{L}{K_0 + (1-K_0)\alpha^r} \tag{2.33}$$

The drift velocity, to account for the vapor velocity with respect to the volume center of the mixture, is given by:

$$\overline{V_{gj}} = 1.41\left(\frac{\Delta\rho g_z \sigma}{\rho_l^2}\right)^{1/4} C_2 C_3 C_4 C_9 \tag{2.34}$$

The details of the parameters appearing in Eqs. (2.33) and (2.34) are found from the publication of Chexal and Lellouche (1992). Then, from the drift-flux relationships, each phasic velocity can be obtained by:

$$v_v = \frac{C_0 G_m + \rho_l \overline{V_{gj}}}{\rho_l - C_0 \alpha \Delta\rho} \tag{2.35}$$

$$v_l = \frac{G_m - \alpha\left(C_0 G_m + \rho_v \overline{V_{gj}}\right)}{(1-\alpha)\left(\rho_l - C_0 \alpha \Delta\rho\right)} \tag{2.36}$$

Thus, the relative velocity is:

$$v_r = \frac{\rho_m \overline{V_{gj}} - G_m\left(1 - C_0\right)}{(1-\alpha)\left(\rho_l - C_0 \alpha \Delta\rho\right)} \tag{2.37}$$

2.5 Component Models

2.5.1 Point Reactor Kinetics

To determine the time-dependent behavior of the fission power, point kinetics equations with six delayed neutron groups are solved in the TAPINS. By allowing the spatial dependence to be eliminated, the point reactor kinetics yields solutions for the neutron population density and delayed neutron precursor concentrations from this set of coupled ordinary differential equations:

$$\frac{dN(t)}{dt} = \frac{\rho(t) - \beta}{\Lambda(t)} N(t) + \sum_i \lambda_i C_i(t) \tag{2.38}$$

$$\frac{dC_i(t)}{dt} = \frac{\beta_i}{\Lambda(t)} N(t) - \lambda_i C_i(t) \qquad (i = 1, 2, \cdots, 6) \tag{2.39}$$

The change in the reactivity induced by the negative feedback effect is also taken into account. The reactivity feedbacks caused by the variation of the core-averaged fuel element and the coolant temperatures as well as the externally introduced reactivity are of great importance:

$$\rho(t) = \rho_0 + \alpha_{T_f} \left(\overline{T}_f(t) - \overline{T}_{f0} \right) + \alpha_{T_m} \left(\overline{T}_m(t) - \overline{T}_{m0} \right) + \delta\rho_{ext}(t) \tag{2.40}$$

In the core kinetics model of the TAPINS, the neutron kinetics parameters and the reactivity temperature coefficients are given in the input data.

The heat conduction equation is also solved in polar coordinates so that the radial temperature distribution in the fuel rods is determined. With the axial heat conduction neglected, the transient heat transport in fuel elements is represented by a model of a typical fuel rod to obtain the average fuel temperature and the cladding surface temperature. The temperature dependence of the thermal conductivity is explicitly modeled. The boundary conditions for the fuel-cladding gap and the cladding-coolant interface are implemented by supposing a quadratic temperature profile in the vicinity of the boundaries and imposing heat flux continuity. In order to obtain the convective heat transfer rate into the coolant, a correlation suggested by Churchill and Chu (1975b), which is suitable for free convection flows, is used as a default model:

$$Nu = \left\{ 0.825 + \frac{0.387 Ra^{1/6}}{\left[1 + (0.492 / Pr)^{9/16} \right]^{8/27}} \right\}^2 \tag{2.41}$$

For turbulent flow in the range of Re > 10,000, the heat transfer model is replaced by the Dittus-Boelter equation. As a CHF correlation, the empirical correlation proposed by Bowring (1972) is incorporated into the TAPINS. It is derived from the database covering the pressure range of 2 - 190 bar, to which the operational pressure of REX-10 belongs.

2.5.2 Steam-gas Pressurizer

In the steam-gas pressurizer, a certain content of non-condensable gas such as nitrogen is maintained in the gas phase. As the presence of the non-condensable gas provides excess pressure in addition to the partial pressure of steam, the subcooled state can be retained at the core outlet. This excludes the use of active equipment such as a spray or heater for control of the primary system pressure. Located at the upper head region of the reactor vessel, the steam-gas pressurizer can hold larger volume of water and gaseous mixture compared to a conventional separate pressurizer.

In order to predict the dynamic behavior of the primary system pressure, an analytical model for the steam-gas pressurizer is newly proposed in this study. The previous pressurizer models are advanced from the two-region model (Baron, 1973) to the three-region non-equilibrium model (Baek, 1986). However, these models deal with a pressurizer containing only steam in the upper gas region and thus the presence of the non-condensable gas is not coupled with the pressure behavior. Since the non-condensable gas affects not only the intensity of mass diffusions occurring in the pressurizer but also the total pressure responses to the transients, a new model accounting for the effect of non-condensable gas is indispensable.

To analyze the thermal-hydraulic characteristics of the steam-gas pressurizer, Kim et al. (2006) proposed the two-region non-equilibrium concept by extending the pressurizer model of the RETRAN/3D-INT. Kim (2010) also developed the two-region model which includes various local mass transfer models in the presence of non-condensable gas and applied it to his own experiments.

The steam-gas pressurizer model of the TAPINS is the three-region non-equilibrium model based on the basic conservation principles of mass and energy. The pressurizer volume is separated into three distinct regions of the gaseous mixture, the upper and the lower liquid regions, each establishing its own thermodynamic state. By the thermal stratification, the lower liquid region is immediately influenced by surge flow while the upper region, the floating hot liquid layer, stays with little changes in temperature. The following assumptions are made in this model:

(1) All regions in the pressurizer share the same pressure.

(2) The Gibbs-Dalton law is valid for the gas phase.

(3) The gaseous mixture establishes thermal equilibrium, i.e. the temperatures of the steam and the non-condensable gas are the same.

(4) Dissolution of the non-condensable gas in the liquid is negligible.

With regard to mass and energy balance, the model takes into account all the processes of heat and mass transfer that occur between the vapor and liquid phases inside the steam-gas pressurizer, as well as the surge flow from the primary loop. The conservation equations are applied to the steam, non-condensable gas and liquid water. Physical phenomena to be modeled include surge (*su*), rainout (*ro*), flashing (*fl*), inter-region heat and mass transfer (*itr*), and wall condensation (*wc*), as illustrated in Fig. 2.3. The mass conservation equations are:

$$\frac{dM_{l1}}{dt} = W_{su} - W_{fl1} - W_{l12} \tag{2.42}$$

$$\frac{dM_{l2}}{dt} = W_{l12} + W_{fl1} - W_{fl2} + W_{itr} + W_{ro} + W_{wc} \tag{2.43}$$

$$\frac{dM_{stm}}{dt} = W_{fl2} - W_{itr} - W_{ro} - W_{wc} - W_{rv-stm} \tag{2.44}$$

$$\frac{dM_{nc}}{dt} = W_{in} - W_{rv-nc} \tag{2.45}$$

The energy conservation equations are written in terms of the convective energy flows and the mechanical work done as follows:

$$\frac{d}{dt}\left(M_{l1}h_{l1}\right) = W_{su}h_{su} - W_{fl1}h_g - W_{l12}h_{l12} + V_{l1}\frac{dP}{dt} \tag{2.46}$$

$$\frac{d}{dt}\left(M_{l2}h_{l2}\right)=W_{l12}h_{l12}+\left(W_{fl1}-W_{fl2}+W_{itr}\right)h_g+\left(W_{ro}+W_{wc}\right)h_f+V_{l2}\frac{dP}{dt} \tag{2.47}$$

$$\frac{d}{dt}\left(M_{stm}h_{stm}\right)=\left(W_{fl2}-W_{itr}\right)h_g-W_{ro}h_f-\left(W_{wc}+W_{rv-stm}\right)h_{stm}+V_g\frac{dP_{stm}}{dt} \tag{2.48}$$

$$\frac{d}{dt}\left(M_{nc}h_{nc}\right)=W_{in}h_{in}-W_{rv-nc}h_{nc}+V_g\frac{dP_{nc}}{dt} \tag{2.49}$$

Contrary to the conventional pressurizer models, it is noted that terms for the heater or spray do not appear in the conservation equations. The relationship for mass flow rate between liquid regions is obtained from the requirement that the lower liquid volume is fixed as following:

$$W_{l12}=W_{su}-W_{fl1}+\frac{M_{l1}}{\upsilon_{l1}}\left(\frac{\partial\upsilon_{l1}}{\partial P}\frac{dP}{dt}+\frac{\partial\upsilon_{l1}}{\partial h_{l1}}\frac{dh_{l1}}{dt}\right) \tag{2.50}$$

Table 2.2 summarizes the physical models for local phenomena occurring in the steam-gas pressurizer. In particular, special emphasis is placed on the calculation of condensate rate at the wall in the presence of non-condensable gas (Kim et al., 2009). In the condensation model, the total heat transfer coefficient is derived from the heat balance at a liquid film interface, and the heat and mass transfer analogy based on mass approach is applied to calculate the condensation heat transfer coefficient in the diffusion layer and the condensate rate.

The interfacial mass transfer between the liquid and the steam is calculated by the Hertz-Knudsen-Schrage Equation (Schrage, 1953) defined on the basis of the gas kinetic theory as shown in Table 2.2. The dynamic equilibrium is assumed at the saturated pressure of the liquid temperature. The coefficient f denotes the condensation coefficient defined as the ratio of the number of molecules absorbed by the liquid phase to the number of molecules impinging on the liquid phase as described in Fig. 2.4. To apply the equation to the high pressure system such as nuclear reactors, one can refer to the correlation by Finkelstein and Tamir (1976) accounting for the pressure dependency of the condensation coefficient.

The above conservation equations form a system in which the unknowns outnumber the equations by 11 (4 mass, 4 enthalpy, 3 pressure) to 8. Thus one requires three more constitutive relations for closure. One is the Gibbs-Dalton law for the gas phase, which states that the total pressure exerted by the gaseous mixture is equal to the sum of the partial pressures of steam and nitrogen. With respect to time, this can be expressed as:

$$\dot{P} = \dot{P}_{stm} + \dot{P}_{nc} \tag{2.51}$$

Another constraint is the thermodynamic equilibrium condition in the gas phase. The temperatures of steam and nitrogen, determined by their respective partial pressure and enthalpy, are given by the following:

$$T_{stm}(P_{stm}, h_{stm}) = T_{nc}(P_{nc}, h_{nc}) = T_g \tag{2.52}$$

The other relation is the time-dependent pressure equation derived from the constraint on the invariant pressurizer volume with time, which is expressed as:

$$\dot{V}_{sgp} = \dot{V}_{l1} + \dot{V}_{l2} + \dot{V}_g = \sum_j \frac{d}{dt}\left(\upsilon_j \cdot M_j\right) = 0 \tag{2.53}$$

where the specific volume of the gaseous mixture is defined by:

$$\upsilon_g = \frac{V_g}{M_g} = \frac{V_g}{M_{stm} + M_{nc}} = \left(\frac{1}{\upsilon_{stm}} + \frac{1}{\upsilon_{nc}}\right)^{-1} \tag{2.54}$$

Note that the v_g can be described with three independent properties in the equation of state due to the thermal constraint of Eq. (2.52). Substituting the equation of states for the gas and the liquid into Eq. (2.53) and rearranging them with respect to the time derivative of pressure yields:

$$\frac{dP}{dt}=-\frac{\sum_j\left(\upsilon_j\cdot W_j\right)+\sum_k\left(\frac{\partial\upsilon_{lk}}{\partial h_{lk}}\cdot WH_{lk}\right)+\xi_g}{\sum_k\left(M_{lk}\cdot\frac{\partial\upsilon_{lk}}{\partial P}+V_{lk}\cdot\frac{\partial\upsilon_{lk}}{\partial h_{lk}}\right)+\eta_g} \tag{2.55}$$

where

$$\xi_g=M_g\left[\dot{P}_{nc}\left(\frac{\partial\upsilon_g}{\partial P_{nc}}-\frac{\partial\upsilon_g}{\partial P_{stm}}\right)+\frac{1}{M_{stm}}\frac{\partial\upsilon_g}{\partial h_{stm}}\left(WH_{stm}-V_g\dot{P}_{nc}\right)\right]$$

$$\eta_g=M_g\frac{\partial\upsilon_g}{\partial P_{stm}}+V_g\frac{\partial\upsilon_g}{\partial h_{stm}}\frac{M_g}{M_{stm}}$$

$$WH_k=\left(\sum_i W_{in,i}h_i-\sum_j W_{out,j}h_j\right)_k-W_k h_k$$

The variation of the water level is advanced from the time derivative of the total liquid volume as following:

$$\frac{dL_l}{dt}=\frac{1}{A_l}\sum_k\left(M_{lk}\cdot\left(\frac{\partial\upsilon_{lk}}{\partial P}\frac{dP}{dt}+\frac{\partial\upsilon_{lk}}{\partial h_{lk}}\frac{dh_{lk}}{dt}\right)+\upsilon_{lk}W_{lk}\right) \tag{2.56}$$

2.5.3 Helical-coil Steam Generator

The precise prediction of heat transport in the helical-coil steam generator is of great importance, especially for free convection flow in an integral system such as REX-10, since the cooling capability of the S/G predominantly affects the stabilized temperature of the primary coolant as well as the transient behavior of

RCS. The steam generator model in the TAPINS calculates the shell-side and the tube-side heat transfer coefficients for helically-wound tubes. The heat transfer on the tube-side is estimated using a single helical coil and the effective heat transfer regions of both sides are composed of the same number of nodes. The heat transfer regions inside the tubes are divided into economizer, evaporator and superheater sections. Similar heat transfer and friction factor models to those used by Yoon et al. (2000), which are employed for the thermal-hydraulic design of a once-through steam generator in SMRAT, are incorporated in the TAPINS with slight modifications.

The empirical correlations for the helical-coil S/G in the TAPINS are summarized in Table 2.3. To predict the transient heat transport from the primary to the secondary circuit, the heat conduction equation has to be solved with suitable tube-side and shell-side heat transfer coefficients needed to implement boundary conditions for convective flows.

For the tube-side, the secondary coolant suffers every boiling region as it changes from the subcooled water to the saturated or superheated vapor. The heat transfer coefficient by single-phase liquid or vapor is obtained by Mori-Nakayama correlation (1967). For the evaporator region, Chen correlation (1963) is used to calculate heat transfer coefficient for saturated nucleate boiling. From the experimental investigation of Kozeki (1970), it is suggested that the dryout occurs inside the helical coil when the steam quality reaches to 0.8.

While a number of investigations have been performed on the internal heat transfer and flow characteristics inside the curved coil, there is no generalized correlation for the shell-side tube bundles in the helical-coil steam generator. One of the most widely used correlations was proposed by Zukauskas and Ulinskas

(1985), and it is associated with the cross flow across banks of tubes in the form:

$$Nu = CRe_{max}^{m} Pr^{0.36} \left(\frac{Pr}{Pr_w} \right)^{0.25} \tag{2.57}$$

where the maximum Reynolds number is defined as the following:

$$Re_{max} = \frac{\rho u_{max} d_o}{\mu} \tag{2.58}$$

The values of C and m are governed by the tube arrangement, i.e. staggered or aligned, and the Reynolds number. Note that the characteristic dimension of the Reynolds number on the shell-side is the outer diameter of the tube, and the Reynolds number is based on the maximum fluid velocity that occurs when the fluid passes through the region of minimum inter-tube area. In the TAPINS, the minimum flow area is computed by taking into account the fractional area occupied by tubes in the transverse plane, as follows:

$$\frac{A_{min}}{A_{annu}} = 1 - N_{col} \frac{2 d_o}{D_o - D_i} \tag{2.59}$$

The sensitivity tests revealed, however, that the Zukauskas correlation quite underestimates the heat transfer rate to the helical coil when the fluid velocity is very low. The problem is overcome by introducing another correlation suggested by Churchill and Chu (1975a) for the external natural convection flows on the horizontal cylinder. The larger heat transfer coefficient between the two is chosen to calculate the heat transport in the primary side, combined with the total heat transfer area of the tube bundles.

In finding the time-dependent enthalpy-energy distributions in the tube-side of the helical-coil steam generator, a simplified approach is applied. The flow rate of the secondary coolant is assumed to be constant, and the following equation is solved for the energy balance:

$$\rho \frac{\partial h}{\partial t} + G \frac{\partial h}{\partial z} = \frac{q^{"} \xi_h}{A} \tag{2.60}$$

Eq. (2.60) is the simplified form of the energy conservation equation. Instead of solving the PDE for momentum conservation, the three components due to acceleration, friction loss and gravity are summed to give the total pressure drop along the helical coil. Moreover, the time-dependent heat conduction solutions are advanced across the tubes, which are divided into several intervals.

Another issue associated with a helical-coil S/G is the prediction of shell-side pressure loss across the tube bundles. Notwithstanding its crucial importance in sizing a heat exchanger and determining the convective flow rate in a primary system, a universal method applicable to various designs of helical-coil S/G is rarely found. In the TAPINS, the shell-side pressure loss is determined by referring to the research of Zukauskas and Ulinskas (1998) on the flows across banks of tubes. The pressure drop is expressed as:

$$\Delta P = Eu\left(\frac{\rho u_{max}^2}{2}\right) N_Z \tag{2.61}$$

where the Euler number is obtained from the correlation in the form:

$$Eu = c_0 + \frac{c_1}{Re} + \frac{c_2}{Re^2} + \frac{c_3}{Re^3} + \frac{c_4}{Re^4} \tag{2.62}$$

The coefficients of Eq. (2.62) depend on the Reynolds number, the configuration of tube bundles and the relative transverse pitch. The interpolated Euler number is reflected to calculate the friction loss term in the momentum equation.

Table 2.1 Interphase heat transfer coefficients for liquid

Regime	**Subcooled liquid**	**Superheated liquid**
Bubbly	$H_{if} = \dfrac{F_5 h_{fg}\rho_g\rho_f\alpha}{\rho_f-\rho_g} \quad \alpha > 0.0$ $= 0.0 \quad \alpha = 0.0$	$H_{if} = \max\left[\begin{array}{c} -\dfrac{k_f}{d_b}\dfrac{12}{\pi}\Delta T_{sf}\dfrac{\rho_f C_{pf}}{\rho_g h_{fg}}\beta \\ \dfrac{k_f}{d_b}\left(2.0+0.74\,\mathrm{Re}_b^{0.5}\right)\end{array}\right] a_{gf}$
Slug	$H_{if} = H_{if,Tb} + H_{if,bub}$ $H_{if,Tb} = 1.19\,\mathrm{Re}_f^{0.5}\,\mathrm{Pr}_f^{0.5}\dfrac{k_f}{D}a^*_{gf,Tb}\alpha_{Tb}$ $H_{if,bub}$: same as bubbly SCL	$H_{if} = H_{if,Tb} + H_{if,bub}$ $H_{if,Tb} = 3\times10^6 a^*_{gf,Tb}\alpha_{Tb}$ $H_{if,bub}$: same as bubbly SHL
Annular	$H_{if} = H_{if,ann} + H_{if,drp}$ $H_{if,ann} = 10^{-3}\rho_f C_{pf}\lvert v_f\rvert\alpha_{gf,ann}$ $H_{if,drp} = \dfrac{k_f}{d_d}F_{13}a_{gf,drp}$	$H_{if} = H_{if,ann} + H_{if,drp}$ $H_{if,ann} = 3\times10^6\alpha_{gf,ann}$ $H_{if,drp} = \dfrac{k_f}{d_d}F_{13}a_{gf,drp}$
Mist	$H_{if} = \dfrac{k_f}{d_d}a_{gf}$	$H_{if} = \dfrac{k_f}{d_d}F_{13}a_{gf}$

Table 2.2 Physical models of local phenomena in the steam-gas pressurizer

Type of mass transfer	**Physical model**
Flashing	$W_{fl} = \rho_g u_b \alpha_l A$
Rainout	$W_{ro} = \rho_f u_d (1-\alpha_v) A$
Interfacial mass transfer	$W_{itr} = \dfrac{f}{1-0.5f}\left[\dfrac{M}{2\pi R}\right]^{1/2}\left(\dfrac{P_v}{T_v^{1/2}}-\dfrac{P_s}{T_s^{1/2}}\right)\cdot A$
Wall condensation	$W_{wc} = Sh\dfrac{\rho D}{L}\dfrac{w_{nc,i}-w_{nc,b}}{w_{nc,i}}\cdot A$
Chocked flow	Modified Henry-Fauske model

Table 2.3 Empirical correlations for helical-coil S/G in the TAPINS

	Tube-side	**Shell-side**
Friction factor	Mori-Nakayama	Zukauskas
Heat transfer coefficient		
Subcooled water	Mori-Nakayama	Max (Zukauskas, Churchill-Chu)
Saturated boiling	Chen	
Dryout quality	Kozeki	
Mist evaporation	Linear interpolation	
Superheated steam	Mori-Nakayama	

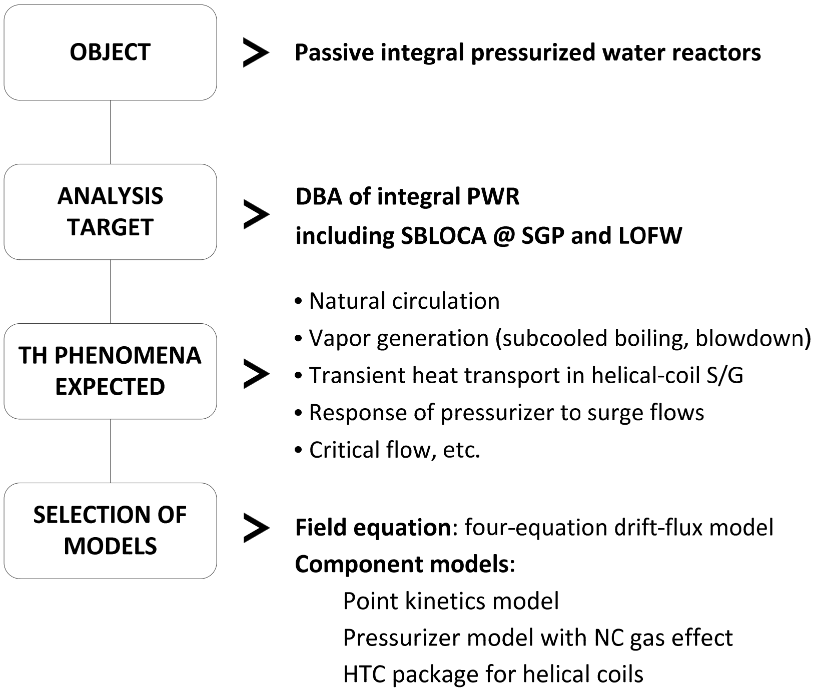

Figure 2.1 Design procedure of the TAPINS

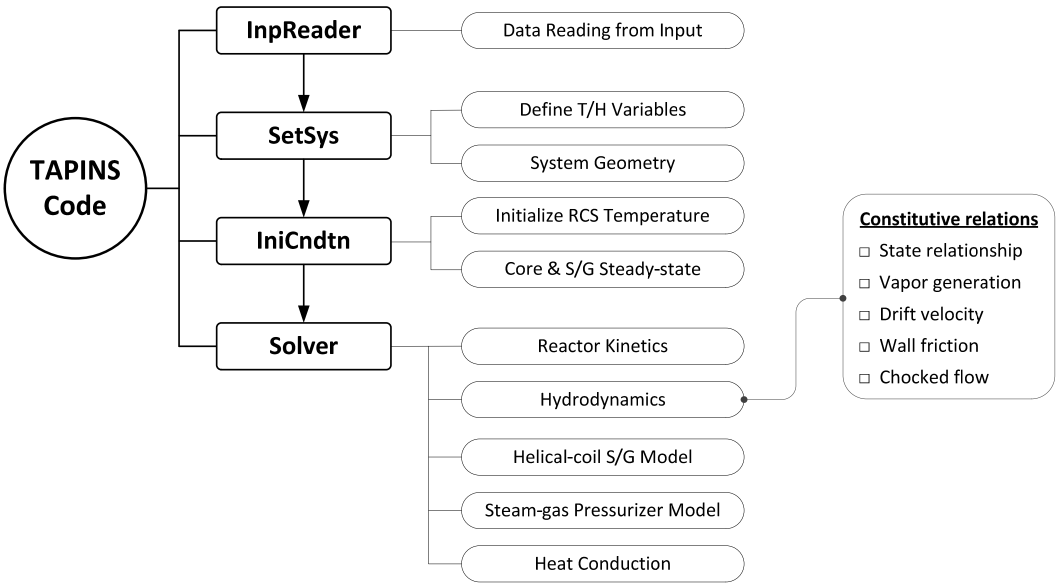

Figure 2.2 Code structure of the TAPINS

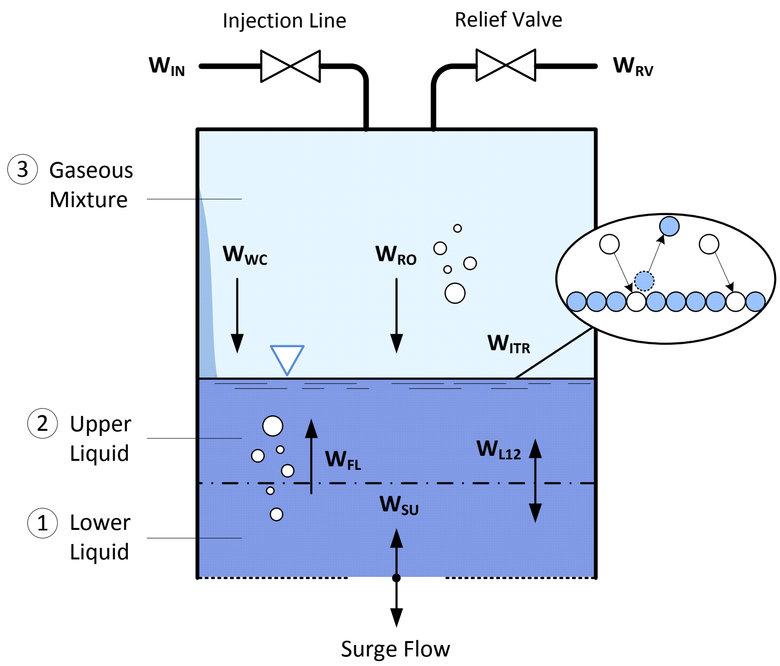

Figure 2.3 Local phenomena in the steam-gas pressurizer

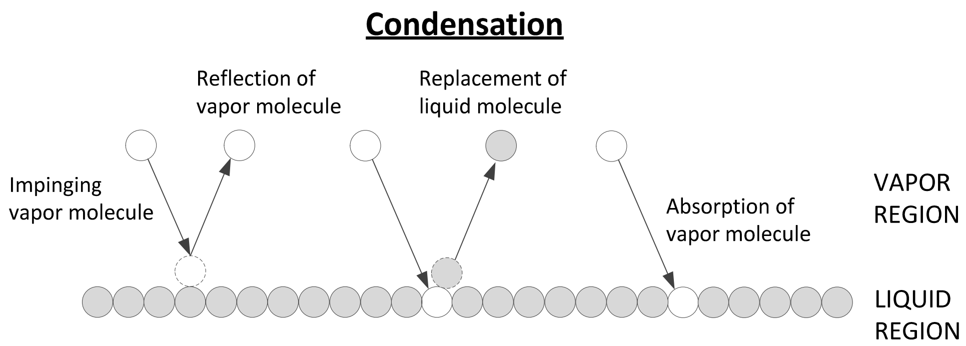

Figure 2.4 Mechanism of condensation at interface (Marek and Straub, 2001)

Chapter 3

Numerical Solution Method

3.1 Difference Scheme

In the TAPINS, the hydrodynamic model is numerically solved using a semi-implicit finite difference scheme on the staggered grid meshes. It has been proved that the semi-implicit scheme is numerically stable and capable of providing an accurate prediction for most applications. In the scheme, the terms associated with the sonic wave propagation are evaluated implicitly. All other terms, including the convection term in the momentum conservation equation, are evaluated at the old time level.

Since the large sources and sinks of momentum exist in a nuclear reactor, the momentum equation has not to be necessarily treated in the conservative form. Errors generated by using the non-conservative form are considered to be small, and the form is more convenient in numerical applications. Thus, the unsteady term and the convection term of the momentum conservation equation can be converted into the non-conservative form by using the continuity equation:

$$\frac{\partial}{\partial t}\left(\rho_m v_m\right)+\frac{\partial}{\partial z}\left(\rho_m v_m^2\right) \cong \rho_m \frac{\partial v_m}{\partial t}+\rho_m v_m \frac{\partial v_m}{\partial z} \tag{3.1}$$

The mesh cell configuration and the labeling convection for cell edges and cell centers are illustrated in Fig. 3.1. On the staggered spatial meshes, the scalar properties (pressure, enthalpy, and void fraction) of the flow are defined at cell centers, and the vector quantities (velocity) are defined on the cell boundaries. Thus, the difference equations for each cell are obtained by integrating the mass and energy equations over the mesh cells from inlet junction to outlet junction. The momentum equation is differenced at the cell edges.

For example, when the mass equation is integrated in a cell, the differential equations expressed in terms of cell-averaged properties and cell boundary fluxes are obtained as following:

$$V_i \left. \frac{\partial \rho_m}{\partial t} \right|_i + \left[\rho_m v_m A \right]_{x_{i-1/2}}^{x_{i+1/2}} = 0 \tag{3.2}$$

The resulting difference equation using the staggered spatial difference scheme is:

$$V_i \frac{(\rho_m)_i^{n+1} - (\rho_m)_i^n}{\Delta t} + (\rho_m)_{i+1/2}^n (v_m)_{i+1/2}^{n+1} A_{i+1/2} - (\rho_m)_{i-1/2}^n (v_m)_{i-1/2}^{n+1} A_{i-1/2} = 0 \tag{3.3}$$

Be sure that the junction area, upon which velocities are based, is the minimum area of the two adjoining volumes as:

$$A_{i+1/2} = \min(A_i,\ A_{i+1}) \tag{3.4}$$

The same procedure is applied to the other balance equations, except that the momentum equation is integrated from cell center “i” to “$i+1$”. The resulting difference equation for vapor mass, mixture momentum and mixture energy are as following:

$$V_i \frac{(\alpha\rho_v)_i^{n+1}-(\alpha\rho_v)_i^n}{\Delta t}+(\alpha\rho_v)_{i+1/2}^n(v_m)_{i+1/2}^{n+1}A_{i+1/2}-(\alpha\rho_v)_{i-1/2}^n(v_m)_{i-1/2}^{n+1}A_{i-1/2}$$

$$+\left[\frac{\alpha\rho_v\rho_l\overline{V_{gj}}A}{\rho_m}\right]_{i+1/2}^n-\left[\frac{\alpha\rho_v\rho_l\overline{V_{gj}}A}{\rho_m}\right]_{i-1/2}^n=V_i\cdot\Gamma_g \tag{3.5}$$

$$(\rho_m)_{i+1/2}^n\Delta z_{i+1/2}\frac{(v_m)_{i+1/2}^{n+1}-(v_m)_{i+1/2}^n}{\Delta t}+(\rho_m)_{i+1/2}^n(v_m)_{i+1/2}^n\left[(v_m)_{i+1}^n-(v_m)_i^n\right]$$

$$+\left\{\left[\frac{\alpha\rho_v\rho_l}{(1-\alpha)\rho_m}\overline{V_{gj}}^2\right]_{i+1}^n-\left[\frac{\alpha\rho_v\rho_l}{(1-\alpha)\rho_m}\overline{V_{gj}}^2\right]_i^n\right\}+\left(P_{i+1}^{n+1}-P_i^{n+1}\right)$$

$$+(\rho_m)_{i+1/2}^n g_z\Delta H_{z,i+1/2}+f_m\frac{L}{2D}(\rho_m)_{i+1/2}^n(v_m)_{i+1/2}^n\left|(v_m)_{i+1/2}^n\right|=0 \tag{3.6}$$

$$V_i\frac{(\rho_m h_m)_i^{n+1}-(\rho_m h_m)_i^n}{\Delta t}+(\rho_m h_m)_{i+1/2}^n(v_m)_{i+1/2}^{n+1}A_{i+1/2}-(\rho_m h_m)_{i-1/2}^n(v_m)_{i-1/2}^{n+1}A_{i-1/2}$$

$$+\left\{\left[\frac{\alpha\rho_v\rho_l}{\rho_m}\Delta h_{gf}\overline{V_{gj}}A\right]_{i+1/2}^n-\left[\frac{\alpha\rho_v\rho_l}{\rho_m}\Delta h_{gf}\overline{V_{gj}}A\right]_{i-1/2}^n\right\}-V_i\frac{P_i^{n+1}-P_i^n}{\Delta t} \tag{3.7}$$

$$-V_i\left[v_m+\frac{\alpha(\rho_l-\rho_v)}{\rho_m}\overline{V_{gj}}\right]_i^n\frac{P_{i+1/2}^{n+1}-P_{i-1/2}^{n+1}}{\Delta z_i}\Bigg\}=V_i\left(\frac{q_W''\xi_h}{A}\right)$$

Note that the convective terms in the mass and energy equations, the pressure gradient term in the momentum equation, and the compressible work term in the energy equation all contain terms evaluated at the new time level. All other terms, including the wall friction term and the wall heat source term, are evaluated at the old time level. Because the phase transition term Γ_g represents important source or loss mechanisms for vapor, it is treated in an implicit manner as shown in the next section. It is known that, when the semi-implicit scheme is employed, an approximate criterion of numerical stability is defined in the form:

$$v_m\frac{\Delta t}{\Delta z}<1 \tag{3.8}$$

The above difference equations have to be supplemented by additional relationships among variables at the edges and the cell centers. In the TAPINS, the donor cell difference scheme that is particularly stable is employed. It is expressed as:

$$\zeta_{i+1/2} = \left(\frac{1+\beta_{i+1/2}}{2} \right) \zeta_i + \left(\frac{1-\beta_{i+1/2}}{2} \right) \zeta_{i+1} \tag{3.9}$$

$$v_i = \left(\frac{1+\beta_{i+1/2}}{2} \right) v_{i-1/2} + \left(\frac{1-\beta_{i+1/2}}{2} \right) v_{i+1/2} \tag{3.10}$$

where ζ denotes scalar quantities such as density and enthalpy. β is chosen for full donor cell differencing as:

$$\beta_{i+1/2} = \frac{v_{i+1/2}}{\left| v_{i+1/2} \right|} \tag{3.11}$$

In short, the quantities are defined by the principle of the upwind scheme which takes into account the flow directions.

3.2 Solution Procedure

The difference equations (3.3) and (3.5)-(3.7) in conjunction with constitutive relations of Chapter 2.4 represent a nonlinear algebraic system of equations for all mesh variables at the new time level. In the TAPINS, void fraction (α), pressure (P), mixture velocity (v_m) and liquid enthalpy (h_l) are selected as four primitive variables. To solve this system of equations, the TAPINS employs the Newton Block Gauss Seidel (NBGS) method (Liles and Reed, 1978).

In the NBGS technique, all unknowns appearing in the difference equations, except four primitive variables, are eliminated by the linearization in terms of the latest iterate values and the four fundamental unknowns. For the mixture mass conservation equation, the mixture density $(\rho_m)_i^{n+1}$ has to be linearized. From the definition given by Eq. (3.1), it is linearized as:

$$\begin{aligned} \rho_m &= \tilde{\rho}_m + \Delta\alpha \frac{\partial \tilde{\rho}_m}{\partial \alpha} + \Delta\rho_l \frac{\partial \tilde{\rho}_m}{\partial \rho_l} + \Delta\rho_v \frac{\partial \tilde{\rho}_m}{\partial \rho_v} \\ &= \tilde{\rho}_m + (\tilde{\rho}_v - \tilde{\rho}_l)(\alpha - \tilde{\alpha}) + (1-\tilde{\alpha})(\rho_l - \tilde{\rho}_l) + \tilde{\alpha}(\rho_v - \tilde{\rho}_v) \end{aligned} \tag{3.12}$$

By thermal equation of state for the liquid and the vapor,

$$\rho_l = \tilde{\rho}_l + \frac{\partial \tilde{\rho}_l}{\partial P}(P - \tilde{P}) + \frac{\partial \tilde{\rho}_l}{\partial h_l}(h_l - \tilde{h}_l) \tag{3.13}$$

$$\rho_v = \tilde{\rho}_v + \frac{\partial \tilde{\rho}_v^s}{\partial P}(P - \tilde{P}) \tag{3.14}$$

Substituting Eqs. (3.13) and (3.14) to Eq. (3.12) yields:

$$\begin{aligned} \rho_m = \tilde{\rho}_m + (\tilde{\rho}_v - \tilde{\rho}_l)(\alpha - \tilde{\alpha}) + \left[(1-\tilde{\alpha}) \frac{\partial \tilde{\rho}_l}{\partial P} + \tilde{\alpha} \frac{\partial \tilde{\rho}_v^s}{\partial P} \right](P - \tilde{P}) \\ + (1-\tilde{\alpha}) \frac{\partial \tilde{\rho}_l}{\partial h_l}(h_l - \tilde{h}_l) \end{aligned} \tag{3.15}$$

Eq. (3.15) expresses a linear relationship between the mixture density and three primitive variables. Then the resulting continuity equation is expressed as:

$$\begin{aligned} &(\rho_m)_i^k - (\rho_m)_i^n + \left[(\rho_v)_i^k - (\rho_l)_i^k \right](\alpha_i^{k+1} - \alpha_i^k) \\ &+ \left[(1-\alpha_i^k) \frac{\partial \rho_l^k}{\partial P} + \alpha_i^k \frac{\partial (\rho_v^s)^k}{\partial P} \right] \cdot (P_i^{k+1} - P_i^k) + (1-\alpha_i^k) \frac{\partial \rho_l^k}{\partial h_l} \cdot [(h_l)_i^{k+1} - (h_l)_i^k] \\ &+ \frac{\Delta t}{V_i} \left[(\rho_m)_{i+1/2}^n (v_m)_{i+1/2}^{k+1} A_{i+1/2} - (\rho_m)_{i-1/2}^n (v_m)_{i-1/2}^{k+1} A_{i-1/2} \right] = 0 \end{aligned} \tag{3.16}$$

It is noted that the superscripts are introduced to indicate successive iterative approximation to variables at the new time level, and tilde quantities are evaluated at the k th iterate.

The same procedure is applied to the vapor mass conservation equation and the mixture energy equation. In the vapor mass conservation equation, $(\alpha\rho_v)_i^{n+1}$ is linearized as following:

$$\alpha\rho_v = \left(\tilde{\alpha}\tilde{\rho}_v\right) + \tilde{\rho}_v\left(\alpha - \tilde{\alpha}\right) + \tilde{\alpha}\frac{\partial\tilde{\rho}_v^s}{\partial P}(P - \tilde{P}) \tag{3.17}$$

In the TAPINS, the phase change term is implicitly coupled by the linearized definition since it represents vapor production which strongly affects the fluid dynamics. Because the vapor phase is assumed to be at the saturation temperature, from the definition given by Eq. (2.24), the R.H.S of Eq. (3.5) can be expressed as:

$$\begin{aligned} & R.H.S. \\ & = -\frac{H_{if}^n \cdot \Delta t}{(h_v^*)_i^n - (h_l^*)_i^n}\left[(T^s)_i^{n+1} - (T_l)_i^{n+1}\right] + \Delta t \cdot \Gamma_w^n \\ & = -\frac{H_{if}^n \cdot \Delta t}{(h_v^*)_i^n - (h_l^*)_i^n}\left\{(T^s)_i^k + \frac{\partial (T^s)^k}{\partial P}(P_i^{k+1} - P_i^k) - (T_l)_i^k - \frac{\partial T_l^k}{\partial P}(P_i^{k+1} - P_i^k)\right. \\ & \quad \left. - \frac{\partial T_l^k}{\partial h_l}[(h_l)_i^{k+1} - (h_l)_i^k]\right\} + \Delta t \cdot \Gamma_w^n \end{aligned} \tag{3.18}$$

Then the final form of the vapor mass conservation equation is:

$$\begin{aligned} & (\rho_v)_i^k\left(\alpha_i^{k+1} - \alpha_i^k\right) + \left[\alpha_i^k\frac{\partial(\rho_v^s)^k}{\partial P} + \frac{H_{if}^n \cdot \Delta t}{(h_v^*)_i^n - (h_l^*)_i^n}\cdot\left(\frac{\partial (T^s)^k}{\partial P} - \frac{\partial T_l^k}{\partial P}\right)\right]\cdot(P_i^{k+1} - P_i^k) \\ & \quad - \frac{H_{if}^n \cdot \Delta t}{(h_v^*)_i^n - (h_l^*)_i^n}\cdot\frac{\partial T_l^k}{\partial h_l}[(h_l)_i^{k+1} - (h_l)_i^k] \\ & \quad + \frac{\Delta t}{V_i}\left[(\alpha\rho_v)_{i+1/2}^n(v_m)_{i+1/2}^{k+1}A_{i+1/2} - (\alpha\rho_v)_{i-1/2}^n(v_m)_{i-1/2}^{k+1}A_{i-1/2}\right] \end{aligned}$$

$$
\begin{aligned}
&= \alpha_i^n(\rho_v)_i^n - \alpha_i^k(\rho_v)_i^k - \frac{\Delta t}{V_i}\left\{\left[\frac{\alpha\rho_v\rho_l\overline{V_{gj}}A}{\rho_m}\right]_{i+1/2}^n - \left[\frac{\alpha\rho_v\rho_l\overline{V_{gj}}A}{\rho_m}\right]_{i-1/2}^n\right\} \\
&- \frac{H_{if}^n\cdot\Delta t}{(h_v^*)_i^n-(h_l^*)_i^n}\left[(T^s)_i^k-(T_l)_i^k\right] + \Delta t\cdot\Gamma_w^n
\end{aligned}
\tag{3.19}
$$

For the mixture energy equation, the $(\rho_m h_m)_i^{n+1}$ term is linearized by using the specified definition of Eq. (2.3) and the final form of linear algebraic equation is derived in the same way as described above:

$$
\begin{aligned}
&(\rho_m h_m)_i^k - (\rho_m h_m)_i^n + \left[(\rho_v h_v)_i^k - (\rho_l h_l)_i^k\right](\alpha_i^{k+1}-\alpha_i^k) \\
&+\left\{(1-\alpha_i^k)\cdot(h_l)_i^k\frac{\partial\rho_l^k}{\partial h_l} + \alpha_i^k(h_v)_i^k\frac{\partial(\rho_v^s)^k}{\partial P} + \alpha_i^k(\rho_v)_i^k\frac{\partial(h_v^s)^k}{\partial P}\right\}\cdot(P_i^{k+1}-P_i^k) \\
&+(1-\alpha_i^k)\left[(\rho_l)_i^k + (h_l)_i^k\frac{\partial\rho_l^k}{\partial h_l}\right]\cdot[(h_l)_i^{k+1}-(h_l)_i^k] \\
&+\frac{\Delta t}{V_i}\left[(\rho_m h_m)_{i+1/2}^n(v_m)_{i+1/2}^{k+1}A_{i+1/2} - (\rho_m h_m)_{i-1/2}^n(v_m)_{i-1/2}^{k+1}A_{i-1/2}\right] \\
&+\frac{\Delta t}{V_i}\left\{\left[\frac{\alpha\rho_v\rho_l}{\rho_m}\Delta h_{gf}\overline{V_{gj}}A\right]_{i+1/2}^n - \left[\frac{\alpha\rho_v\rho_l}{\rho_m}\Delta h_{gf}\overline{V_{gj}}A\right]_{i-1/2}^n\right\} - (P_i^{k+1}-P_i^n) \\
&-\frac{\Delta t}{\Delta z_i}\left[v_m + \frac{\alpha(\rho_l-\rho_v)}{\rho_m}\overline{V_{gj}}\right]_i^n\left(P_{i+1/2}^{k+1}-P_{i-1/2}^{k+1}\right) = \Delta t\cdot\left(\frac{q_W^{"}\xi_h}{A}\right)
\end{aligned}
\tag{3.20}
$$

Then Eqs. (3.6), (3.16), (3.19), (3.20) forms a complete set of linear algebraic equations for the four primitive variables. These linear algebraic equations are applied to all the modeled nodes and junctions in the system.

When a linear system based on the above formulations is set up for all the meshes in the loop, the entries of the matrix are arranged in a regular pattern as shown below; the nonzero entries are grouped into a pattern of 5 × 5 blocks in the linear system.

$$
\begin{bmatrix}
X & 0 & X & & & & & & \\
 & \ddots & & & & & & & \\
X & 0 & A_{i11} & 0 & A_{i13} & 0 & 0 & & \\
 & & A_{i21} & A_{i22} & A_{i23} & A_{i24} & A_{i25} & & \\
 & & A_{i31} & A_{i32} & A_{i33} & A_{i34} & A_{i35} & & \\
 & & A_{i41} & A_{i42} & A_{i43} & A_{i44} & A_{i45} & & \\
 & & 0 & 0 & A_{i53} & 0 & A_{i55} & 0 & X \\
 & & & & & & & \ddots & \\
 & & & & & X & X & X & X
\end{bmatrix}
\begin{bmatrix} v_1 \\ \vdots \\ v_{i-1/2} \\ \delta\alpha_i \\ \delta P_i \\ \delta h_i \\ v_{i+1/2} \\ \vdots \\ \delta h_N \end{bmatrix}
=
\begin{bmatrix} \vdots \\ b_{i1} \\ b_{i2} \\ b_{i3} \\ b_{i4} \\ b_{i5} \\ \vdots \\ \\ \end{bmatrix}
$$

In above matrix, the unknowns for scalar quantities are defined as a variation in a single iteration as following:

$$\delta\psi_i = \psi_i^{k+1} - \psi_i^k \tag{3.21}$$

Each of these blocks represents the coefficients of primitive variables for a single mesh cell. The first and fifth rows of the block identify the momentum equations for the inlet and outlet junction of a cell; the remaining rows are set up from the mixture mass, vapor mass, and mixture energy equations.

Note that the five fundamental unknowns for a given cell are coupled only to the pressures in adjoining cells. Thus, if the pressures in the left (upstream) cell and the right (downstream) cell are held fixed, one can solve the 5 × 5 linear system to obtain the updated primitive variables. This indicates the fundamentals of the NBGS technique.

The NBGS method is performed initially by choosing a direction of sweeping the mesh. The method takes the concept of Gauss-Seidel method. The unknowns of a given cell are obtained using the new (just updated) pressure in the left cell but an old iterate pressure in the right cell. One can achieve the fast convergence by using the advanced information as soon as they are known in this way. It is noted that the velocity on the boundary between cells is updated twice in this method. This process is continued until the primitive variables in all the cells are updated. The iteration is terminated when the relative pseudo error of pressure is less than a specified value in all meshes. The convergence criterion to be satisfied is expressed as:

$$\frac{\left|P_i^{k+1} - P_i^k\right|}{P_i^{k+1}} < 10^{-6} \tag{3.22}$$

The calculation procedure of the TAPINS follows six major steps, as shown in Fig. 3.2.

Step 1: From the geometry input and the initial conditions supplied by a user, the pre-processors required to the computation are prepared. The fundamental variables are defined and the fluid conditions and properties are initialized.

Step 2: Before getting into the iteration loop, the constitutive parameters for wall-to-fluid heat transfer, wall friction, vapor generation, drift velocity etc. are explicitly calculated using the old time variables.

Step 3: The iteration loop starts here. The old iterate fundamental variables are assigned to solve governing equations for a mesh cell. Thermodynamic properties are called and the partial derivatives of properties are computed.

Step 4: The 5 × 5 linear system is solved by Gauss elimination. From the new values for the primitive variables, other remaining unknowns are updated. Steps 3 and 4 are performed for all mesh cells.

Step 5: The convergence test is performed. If the convergence does not succeed, Steps 3 and 4 are repeated unless the iteration number exceeds a specified maximum value.

Step 6: The converged variables are stored and several major output parameters are calculated. Advance to the next time step.

The core and the helical-coil steam generator models explicitly evaluate the wall heat sources appearing in the energy conservation equation, and the steam-gas pressurizer model provides the pressure boundary for the field equation solver.

The numerical solution method to facilitate solutions for the steam-gas pressurizer model is also suggested in this study. Since the thermal constraint of Eq. (2.52) is not a formulated explicit function, but a relation achievable from the steam table, a linear matrix system cannot be established; therefore, the iteration method is employed in getting the solutions. The detailed procedure is described in Fig. 3.3. To make a long story short, the guessed pressure rate of each gaseous component is calculated by using the pressure equation, Eq. (2.55), and the Gibbs-Dalton law, Eq. (2.51), and the convergence is checked by updating these estimations from the energy equations.

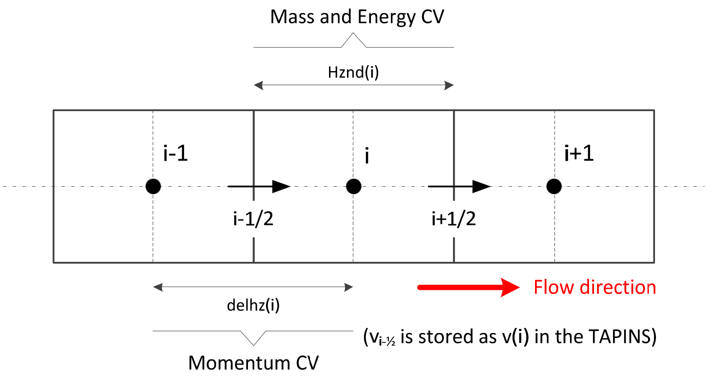

Figure 3.1 Mesh cell configurations

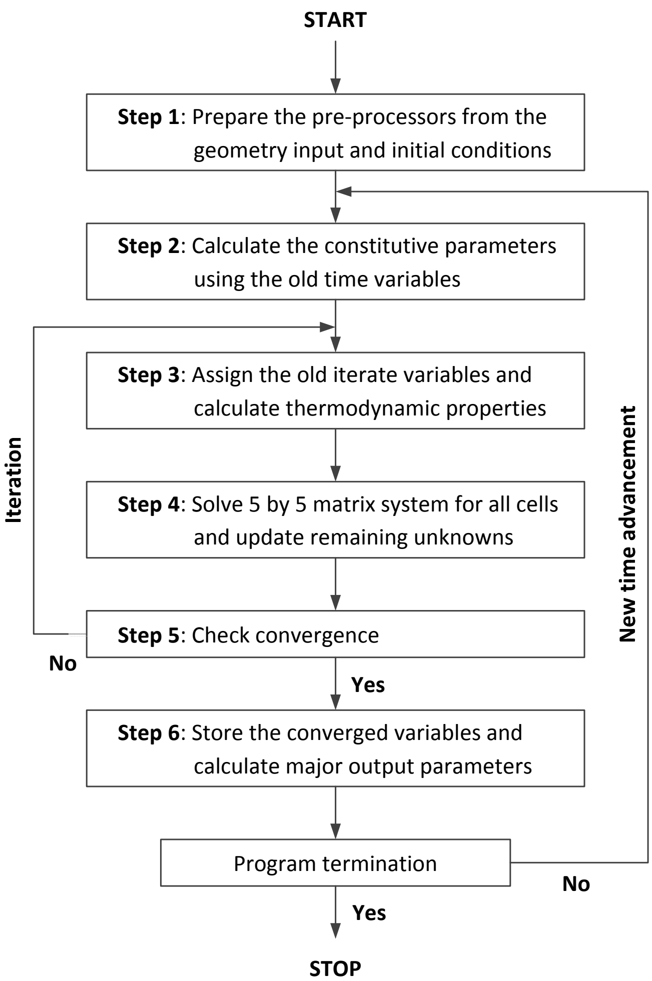

Figure 3.2 Calculation procedure of the TAPINS

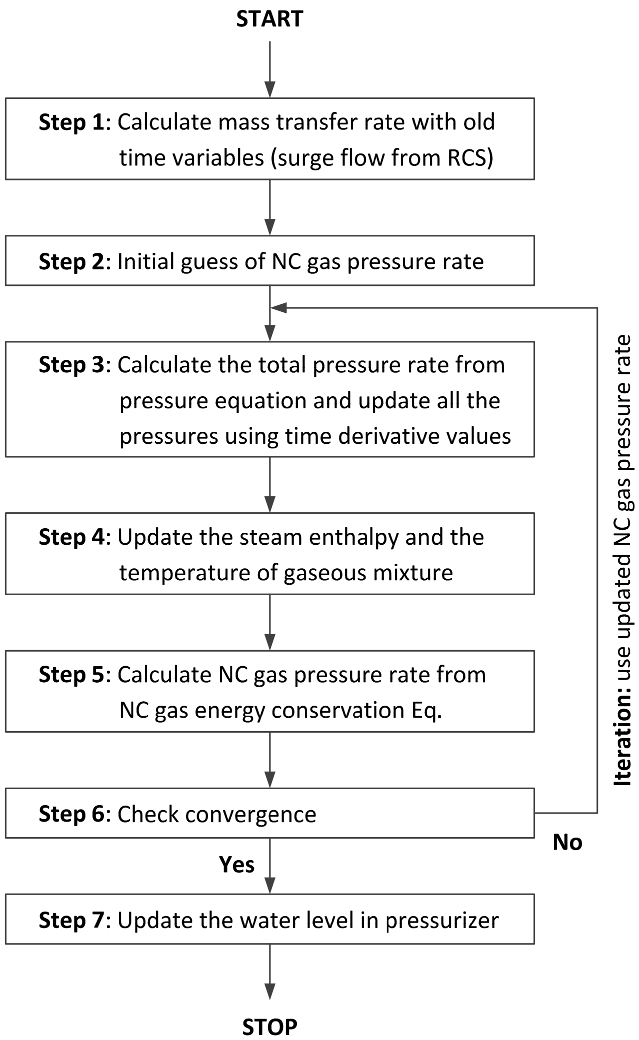

Figure 3.3 Calculation procedure of the steam-gas pressurizer model

Chapter 4

TAPINS Verification and Validation

To assess the applicability of the TAPINS for thermal-hydraulic simulations of integral PWRs, a wide variety of flow situations have been run with the TAPINS. The problems for developmental assessment of TAPINS are categorized into three types: verification problems, separate effects experiments, and integral effects experiments. Two simple verification problems are used to demonstrate that the physical equations have been correctly translated into the TAPINS. For code validation, a total of 5 calculation sets have been simulated, ranging from the steady-state boiling experiments to IET performed in a scaled model of REX-10.

The V&V matrix is presented in Table 4.1 with a brief description on the assessment objectives of each problem. The qualitative and quantitative accuracy of the TAPINS is determined for the problems consistent with the intended application; this assessment matrix is to validate the mathematical models for thermal-hydraulic phenomena encountered in DBAs of an integral PWR.

4.1 Verification Problems

The code verification is the process of determining that the code correctly implements a desired physical model and numerical algorithm. When performing the verification, one can use analytical solutions of mathematical equations to calculate error in a corresponding approximate solution or employ some kinds of phenomenological problems to confirm that the code is in qualitative agreement with the physics of the problem. In this paper, the mass and energy conservation problem and the natural circulation problem is calculated with the TAPINS.

4.1.1 Mass and Energy Conservation Problem

The mass and energy conservation problem is to estimate the truncation error generated from processes in which the non-linear partial differential equations are discretized into the first-order ordinary differential equations or linear algebraic equations, and the unknowns in the field equations are linearized in terms of the primitive variables. In this problem, the circular channel of 0.6 m in length and 0.1 m in diameter is connected to the pressure boundary at the exit and the inlet flow boundary condition is implemented as in Fig. 4.1. Then the calculation results of TAPINS are used to confirm whether the total mass and energy of the system is preserved.

Two flow conditions are analyzed in this problem: one is the single-phase flow that the subcooled liquid of 200 ^{o}C, which is the core outlet temperature of REX-10, enters into the tube without an external heat source, and the other is the two-phase flow that the saturated liquid is heated up in node 2, causing the flow boiling in nodes 2 and 3. For these cases, the mass and energy errors arising from the numerical solution scheme of the TAPINS are evaluated.

The mass and energy errors are computed by comparing those derived from the mass conservation equation and equations of state. When calculating the mass error, the mass expected in the new time step by the inflow and outflow of fluid can be calculated by:

$$M_e^{n+1} = M^n + (W_{in}^n - W_{out}^n) \cdot \Delta t \tag{4.1}$$

Then, the fractional mass error from the value obtained by the equation of state is defined as:

$$\varepsilon_M = \frac{M_e^{n+1} - M^{n+1}}{M^{n+1}} \tag{4.2}$$

The energy error is calculated in the same way. In this problem, the conservation of the mixture enthalpy is checked as:

$$H_e^{n+1} = H^n + (W_{in}^n \cdot H_{in}^n - W_{out}^n \cdot H_{out}^n) \cdot \Delta t \tag{4.3}$$

$$\varepsilon_H = \frac{H_e^{n+1} - H^{n+1}}{H^{n+1}} \tag{4.4}$$

Figures 4.2 and 4.3 show the fractional mass and energy errors when the single-phase liquid at 20 bar and 200 ^{o}C flows through the channel. The fractional error of the TAPINS reaches the maximum of 2×10^{-6} at the initial stage, then approaches near zero as the equilibrium state is quickly established (10^{-16}~10^{-15} for mass, about 10^{-10} for energy). Thus, one can confirm that the mass and energy errors resulting from the numerical solution method of the TAPINS is negligibly small.

The calculation results for mass and energy conservation of the two-phase flow in the presence of an external heat source are depicted in Figs. 4.4 and 4.5. In this two-phase flow condition, the fractional error of the TAPINS is estimated higher than that of subcooled liquid flow; the maximum fractional error observed at the initial transient is about 2×10^{-2}. The reason why the mass and energy errors are much higher for two-phase flow is that, in a linearization procedure to derive the difference equations, the approximation of mixture variable comprise both liquid and vapor properties. As in the single-phase liquid analysis, the flow condition reaches steady-state after a few time steps of calculation. Then the fractional error is maintained at 10^{-16}~10^{-15} for mass, and about 10^{-4} for energy. From the calculation results, one can conclude that the truncation error caused by the numerical scheme of the TAPINS is negligible, and the mass and energy are well preserved.

4.1.2 Natural Circulation Problem

The natural circulation is the most important phenomenon in design, operation and safety analysis of a fully-passive integral PWR. Accordingly, the predictive capability of the TAPINS has to be essentially verified. The natural circulation problem presented in this section is a basic benchmark to calculate the flow rate of free convection driven by the density gradients in a closed loop, and compare the results with the analytical solutions. As depicted in Fig. 4.6, the natural circulation is created by heating water from below and cooling it from above. The vertically oriented channel is 0.1 m in diameter and 0.4 m in height.

In the TAPINS modeling, the whole channel is comprised of 8 identical nodes, and the same amount of heat applied to node 1 is removed from node 5. The initial inlet conditions of node 1 are fixed to 20 bar and 100 ^{o}C in all the cases. The predicted natural circulation flow rate according to the heating power is compared with the analytical solution.

An analytical expression for the steady-state natural circulation flow is derived from the momentum equation as (Lewis, 1977):

$$W_{NC} = \left[\frac{2\bar{\rho}^2 g \beta P}{C_p R} \left(\bar{z}_{SG} - \bar{z}_{core} \right) \right]^{1/3} \tag{4.5}$$

where R denotes the total flow resistance around loop defined as:

$$R = \sum_k f_k \frac{L_k}{D_{h_k} A_k^2} + \sum_j \frac{K_j}{A_j^2} \tag{4.6}$$

For convenience of handy calculation on the analytic solution, the wall friction factor is set to 0 and the form loss coefficient is given as 0.1 to all junctions. As shown in Eq. (4.5), the natural circulation flow rate is determined not only from the fluid properties but also the power level, the effective difference in elevation between the heat source and the heat sink, and the total flow resistance of a circuit. In this calculation, the predictions of the TAPINS at 2.5, 5.0, 7.5, and 10.0 kW are compared to the analytical solutions. The results are tabulated in Table 4.2.

Inspection of Table 4.2 reveals that the deviations of the predictions from the analytical solutions are less than 0.55 %. The error gets larger with an increase in the power level since the mean water properties are deviated from those calculated at 100 ^{o}C as the rise in the coolant temperature increases. By using the properties and parameters summarized in Table 4.2, the relations between the heat input and natural circulation flow rate is acquired from Eq. (4.5), which is plotted in Fig. 4.7. Eq. (4.5) tells us that the mass flow rate is proportional to the total heat input to the power of 1/3. Figure 4.7 shows that the predictions of the TAPINS accurately conform to the relation. From the above simulations, the predictive capability of the TAPINS on the natural circulation phenomena is assessed.

4.2 Separate Effects Problems

4.2.1 MIT Pressurizer Test

The first validation activity that is carried out for a comprehensive assessment of the TAPINS is concerned with the steam-gas pressurizer model. As it is not essential for the conventional pressurizer used in NPPs, the experimental data on the transient response of the pressurizer in the presence of non-condensable gas is quite rare. However, Leonard (1983) performed a series of separate effect tests to investigate the responses of a small-scale pressurized vessel to insurge transients with three non-condensable gases: nitrogen, helium and argon. The pressure histories caused by the rapid insurge were observed with different types and concentrations of non-condensable gas.

The schematic diagram of the test facility is depicted in Fig. 4.8. The primary tank in the tests is 0.203 m in inner diameter and 1.143 m in height. The transient is initiated by injecting the subcooled water into the primary tank from the storage tank pressurized with nitrogen. The insurge is maintained for approximately 35 s. The accuracy of the pressure behavior predicted by the newly proposed dynamic model in the TAPINS is evaluated against the data from the separate effect tests conducted by Leonard. Among the various test cases, two cases of the insurge transient in the presence of nitrogen are simulated with the TAPINS, since nitrogen would constitute the gaseous mixture in the steam-gas pressurizer of

REX-10.

Figure 4.9 displays the transient calculation result when the initial mass fraction of nitrogen is 9.7 %. During the insurge, the vessel pressure continuously rises by virtue of the reduction in the gas volume. After termination of the insurge, however, the wall heat transfer from the gaseous mixture results in a moderate decrease in the pressure. The rate of decline slowly decreases as the naturally convective gaseous mixture becomes stagnant after the rise in the water level ceases. Figure 4.9 reveals that the steam-gas pressurizer model in the TAPINS successfully predicts the pressure histories arising from these mechanisms. The deviation of the calculated final water level from the measured one is at most 1.5 mm.

A notable simulation result is observed when the two-region pressurizer model is employed, in which the thorough mixing of the insurge flow with the liquid phase is assumed by using a single integrated control volume for the liquid regions. While the insurge of subcooled water immediately leads to a decrease in the temperature of an overall liquid region in the simulation of a two-region model, the hot liquid layer, keeping the temperature nearly constant, floats to the top of the liquid region due to thermal stratification in the actual conditions. The net effect is that the interfacial mass transfer at the interface into the liquid is over-predicted, so that the pressure response to the insurge is miscalculated. Figure 4.9 clearly exhibits the improved accuracy of the three-region model over the two-region model. In this kind of SET apparatus, which has quite a small volume, slight differences in the calculated mass transfer rates of local phenomena may give rise to considerable deviation in the simulation results.

The simulation result when the mass fraction of nitrogen goes up to 20.1 % is plotted in Fig. 4.10. Compared to Fig. 4.9, the pressure transient exhibits a steeper slope during the insurge and a higher peak value. It is widely reported that the accumulated non-condensable gas along the wall provides resistance against heat transfer to the wall by condensation. Therefore, the rate of wall condensation is degraded as the concentration of non-condensable gas increases. By incorporating the condensation model with the heat and mass transfer analogy, the TAPINS predicts the pressure response caused by insurge transients with reasonable accuracy.

4.2.2 Subcooled Boiling Tests

The subcooled boiling is a representative phenomenon associated with the non-equilibrium effect of two-phase flow. Where there is a local boiling from the heated surface, vapor bubbles may nucleate at the wall even though the mean enthalpy of the liquid phase is less than saturation. In this phenomenon, the liquid is still subcooled, whereas the vapor bubbles are generated regularly at the wall surface and condensed as they slowly move through the fluid. That is, the subcooled boiling is characterized by the fact that thermodynamic equilibrium does not exist (Lahey, 1993).

The interphase mass transfer and the wall heat flux partitioning model of the TAPINS is assessed using the data from subcooled boiling tests conducted by Christensen (1961) and Bartolomey (1967). The test section of the Christensen experiment consists of a 127 cm long stainless steel tube of the rectangular cross-section (dimensions 1.11 cm × 4.44 cm). The tube is heated by passing an AC current through the tube walls. The void fraction along the test tube is measured by a gamma densitometer. Four different runs are simulated with the TAPINS, and the test conditions for these runs are given in Table 4.3. In particular, the run No. 15 test is a widely known SET problem used to validate the RELAP5 (Ransom et al., 2001b)

The experiment of Bartolomey is performed in a uniformly heated vertical tube of 12 mm in inlet diameter and 1 m in height. Experimental data are obtained at the pressure ranging from 3.0 to 14.7 MPa with various heat fluxes, mass fluxes, and inlet liquid temperature. Four selected tests are calculated by the TAPINS for evaluation of the subcooled boiling model. The test conditions for these sets are summarized in Table 4.4.

For both experiments, the TAPINS models the test sections with 20 vertically oriented nodes. Figures 4.11 – 4.14 show the calculation results of the TAPINS for the Christensen experiments. In the TAPINS, the mass transfer rate per unit volume near a wall is calculated by the Lahey method (Lahey, 1978), and the void departure point is predicted by the correlation proposed by Saha and Zuber (1974). The computed void profiles from the TAPINS are in good agreement with the experimental data of Christensen as shown in Figs. 4.11 – 4.14.

The calculation results of the TASS/SMR are also plotted in Fig. 4.13. Since the TASS/SMR employs the homogeneous equilibrium model as governing equations, it cannot predict the vapor generation before the onset of bulk boiling even though there already are significant subcooled voids. In addition, even after the bulk enthalpy is saturated, the prediction of the TASS/SMR exhibits some deviations from data. It is because the HEM does not take the relative velocity between phases into account. Then the predicted void fraction versus the flow quality shows some discrepancy with data even when the mixing cup is the same.

Therefore, the TAPINS can provide more accurate prediction on the two-phase flow phenomena with non-equilibrium effect than the TASS/SMR.

The void fraction profiles of the Bartolomey experiment are plotted in Figs. 4.15 – 4.18. While the slug flow regime appears at the exit in the Christensen experiment, the transition to annular-mist flow is encountered in the Bartolomey experiment. The prediction of the TAPINS is almost consistent with test data of Bartolomey. From the above results, it is revealed that the vapor generation model of the TAPINS gives reasonable results for the subcooled boiling phenomena.

4.2.3 Critical Flow Test

When a flow passage opens between the RCS and its environment by either a pipe rupture or some other mechanism, the fluid is expelled at a blowdown rate. A thermal-hydraulic system code requires the critical flow model to calculate the maximum discharge rate of coolant through a broken pressure boundary. The TAPINS employs the Henry-Fauske chocked flow model (1971) which requires only a knowledge of the stagnation conditions and at the same time accounts for the non-equilibrium nature of two-phase mixtures. The critical mass flux is obtained by solving the following set of equations for the chocking criterion and the critical flow expression as:

$$G_c^2 = \left[\frac{x_0 \upsilon_g}{nP} + (\upsilon_{gE} - \upsilon_{l0}) \left\{ \frac{(1-x_0)N}{s_{gE} - s_{lE}} \frac{ds_{lE}}{dP} - \frac{x_0 C_{pg}(1/n - 1/\gamma)}{P(s_{g0} - s_{l0})} \right\} \right]_t^{-1} \tag{4.7}$$

$$(1-x_0)\upsilon_{l0}(P_0 - P_t) + \frac{x_0 \gamma}{\gamma - 1}\left[P_0 \upsilon_{g0} - P_t \upsilon_{gt} \right] = \frac{\left[(1-x_0)\upsilon_{l0} + x_0 \upsilon_{gt} \right]^2}{2} G_c^2 \tag{4.8}$$

The solution procedure and the modification of the RELAP5 are implemented in the TAPINS (Ransom et al., 2001c). The model requires only the stagnation pressure and quality for calculation of mass flux.

The critical flow predicted by the TAPINS is compared to experimental data from University of California Radiation Laboratory (UCRL) as shown in Figs. 4.19 and 4.20. The good agreement is obtained between the TAPINS prediction and the data throughout the quality range investigated. Since the modification of the original model by RELAP5 accounts for the presence of a non-condensable gas, this model can also be applied to predict the two-component mixture discharge rate resulting from the rupture at the steam-gas pressurizer vessel.

4.2.4 Edwards Pipe Problem

The well-known Edwards pipe experiment (Edwards and O'Brien, 1970) is classified as the International Standard Problem No.1 used for evaluation of a thermal-hydraulic safety code. It is a transient blowdown test to simulate very fast depressurization of a heated, pressurized system. The TAPINS is applied to this benchmark problem to validate the vapor generation model and the critical flow model. The code capability on prediction of pressure wave propagation is assessed as well.

The schematic diagram of the test section is illustrated in Fig. 4.21. The apparatus consists of a straight pipe 73 mm in diameter and 4.09 m in length. The pipe is pressurized initially with 7000 kPa and 502 K water. Sudden rupture of a glass diaphragm is induced at one end, followed by the transit of a decompression wave through the test section. The exit area is reduced by 13 % due to fragments of the rupture disk remaining in the pipe. Pressures and local void fractions are measured in the test. The TAPINS model for Edwards pipe is depicted in Fig. 4.22. The test section is modeled by 20 identical volumes, and the discharge rate is calculated by Henry-Fauske model presented in the section 4.2.3.

The short-term results are compared to experimental data obtained at gauge stations 1 and 7 in Figs. 4.23 and 4.24. The propagation of the decompression wave from the open end to the closed end is predicted by the TAPINS, and the results are in good agreement with the data. The calculated decompression wave leads the data by about 0.5 ms at all gauge stations, but the almost constant difference may indicate the accurate prediction of the pressure wave. Actually, this trend is commonly observed in the simulations with other system codes (Hirt and Romeo, 1975; Carlson et al., 1980; Jeong and No, 1987), and thus one cannot rule out the possibility that the effective time of break initiation is slightly different than reported.

Another interesting observation is the large pressure undershoot at the gauge station 7 and the rapid rise again toward the saturation value in a short time. This undershoot is a result of vapor bubble formation; the nucleation interval results in the time duration observed in Fig. 4.24. Even though there is some deviation in the degree of undershoot, the phenomena is reasonably predicted by the TAPINS. The above short-term results reveal that the TAPINS well simulates the pressure wave transition and the flashing initiation.

The long-term results (0 to 500 msec) are plotted on Figs. 4.25 – 4.27 as pressure histories at gauge station 1, 5, and 7 respectively. After the drop to the saturation value by the decompression wave propagation, the pressure gradually decreases due to discharge of the internal fluid out of the pipe. The calculation results of the TAPINS are consistent with the experimental data.

The measured and calculated void fractions at gauge station 5 are plotted in Fig. 4.28 with the prediction of the MARS-KS. At earlier times up to 0.25 s, the calculated void fraction from the both codes deviates a little bit from the data. This deviation seems to be attributed to the over-calculation of the discharge rate from the Henry-Fauske critical flow model. For long-term void fraction, the prediction of the TAPINS agrees with the measured data.

4.3 Integral Effects Problems: RTF Tests

Since the conventional IETs on an integral reactor cannot provide the proper data for a fully-passive PWR as described in section 1.1.3, autonomous integral tests are performed in this study. An experimental program conducted in the RTF generates the data for the steady-state and transient behavior of an integral reactor on natural circulation. Using the RTF tests data, one is capable of performing the comprehensive validation of the TAPINS hydrodynamic models to predict the safety performance and the transient behaviors of a fully-passive integral PWR. In what follows, the description of the test facility and the calculation results of the TAPINS are presented.

4.3.1 Description of Test Facility

To investigate the thermal-hydraulic phenomena and the system responses of a passive integral PWR during the postulated transients, a series of IET are carried out at a scaled-down apparatus called the RTF (Jang et al., 2011; Lee et al., 2012). The RTF is a scaled test rig of REX-10 that was designed to evaluate the characteristics of natural circulation under steady-state and transient conditions and simulate the thermal-hydraulic system behavior during hypothetical accidents. Figure 4.29 is the picture of the RTF apparatus.

Since testing programs of the RTF include the rapid system depressurization accompanying the two-phase phenomena, the two-phase similarity law has to be taken into account. Therefore, in this study, the scaling method proposed by Kocamustafaogullari and Ishii (1987) has been used when scaling the major design parameters for the RTF. Table 4.5 lists the major scaling factors of RTF.

The homologous relationship between the RTF and REX-10 was determined from the constraints on available space and power. As the top priority of the RTF is placed on the system operation under natural circulation condition, the height ratio is kept unity so that the facility can provide an identical hydrostatic head to that of REX-10 for free convection. In addition, it is not difficult to designate the full-pressure facility on account of relatively low system pressure of REX-10. The volume scale ratio is set to 1:50. Then from the basic principles of geometric, kinematic, dynamic, and energy density similarity, the scale ratios for area (1:50), time (1), velocity (1), and the power (1:50) have been determined as shown in Table 4.5. In short, the RTF is the full-height full-pressure facility with reduced power.

A. Primary System

The RTF models all system components of REX-10 housed in the reactor pressure vessel. The primary circuit of the RTF consists of electrical heaters, a riser, four hot legs, and a helical-coil heat exchanger as shown in Fig. 4.29. It is designed to operate at full pressure (2.0 MPa) and temperature (200 ^{o}C) with a maximum heater power of 200 kW. The reactor vessel, which is 5.71 m in height including the steam-gas pressurizer vessel, is made of the type 304 stainless steel and its elemental wall thickness is decided on the basis of ASME Boiler and Pressure Vessel Code section III (ASME, 1986) to withstand the high pressure condition.

Figure 4.30 illustrates the integral configuration of the system components in the RTF. The core region consists of 60 electrical heaters arranged in the square array. The pitch-to-diameter ratio of heater rods is 1.167 and the effective heated length is 1.0 m, as identical to REX-10. The primary coolant heated in the core passes the long riser and flows into the annular space through the four hot legs. Not appearing in the prototypical REX-10, these elbow-shaped hot legs are set up to install flowmeters to measure the natural circulation flow rate, causing major distortion in the similarity between the RTF and REX-10.

The once-through heat exchanger, whose active length is 1.205 m, comprises twelve helical tubes arranged into 3 columns. Each coil is 7.746 mm in inner diameter, 9.525 mm in outer diameter, and approximately 4.38 m in length. The innermost, intermediate, outermost column are composed of 3, 4, 5 helical tubes, respectively. The helical coils wrap around the entire annulus between the core barrel and the reactor vessel wall. The primary coolant flows downward across the tube bundles and transfers heat to the secondary coolant flowing inside the tubes. Located at the lowest region of RTF is the lower plenum through which most instrumentation around the core is inserted.

In the “phase 1” of the RTF experimental program previously performed by

Jang et al. (2011), the steam-gas pressurizer was not equipped as it stands in REX-10 since the experiments were planned primarily to estimate the free convection capability of REX-10. At this stage, the pressurizer vessel was connected to the top of the RTF through a long, narrow pipe, and the non-condensable gas was not inserted in the gas region as well. Instead, the system pressure was regulated by controlling the internal electrical heaters, which are installed inside the pressurizer vessel and submerged in water, to evaporate the water. In this case, the pressurizer and the RCS are fairly non-communicative and the performance of the steam-gas pressurizer in the presence of non-condensable gas cannot be examined.

Thus, in this testing program called "phase 2", the pressurizer module is altered in a way that the pressurizer vessel is directly placed on the top of the RTF as shown in Fig. 4.31 so that the function of the steam-gas pressurizer can be simulated (Lee and Park, 2012). A couple of instrumentations are also employed in the steam-gas pressurizer, and the nitrogen injection line and the gas vent line, branched off by a union tee, are linked to the upper side of the pressurizer vessel for regulation of the fluid inside. The vent line provides the gaseous mixture with the passage to a condensing tank when breaking the pressure boundary in SBLOCA experiment or depressurizing the RTF system after the experiment is finished.

The cylindrical vessel of 0.381 m in diameter and 0.873 m in height is heavily insulated. The effective pressurizer region may be regarded as the whole volume above the top of hot legs. For visualization of water level in the pressurizer, a small rectangular chamber with a transparent window pane disposed on one side of wall is installed as well.

B. Secondary System

In the RTF, the helical tubes of steam generator form a closed loop with three air-cooled type chillers as the secondary circuit. The secondary feedwater at the atmospheric pressure from the chillers enters into the helical tubes and flows up. The coolant is heated up passing through the heat transfer region and flows back into the chillers. Each chiller recirculates water through the tubes of a specific column, and the coolant is split into the coils at the water distributor. While the feedwater turns into the saturated steam when leaving the coils in REX-10, the secondary coolant is maintained in the subcooled state at whole channels in this experiment by setting up the proper mass flow rate. The flow rate of each helical coil is controllable by a ball valve located ahead of the tube entrance. When the cooling capability of a chiller is not sufficient to keep the feedwater temperature constant, a portion of hot water from helical tubes can be drained before returning to the chiller while continuously supplying tap water to the reservoir in the chiller.

C. Instrumentation

Major subsections of RTF are instrumented so that system parameters can be measured and recorded during experiments. In the RTF, a total of 32 K-type thermocouples with error limits of 0.75 % acquire the temperature data at various positions of the primary and the secondary circuit. For the primary system inside the reactor vessel, the inlet and outlet temperatures of the core and the steam generator as well as the temperatures at the downcomer and the lower plenum are measured. Especially, three thermocouple sensors are uniformly distributed in the azimuthal direction at the core inlet and outlet, respectively, to obtain the mean temperature of the cross section. Two thermocouples installed at the steam-gas pressurizer measures the temperature of the liquid and the gaseous mixture. The feedwater temperatures of each tube column and outlet temperatures of each helical coil are also measured.

The mass flow rate by natural circulation is measured using the turbine flowmeters installed at the hot legs. The flow channel inside the flowmeter is just 9 mm in diameter, establishing very narrow flow path. The feedwater flow rate into a tube is checked out by the variable area flowmeters, but not recorded by the data acquisition system. Beside the pressure gauge, the pressure transmitter is installed at the top of the pressurizer vessel to record the system pressure. Another pressure transmitter is used to evaluate the water level in the pressurizer from the differential pressure.

D. Experimental Procedure

Prior to beginning each run of the transient experiments, the system has to be brought to the steady-state condition while continuously supplying the core power and the feedwater for heat removal. Figure 4.32 shows a typical path that the thermodynamic state of the coolant gets stabilized until arriving at heat balance condition.

At first, the tap water is injected into the RTF; the initial water inventory is determined by the requirement that the pressurizer volume is filled half-full with water when the system is heated up and reached to the steady-state. The data acquisition system is then initiated and the desired amount of nitrogen gas is injected to the upper volume of the steam-gas pressurizer. Nitrogen injection at the very early phase of experiments is intended to prevent the bulk boiling of the coolant during heat up. When deciding the amount of nitrogen required, one have to take into account not only the rise in the partial pressure of non-condensable gas but also the changes in the volume of gaseous mixture due to the expansion of RCS coolant as the system is heated up.

The maximum heater power (approximately 180 kW) is applied to the core in order to increase the temperature of liquid in the pressurizer, which governs the partial pressure occupied by the vapor, up to the highest point in this apparatus. It results in the immediate rise in the core exit temperature, and the chiller is turned on subsequently. Then the coolant temperature and the system pressure gradually increase until heat balance equilibrium is established, i.e. the pressure and the temperature profile of the primary circuit are invariant with time. The transient experiments are initiated from the steady-state condition, and pressure, coolant flow rate, temperature, and water level are recorded until the temperature of hot fluid goes down below 100 ^{o}C.

4.3.2 Steady-state Natural Circulation

The experimental results presented in this section results from the RTF experimental program phase 1, in which the primary priority is place on the evaluation of the natural circulation capability of REX-10. The steady-state mass flow rate produced by natural circulation in the primary circuit is simulated at 2.0 MPa. In the tests, the mass flow rate and coolant temperatures are measured at various core powers while the primary system pressure is kept constant by regulating the power of the heaters equipped inside the pressurizer. In all cases, the secondary feedwater at 20 ^{o}C and 1 bar is sent into the helical coil at a rate of 4.5 LPM per tube. The heat loss to the surrounding environment is estimated to be less than 5 %.

In the simulations of the TAPINS, a total of 37 nodes constitute the primary circuit of the RTF; nodes for the core (5), riser (5), upper head including hot legs (8), S/G (14), downcomer (3), and lower plenum (2) establish the RCS of the RTF as illustrated in Fig. 4.33. In particular, fine nodalization is prepared for the helical coil S/G section in an attempt to assure the precise prediction of the heat transfer with coolant. Minor losses due to an abrupt change in flow area are calculated from the relevant empirical correlations (Todreas and Kazimi, 1990). Only when the heat removal rate from the S/G is the same as the input power do the thermal-hydraulic variables converge to their fully stabilized values.

The simulation results predicted by the TAPINS for the steady-state mass flow rate are compared with experimental data from six tests performed using different core powers, as shown in Fig. 4.34. Undoubtedly, the higher the power generated by the core, the greater the natural circulation flow since a high input power increases the temperature gradient of the coolant, and subsequently, the buoyancy force that arises due to the density differences. It is observed that, even though the difference in midplane elevations between the core and the S/G is almost 2.5 m, the mass flow rate is less than 0.5 kg/s for the power ranges used in this study. This low natural circulation flow of the RTF is attributed to the enormous flow resistance applied by hot legs and the flowmeter where the fluid passes through a very narrow flow channel. Inspection of Fig. 4.34 reveals that the steady-state flow rates predicted by the TAPINS show excellent agreement with the data; the maximum deviation is at most 4.2 %.

This analytical solution expressed as Eq. (4.5) is also plotted versus the core power in Fig. 4.34 to provide comprehensive estimates of the stabilized conditions of the RTF. All parameters appearing in Eq. (4.5) are evaluated using the steady-state conditions for an experiment at 141.55 kW. It is shown that the predictions of the TAPINS are very close not only to the experimental data but also to the results of the analytical calculation. The deviation from the curve observed at powers lower than 100 kW results from the dependence of the overall flow resistance and thermophysical properties on Reynolds number and temperature, respectively. In fact, Eq. (4.5) tells us that the mass flow rate is proportional to the total heat input to the power of 1/3, assuming that the flow resistance and temperature profile of the primary system are constant. In reality, a substantial inaccuracy in this calculation may be induced unless the exact distributions of the flow velocity and the fluid temperature are reflected in each case.

The simulation results for coolant temperatures are listed in Table 4.6, along with the measured values from the tests. Compared to the experimental data, the maximum deviation is less than 2.6 K. The equilibrium temperature distribution in the RCS is closely associated with the cooling capability of the heat exchangers. For example, if the calculated heat transfer rate from the primary system to the S/G tubes is lower than the core power, the overall coolant temperatures will gradually increase until heat balance equilibrium is established. Therefore, the results presented in Table 4.6 demonstrate that the incorporated S/G model works very well for predicting the shell-side and tube-side heat transfers across the helical tubes.

4.3.3 Changes in Core Power

Using the RTF, several transient experiments were also carried out by Jang et al. (2011). As the RTF is designed basically for steady-state tests on the natural circulation, not many parameters are controllable in these experiments. However, since the core power and the feedwater flow rate can be easily regulated, three transient tests investigating changes in these factors are presented in this paper: an increase in core power, a reduction in core power, and a reduction in feedwater flow. Through comparison with the transient data obtained from the transient natural circulation tests, the assessments of the predictive capability of the TAPINS can be conducted.

Figures 4.35 and 4.36 show the variation of the coolant flow rate and temperatures when the core power abruptly dropped by half from a stabilized state. At 200 s, the core power is reduced from 138.6 kW to 71.2 kW in a ramp type drop for 40 seconds. One has to remember that the heat transport between the fluid and the internal structures is not trivial in this kind of scaled-down test rig, especially when a dramatic temperature change occurs in the fluid. The stored energy in the structural wall may serve as a heat source during transients, or the relatively cooler internals may absorb a lot of heat from the fluid. In particular, the thermal-hydraulic behavior of the RTF is characterized by a low flow rate and a large temperature rise, and thus the heat transfer with the structural wall has to be modeled. For transient simulations of the TAPINS, the heat exchange with the reactor internals is modeled using a lumped approach as follows:

$$M_s C_s \frac{dT_s}{dt} = -\alpha A_s (T_s - T_\infty) \tag{4.9}$$

The outer surfaces of the walls are assumed to be adiabatic, and the same heat transfer correlations are used as in the core heat transfer models. The sensitivity study revealed that the modeled coolant flow underwent premature changes in flow rate and temperatures unless the effect of the structural wall was taken into account. In simulations of the reduction in core power, the heat transfer rate from the wall instantaneously reached 12% of the time-dependent core power.

In this transient, the reduction in core power is followed by a rapid drop of the natural circulation flow. As the flow velocity is lowered, the temperature rise across the core is somewhat increased, causing a slight overshoot in the coolant flow rate by enhancing the driving force of the free convection. Then the flow rate and the temperatures slowly decrease until a new stabilized state is established. The TAPINS succeeds in predicting the aforementioned flow pattern set up by natural circulation and the transient behavior of the coolant temperatures with fine accuracy, as shown in Figs. 4.35 and 4.36. The outlet temperature of feedwater is also plotted in Fig. 4.37. Since it is a direct indication of time-dependent heat transport to the secondary system, Fig. 4.37 proves that the TAPINS predicts the heat transfer in the helical coil S/G fairly well.

As a similar transient case, the simulation results of an increase in core power are plotted in Figs. 4.38 and 4.39 along with corresponding experimental data. Over 40 seconds, the core power rose from 69.5 kW to 142.75 kW at 200 s. Immediately after the sudden increase in heat input, even though the up-and-down behavior of the flow rate is more conspicuous in the simulation result, the analysis capability of the TAPINS seems quite acceptable.

4.3.4 Reduction in Feedwater Flow Rate

The remaining transient is initiated by reducing the feedwater flow rate into the helical tubes. The ball valves located at the entrance of the helical coils are partially closed so that the flow rate in each tube is reduced from 4.5 LPM to 2.7 LPM. The experimental data and the simulation results are plotted in Figs. 4.40 and 4.41. As the reduction in feedwater flow rate causes a slight decline of the heat transfer in the tube-side, the heat input from the core takes a while to be completely removed from the S/G. According to the simulation by the TAPINS, the cooling rate at the shell-side of the helical tubes is reduced to a minimum of 85% of the core power. In the meantime, the average temperature of the RCS gradually goes up due to the power-cooling mismatch. While the heat removal returns to its normal level, the outlet temperature of the feedwater also increases until it reaches a new steady-state.

Compared to the previous transients caused by the changes in the core power, it is noted that the effect of the feedwater flow rate is relatively insignificant in this transient. In fact, Eq. (4.5) describes cases for which the total input power is equal to the amount of heat removed, and the details of the heat transport to the heat sink are not so predominant in determining the free convective flow rate in the transients. Nevertheless, the TAPINS effectively estimates the qualitative behavior of the primary system in the transient, as shown in Figs. 4.40 and 4.41.

4.3.5 LOFW Accident

The TAPINS application to the LOFW accident of the RTF is presented in this section. This test simulates a hypothetical accident induced by the complete loss of feedwater flow in which the S/G is no longer serves as a heat sink until a protective system is actuated. This loss of total feedwater flow can be caused by a mechanical seizure or a power failure of the feedwater pumps, or an inadvertent closure of the feedwater control valves due to malfunction of a feedwater control system.

When an actual reactor system is encountered to the LOFW accident, the reduced feedwater flow rate immediately triggers the reactor trip. In this test, however, a more conservative scenario is assumed that the low feedwater flow trip is not actuated but the high pressurizer pressure trip resulting from the coolant heatup leads to reactor shutdown. Once the pressurizer pressure reaches 2.3 MPa, a trip setpoint of REX-10, the heater power is dropped to the decay heat level (about 7%) and the chillers are turned on again to simulate the actuation of the PRHRS. Since the PRHRS is neither established in the RTF system nor designed in detail for REX-10, it is assumed that natural circulation flow rate of PRHRS is maintained constant at 1/9 of the nominal feedwater flow rate.

In the analysis of the LOFW accident, the prediction on transient response of the steam-gas pressurizer dominantly affects the overall calculation results; if the TAPINS fails to estimate the accurate moment of reactor trip under the situation in which the heat removal from the RCS completely vanishes, the calculation results will considerably deviate from the data. The prediction results of the TAPINS are shown in Figs. 4.42 – 4.45.

After the chillers are turned off, the coolant is heated up at the rated power as the heat sink vanishes, and the corresponding expansion of RCS coolant and rise in the partial pressure of vapor in the upper gaseous mixture lead to the fast increase in the pressurizer pressure. Due to the absence of a heat sink, the natural circulation flow rate is reduced quite fast as well. At 240s after the initiation of transient occurs the reactor trip, and accordingly, the simulated residual decay heat and PRHRS flow is provided. Then the coolant temperatures and the water level are gradually decreased on account of the continuous cooldown by the PRHRS.

The moment of overpressure trip predicted by the TAPINS is about 20 sec later than the experiment. The deviation is not remarkable in a view of long-term transient, which indicates that the steam-gas pressurizer model incorporated in the TAPINS provides the reasonable prediction. The calculation result of the pressure transient after the core trip is also consistent with the test data. In addition, the predicted variation in the pressurizer water level is in good agreement with the experiment.

Figures 4.44 and 4.45 show the natural circulation flow rate and the change in coolant temperatures in the LOFW accident. The mass flow rate is greatly reduced after the reactor trip, and the RCS coolant is continuously cooled down by the simulated PRHRS function. The results from the TAPINS are in general agreement with the data. In the natural circulation regime where the fluid velocity is very low, the calculated flow rate is slightly lower than the measured one. It is attributed to the deviation of the friction factor for low-velocity natural circulation flow, and it also affects the prediction of the coolant temperatures. Since the forced flow correlations are not generally valid in natural circulation flows (Zvirin, 1981), it needs to improve the friction coefficient models in the TAPINS.

The calculation results of the TASS/SMR are also plotted in Figs. 4.42 – 4.45. The TASS/SMR predicts that the reactor trip occurs at 356s after the initiation of transient; it is nearly 2 minutes later than measured. As shown in the results, the inaccurate prediction of the pressure transient in the steam-gas pressurizer causes significant deviation in overall RCS parameters. It is closely associated with the capability of the TASS/SMR in predicting the pressure response of the steam-gas pressurizer. Since the period of the coolant heatup without heat sink is much longer in the calculation of the TASS/SMR, the coolant temperatures and the pressurizer water level go up far higher than the data. In short, the calculation results of the TASS/SMR exhibit considerable deviation from the experimental data due to inaccurate prediction of the overpressure trip.

From the comparison with IET data of LOFW accident, it is assessed that the TAPINS can provide reasonable prediction on the transient response of the steam-gas pressurizer as well as the RCS behavior of a fully-passive integral PWR.

Table 4.1 Assessment matrix of the TAPINS

Category	**Problem type**	**Assessment objectives**
Verification Problems	Mass and energy conservation problem	Truncation errors
	Natural circulation problem	Free convection phenomena
SET	MIT pressurizer tests	Steam-gas pressurizer model
	Subcooled boiling tests (Christensen / Bartolomey experiments)	Vapor generation model (~slug / ~annular flow regime)
	Critical flow tests (UCRL)	Chocking model: Henry-Fauske
	Edwards pipe problem	Vapor generation, chocked flow
IET	RTF tests (Natural circulation / LOFW)	Comprehensive analyses on a fully-passive integral PWR

Table 4.2 Comparison of computed natural circulation flow to analytical solution

Water properties @ 20 bar, 100 °C $\overline{\rho}$: 959.2 kg/m^3 β : 7.48 × 10^{-4} /K C_p : 4212.3 J/kg·K		**Parameters** Δz =0.3 m $R = \sum_j \frac{K_j}{A_j^2}$: 1.297 × 10^4 m^{-4}	
Power (kW)	**Analytic (kg/s)**	**TAPINS (kg/s)**	**Error (%)**
2.5	0.57013	0.57092	0.139
5.0	0.71832	0.72030	0.276
7.5	0.82227	0.82564	0.410
10.0	0.90502	0.90993	0.542

Table 4.3 Test conditions of Christensen experiments selected for analysis

Run No.	**Pressure (bar)**	**Power (kW)**	**Mass flux (kg/m^2s)**	**Temperature (K)**	**Inlet subcooling (K)**
10	27.6	30	646.9	493.7	8.7
11	41.4	50	940.0	511.1	14.4
15	55.1	70	907.2	530.8	12.5
16	68.9	70	807.7	545.9	12.1

Table 4.4 Test conditions of Bartolomey experiments selected for analysis

Index	**Pressure (bar)**	**Heat flux (kW/m^2)**	**Mass flux (kg/m^2s)**	**Inlet subcooling (K)**
1	30.1	980	990	62.2
2	44.1	900	994	66.3
3	68.4	1130	961	91.4
4	108.1	1130	966	87.9

Table 4.5 Major scaling factors of the RTF

Parameters	**Similarity requirement**	**Scale ratio**
Pressure	P_R	1
Height	l_{0R}	1
Volume	$a_{0R}\, l_{0R}$	1/50
Area	a_{0R}	1/50
Aspect ratio	$l_{0R}\, d_{0R}^{-1}$	7.07
Time	$l_{0R}^{1/2}$	1
Velocity	$l_{0R}^{1/2}$	1
Power	$a_{0R}\, l_{0R}^{1/2}$	1/50

Table 4.6 Steady-state coolant temperature in the RTF at various core powers

Power (kW)	**Core outlet**		**Core inlet**		**Feedwater outlet**	
	Exp.	**Code**	**Exp.**	**Code**	**Exp.**	**Code**
70.55	106.95	106.87	50.63	49.57	37.49	38.79
99.70	128.21	128.72	60.47	59.38	45.56	46.58
141.55	157.98	156.45	74.15	72.37	56.90	57.76
145.75	159.97	159.07	75.14	73.60	58.44	58.87
170.10	174.36	173.68	83.31	80.71	65.04	65.37
172.45	176.89	175.06	82.95	81.44	65.64	65.99

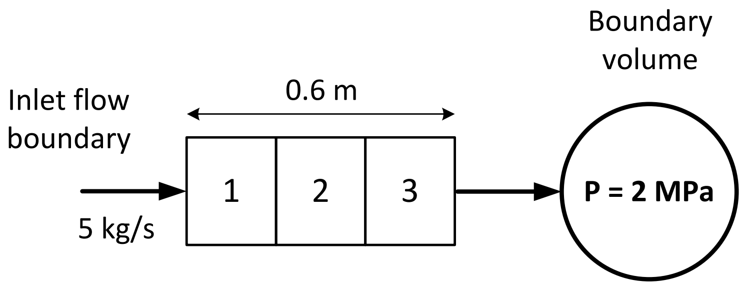

Figure 4.1 TAPINS model for mass and energy conservation problem

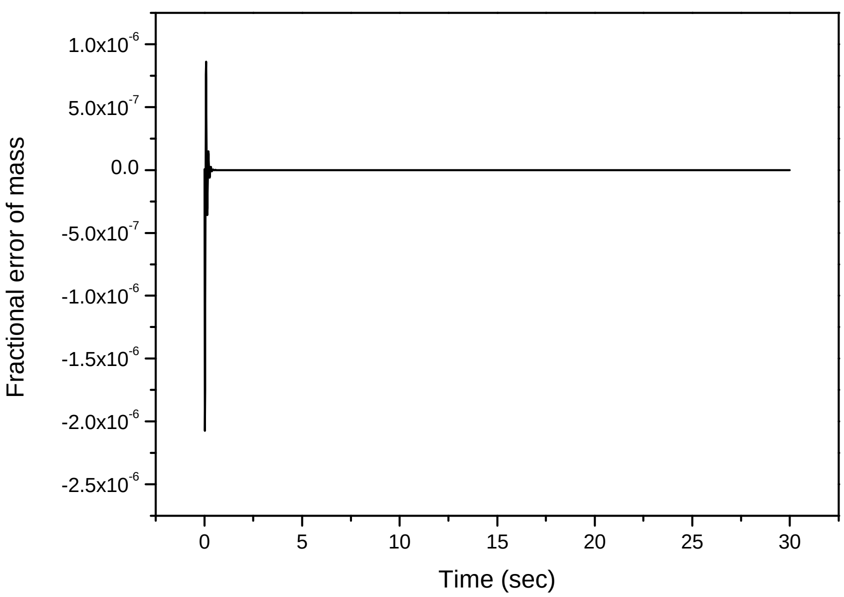

Figure 4.2 Fractional mass error for single-phase liquid flow

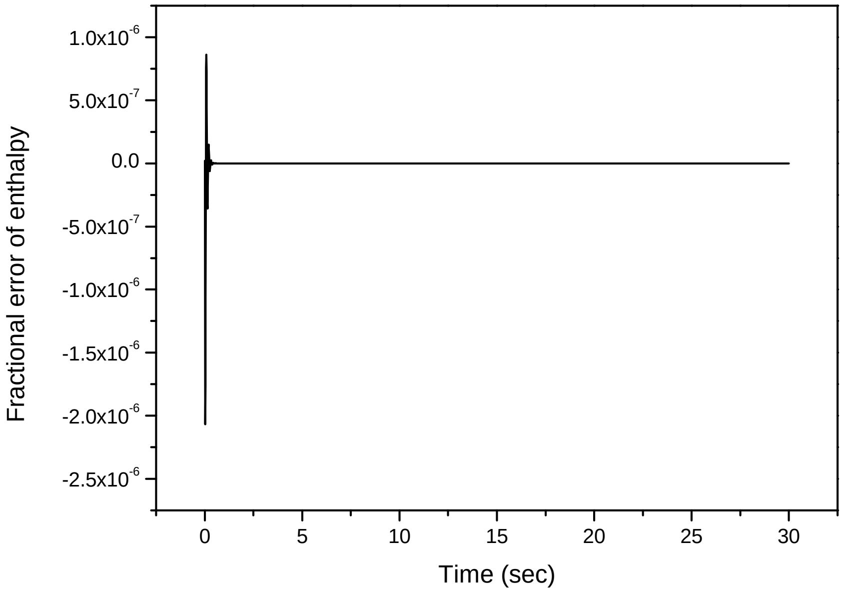

Figure 4.3 Fractional energy error for single-phase liquid flow

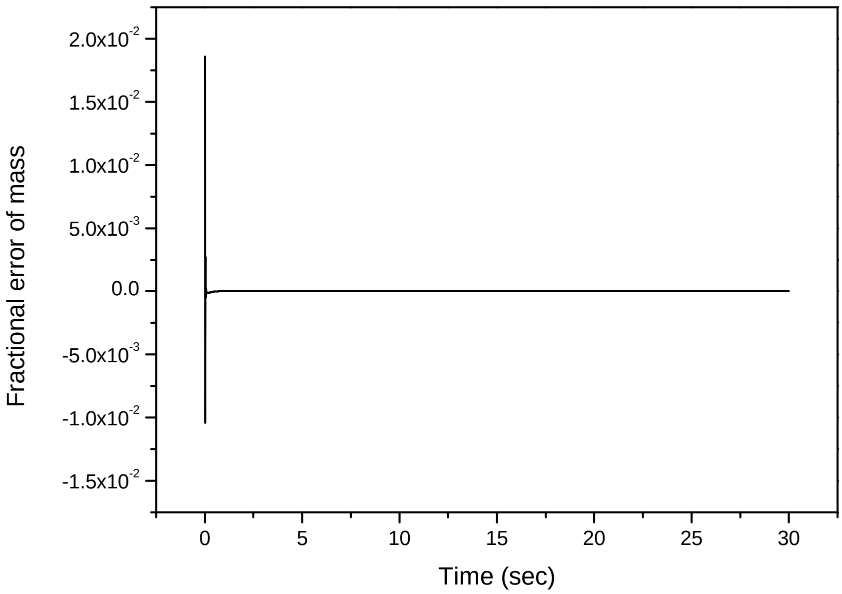

Figure 4.4 Fractional mass error for two-phase flow

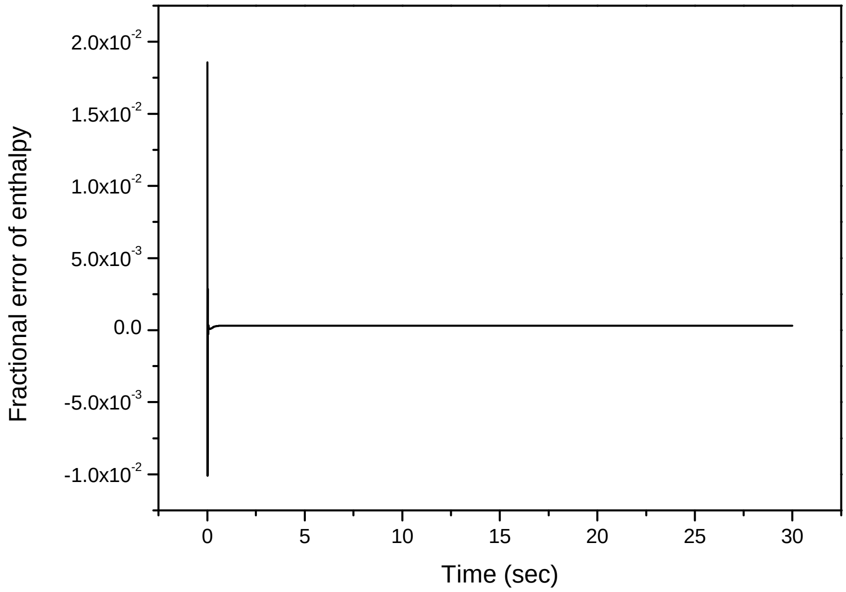

Figure 4.5 Fractional energy error for two-phase flow

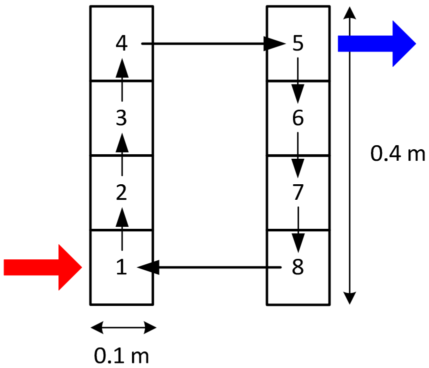

Figure 4.6 TAPINS model for natural circulation problem

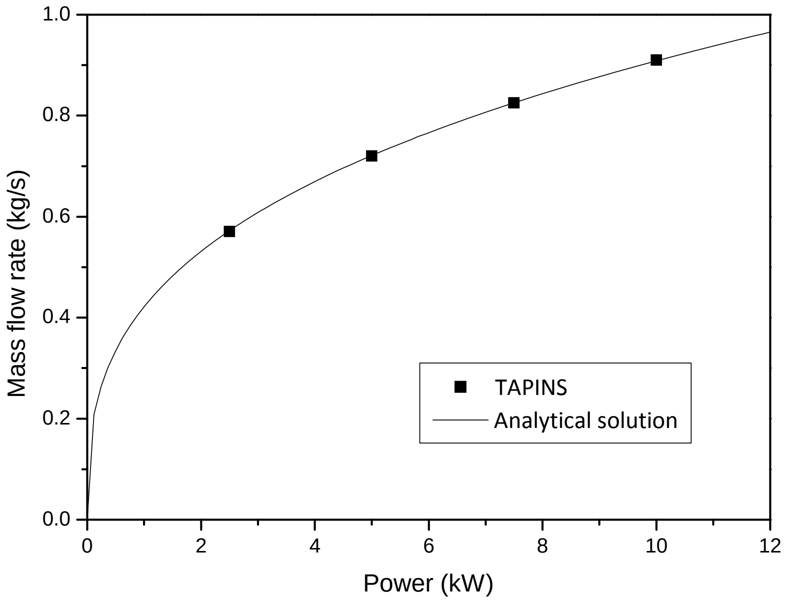

Figure 4.7 TAPINS prediction and analytical solution of natural circulation

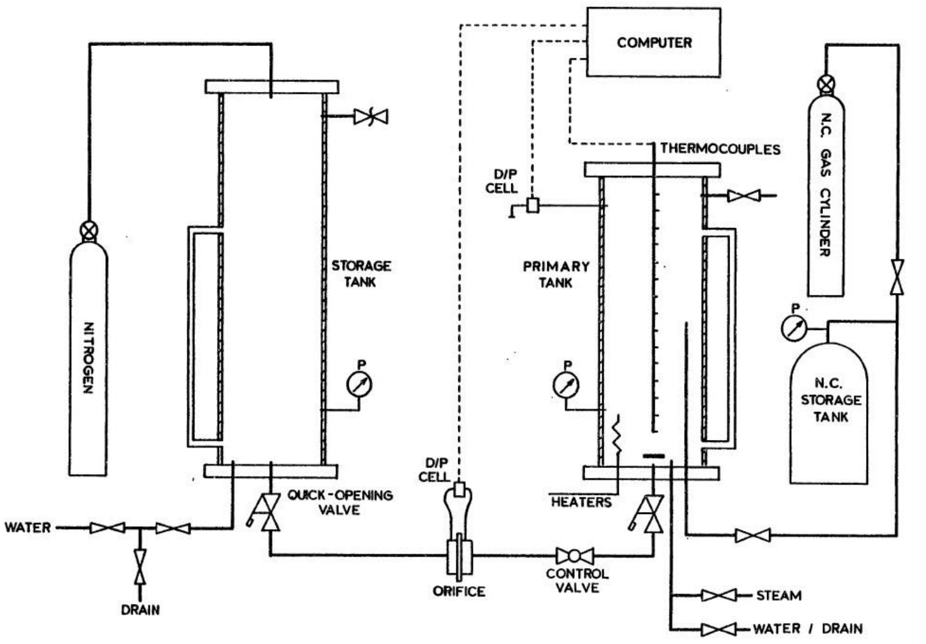

Figure 4.8 Schematic diagram of MIT apparatus

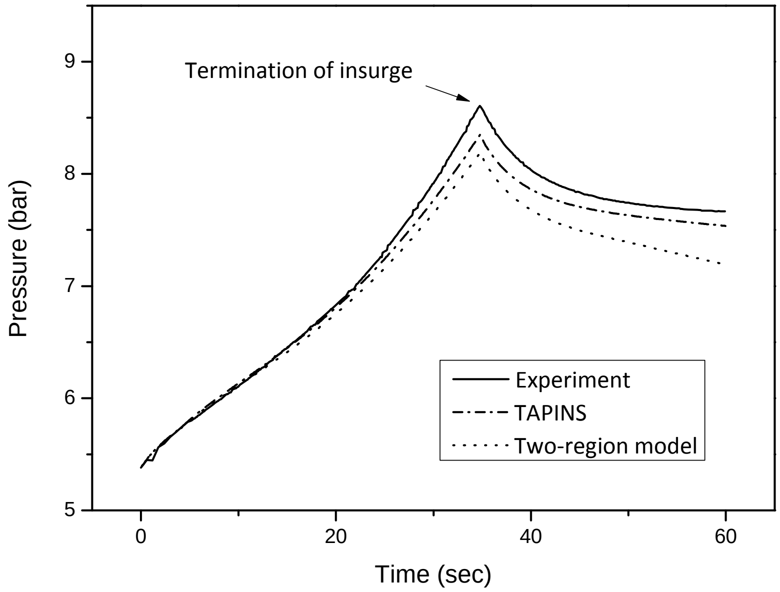

Figure 4.9 Pressure responses to insurge with nitrogen present (N_2 ratio: 10 %)

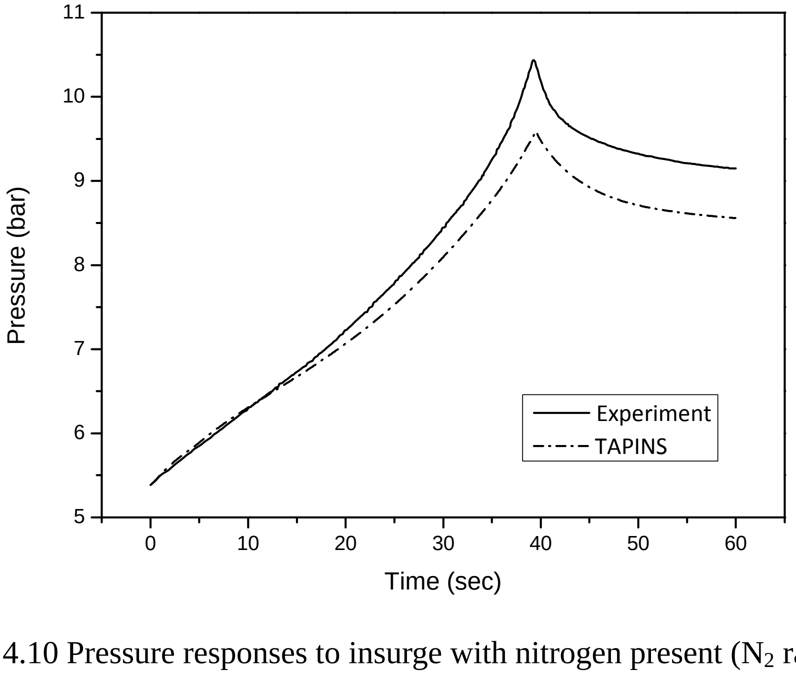

Figure 4.10 Pressure responses to insurge with nitrogen present (N_2 ratio: 20 %)

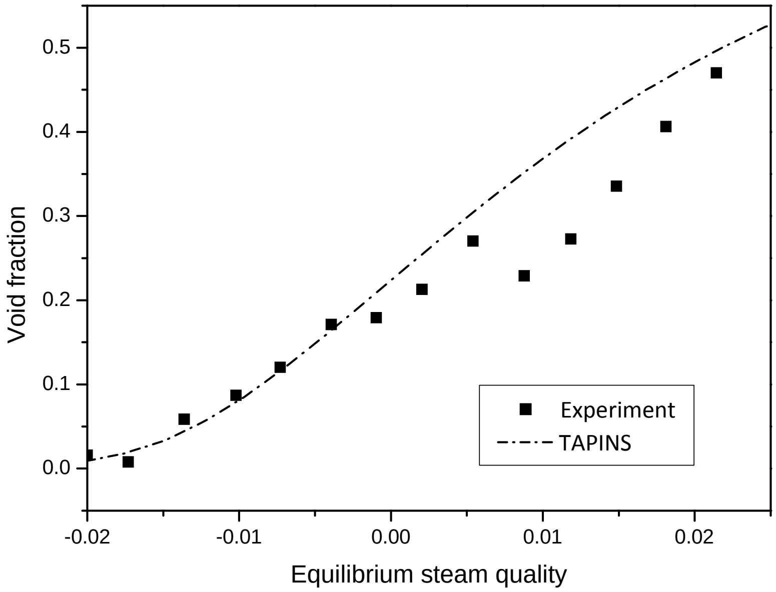

Figure 4.11 Comparison of TAPINS with Christensen Run 10

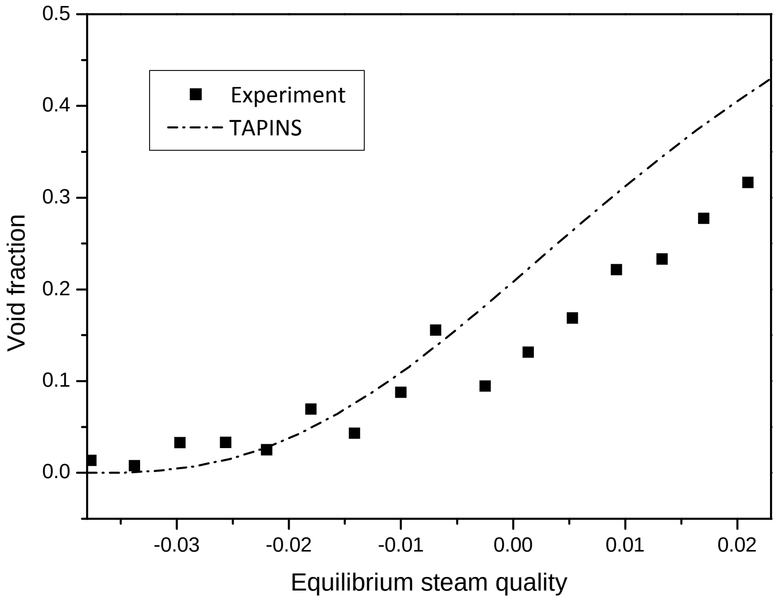

Figure 4.12 Comparison of TAPINS with Christensen Run 11

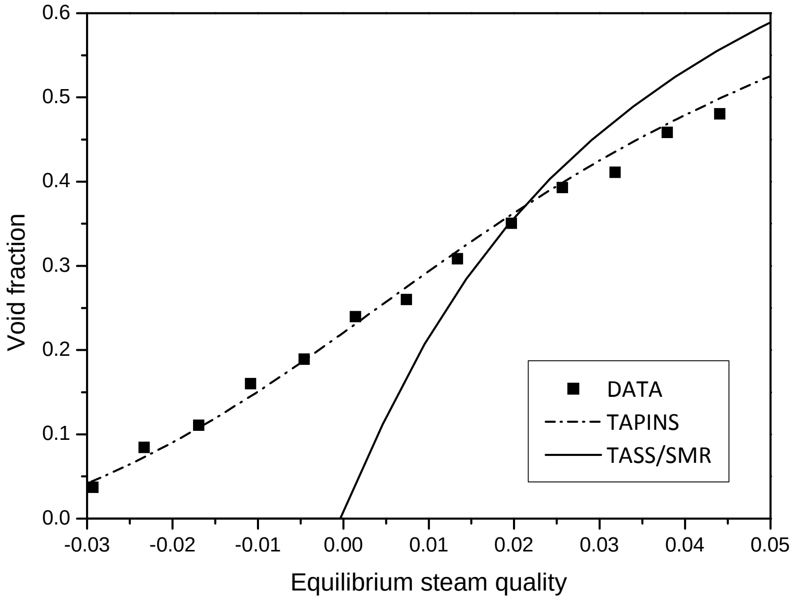

Figure 4.13 Comparison of TAPINS with Christensen Run 15

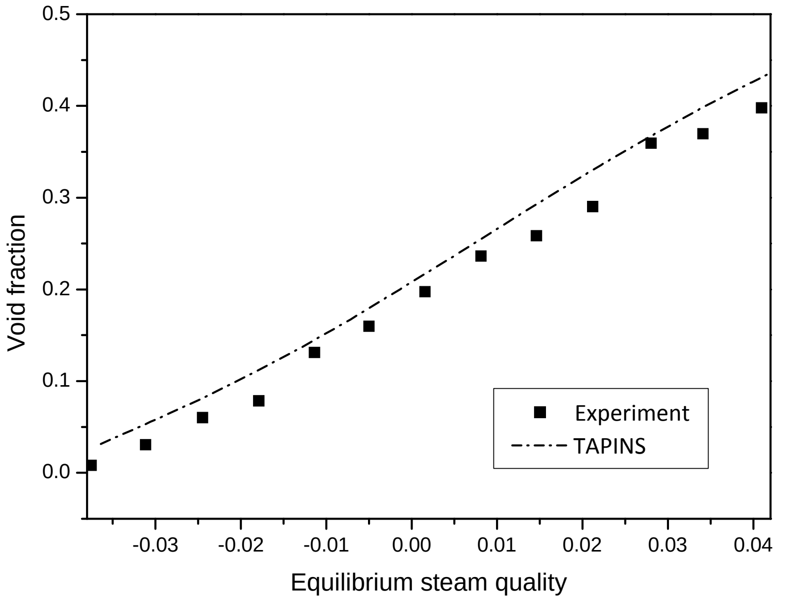

Figure 4.14 Comparison of TAPINS with Christensen Run 16

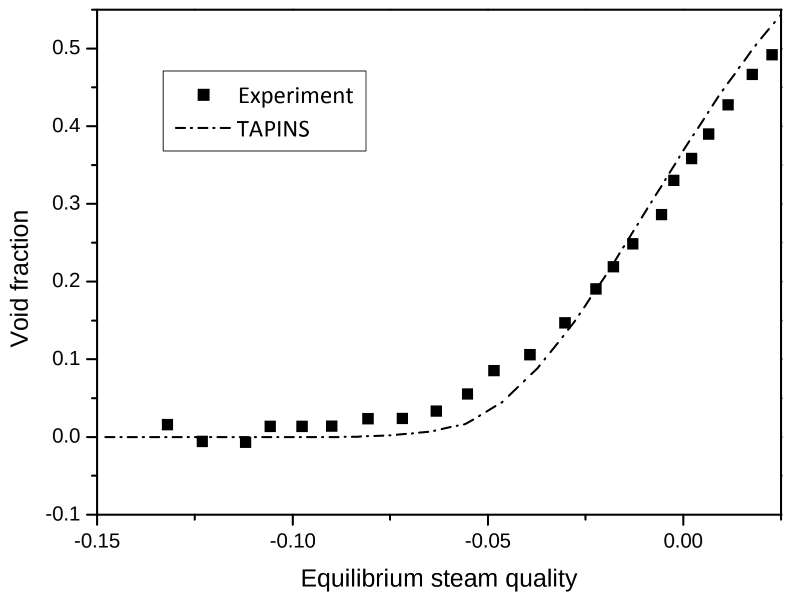

Figure 4.15 Comparison of TAPINS with Bartolomey test at 30.1 bar

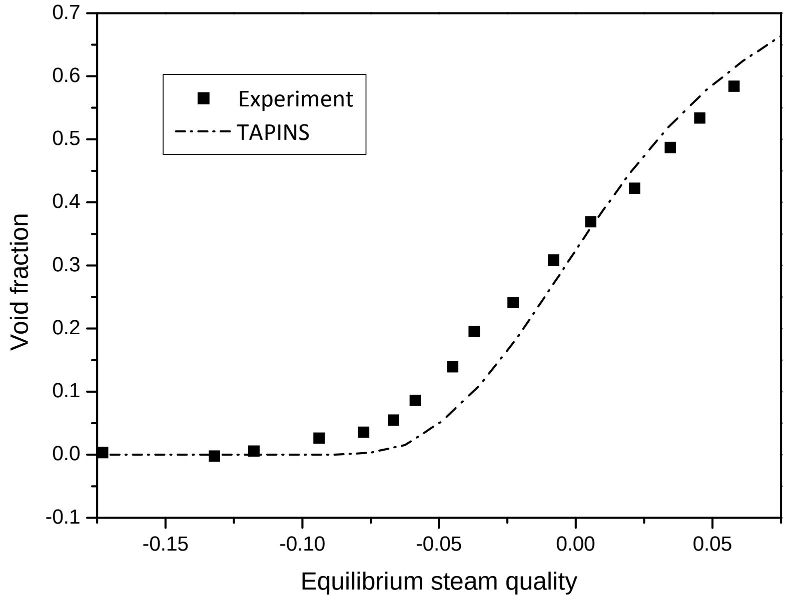

Figure 4.16 Comparison of TAPINS with Bartolomey test at 44.1 bar

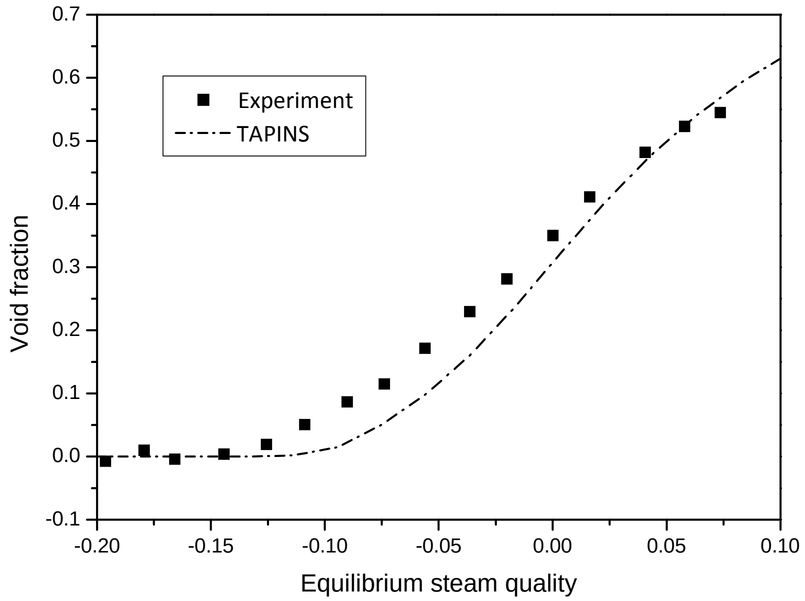

Figure 4.17 Comparison of TAPINS with Bartolomey test at 68.4 bar

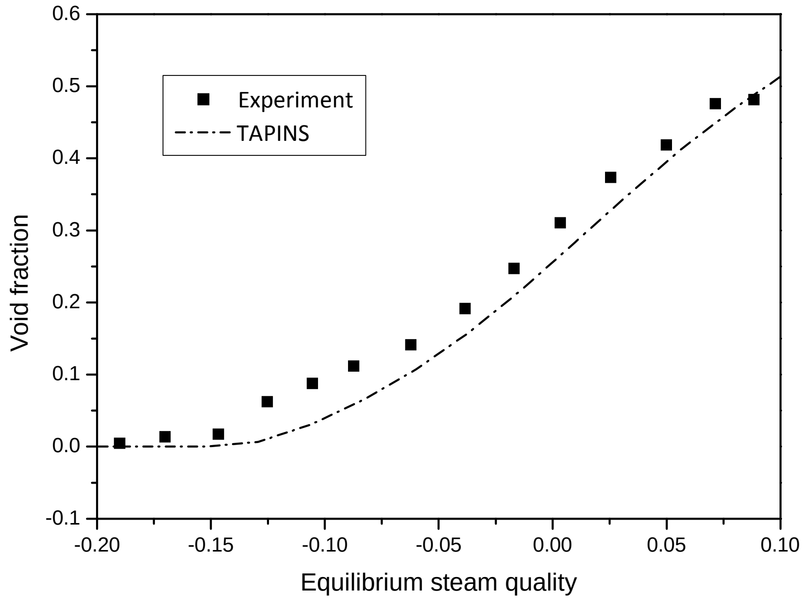

Figure 4.18 Comparison of TAPINS with Bartolomey test at 108.1 bar

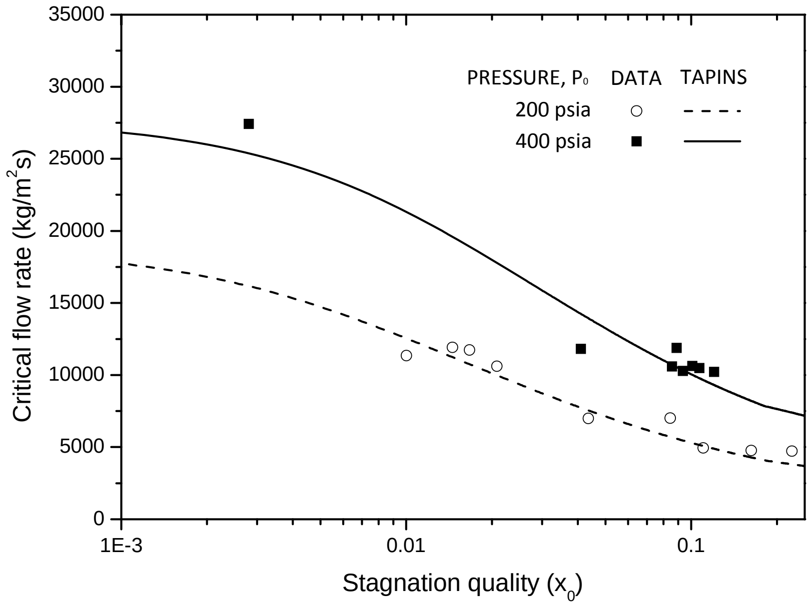

Figure 4.19 Comparison of TAPINS with UCRL critical flow test (1)

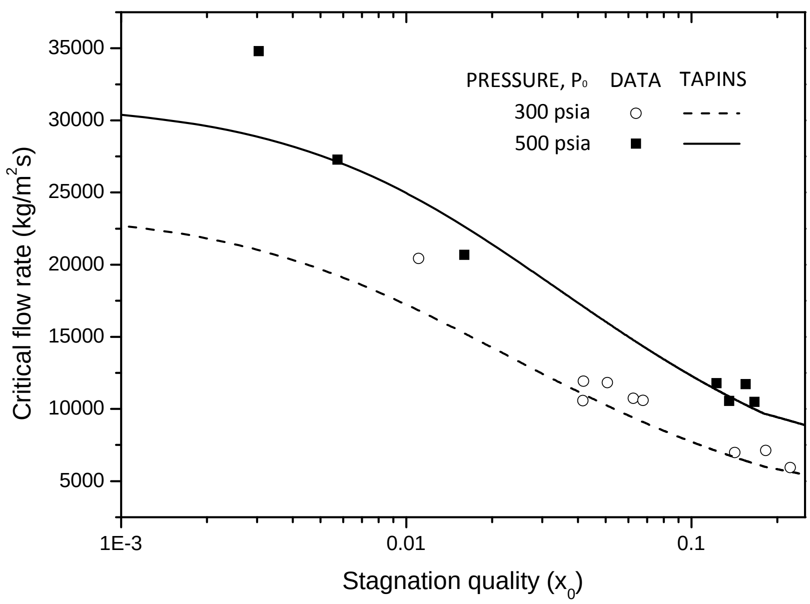

Figure 4.20 Comparison of TAPINS with UCRL critical flow test (2)

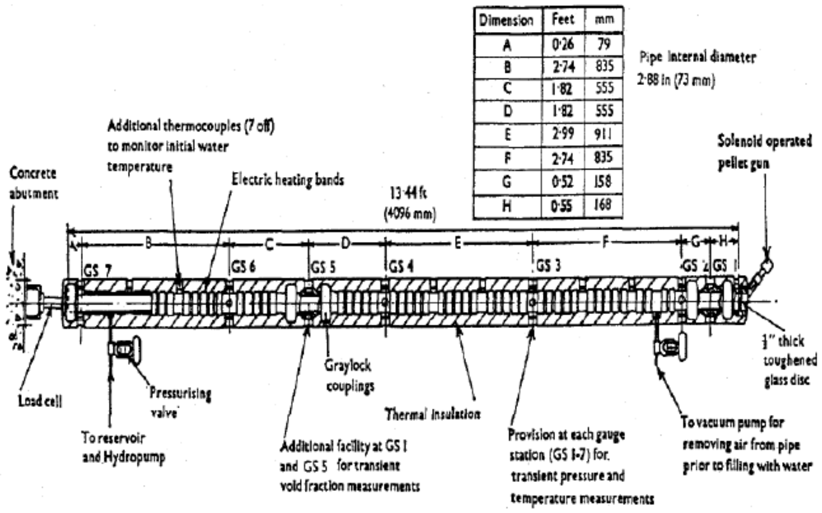

Figure 4.21 Schematic diagram of Edwards pipe experiment apparatus

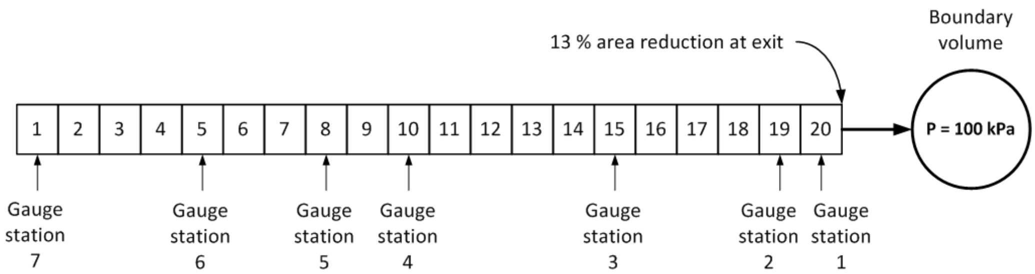

Figure 4.22 TAPINS nodalization of Edwards pipe

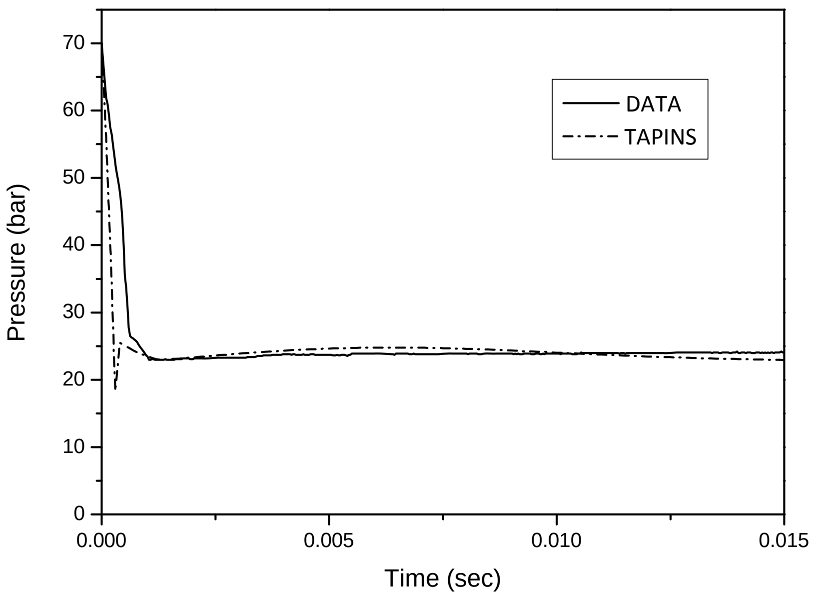

Figure 4.23 Edwards pipe short term pressure transient at gauge station 1

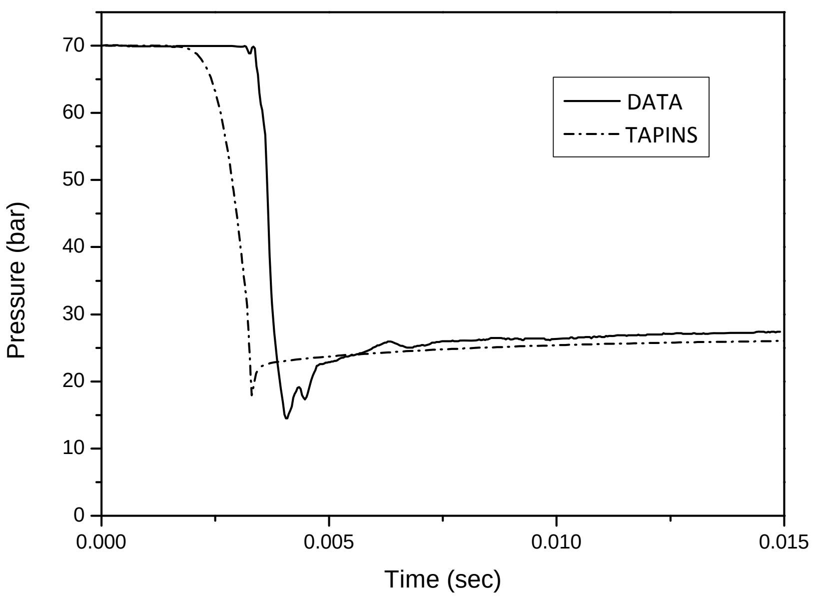

Figure 4.24 Edwards pipe short term pressure transient at gauge station 7

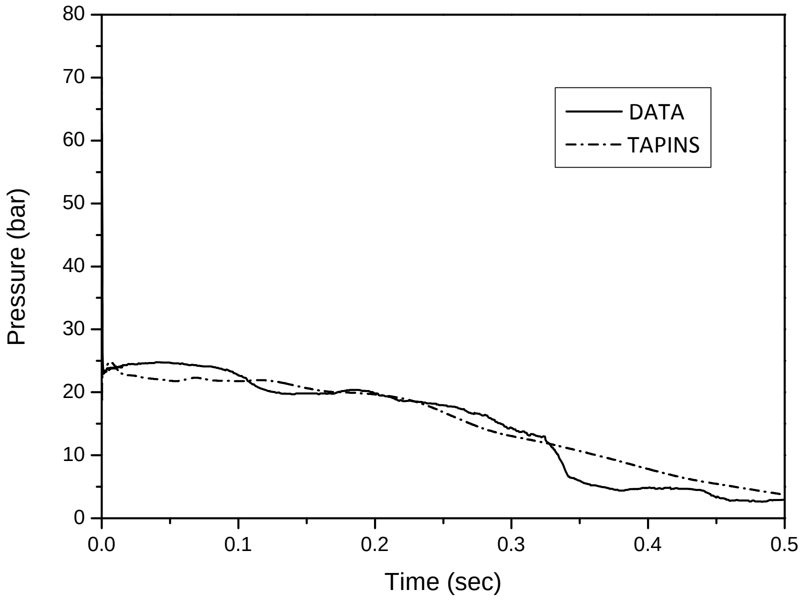

Figure 4.25 Edwards pipe long term pressure transient at gauge station 1

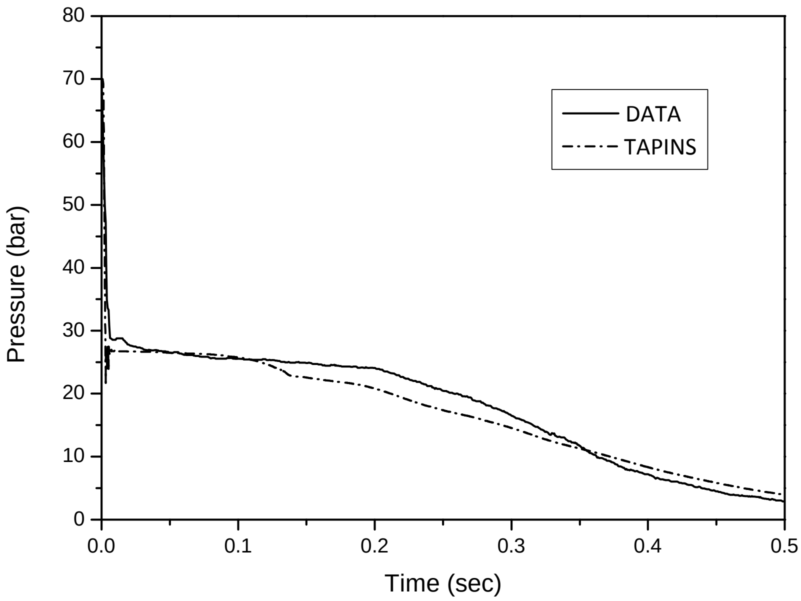

Figure 4.26 Edwards pipe long term pressure transient at gauge station 5

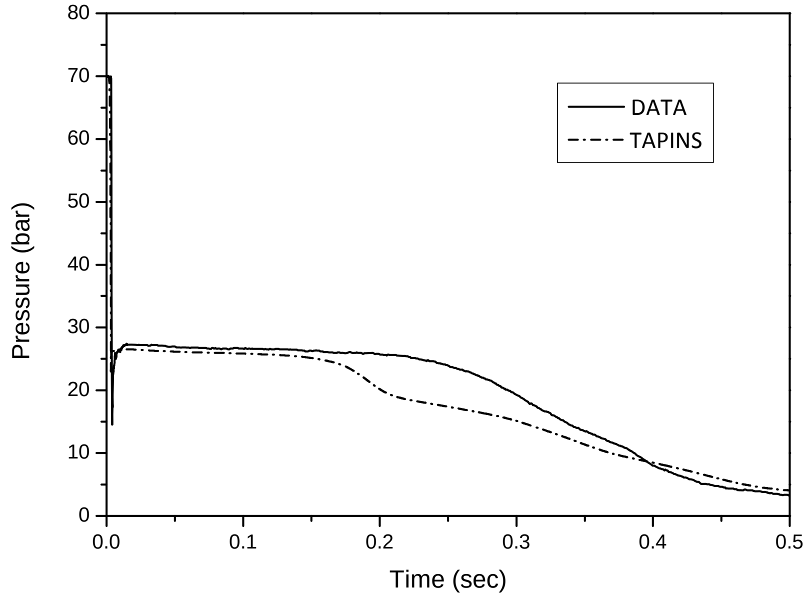

Figure 4.27 Edwards pipe long term pressure transient at gauge station 7

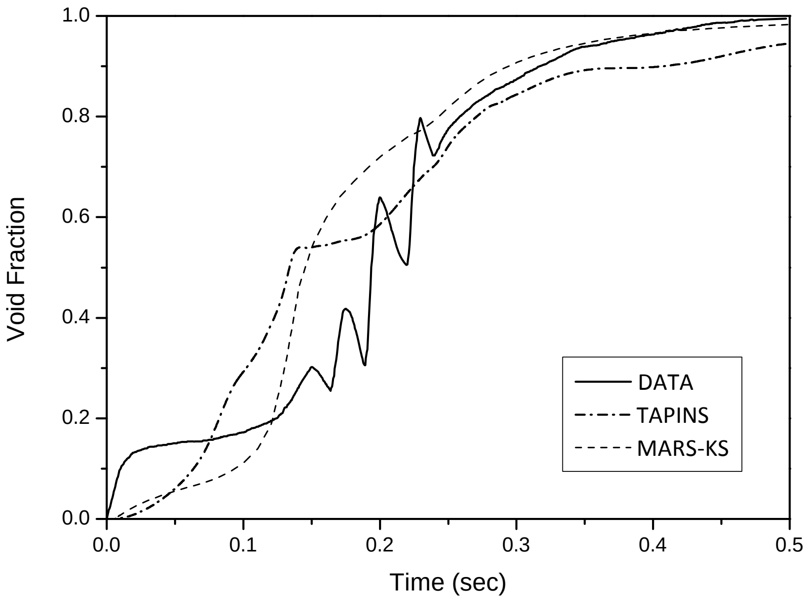

Figure 4.28 Edwards pipe long term void fraction at gauge station 5

Figure 4.29 REX-10 Test Facility (RTF)

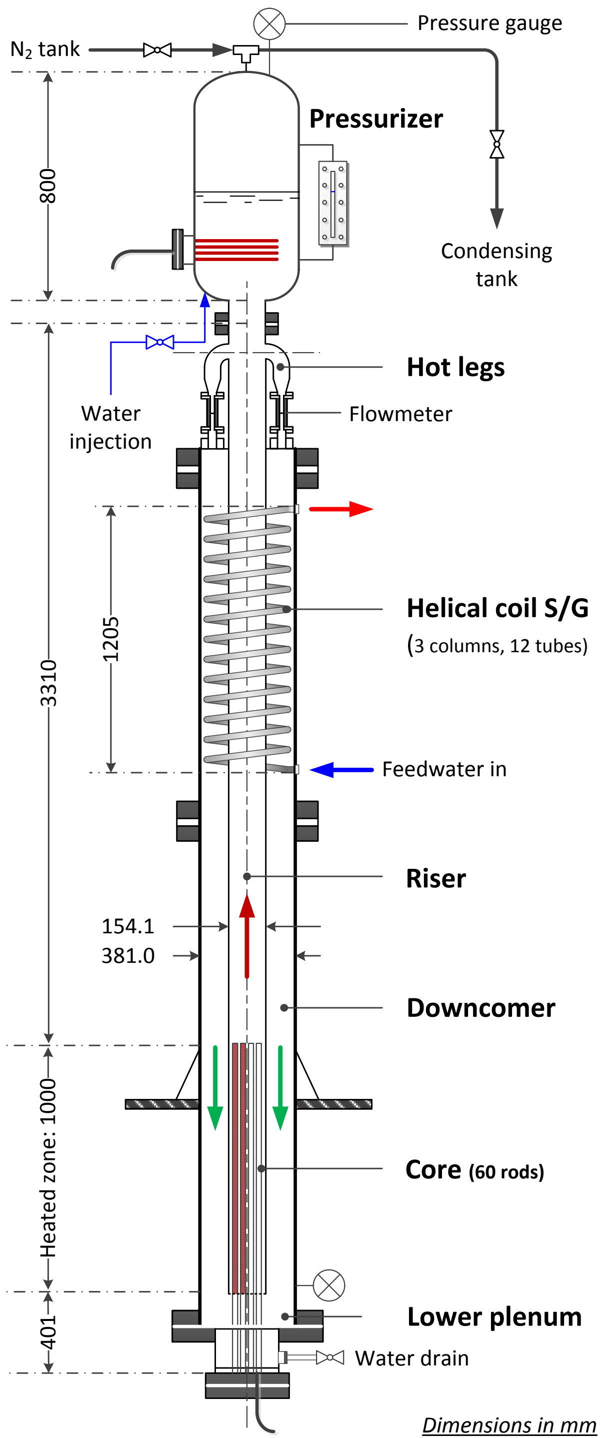

Figure 4.30 System configuration of the RTF

Figure 4.31 Steam-gas pressurizer vessel on the top of the RTF

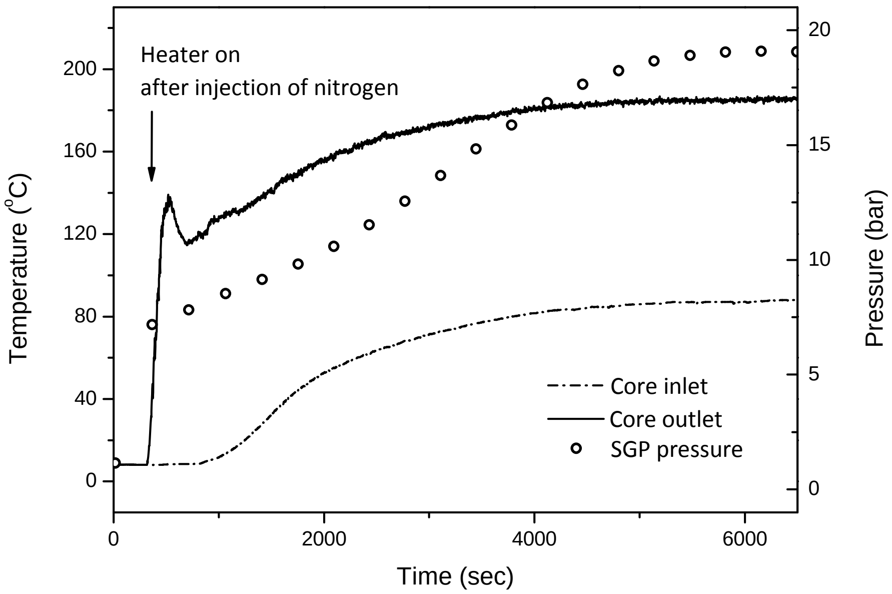

Figure 4.32 RTF approach to steady-state condition prior to initiating transients

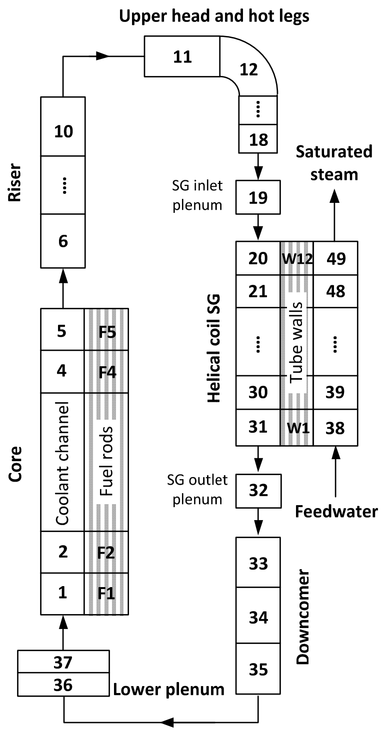

Figure 4.33 TAPINS nodalization diagram for RTF experiments

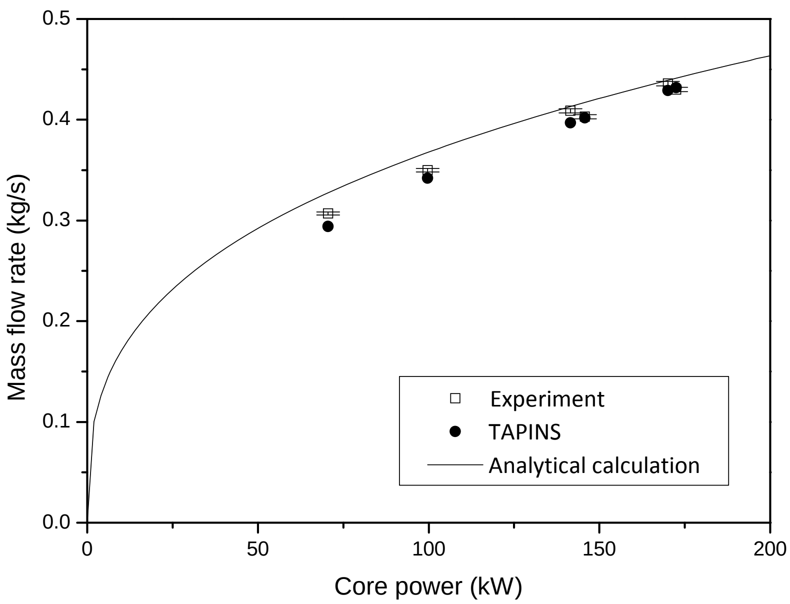

Figure 4.34 Steady-state natural circulation flow rate in the RTF

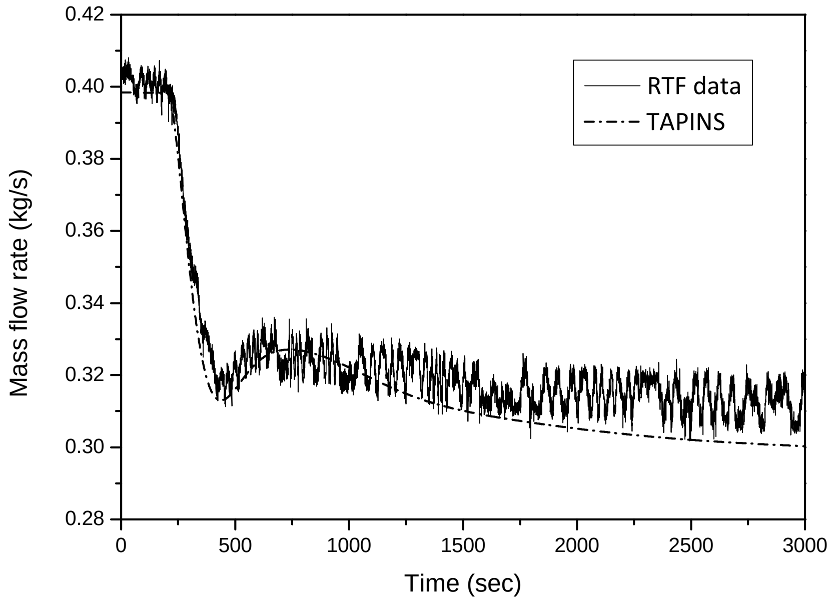

Figure 4.35 Coolant flow rate in response to a reduction in core power

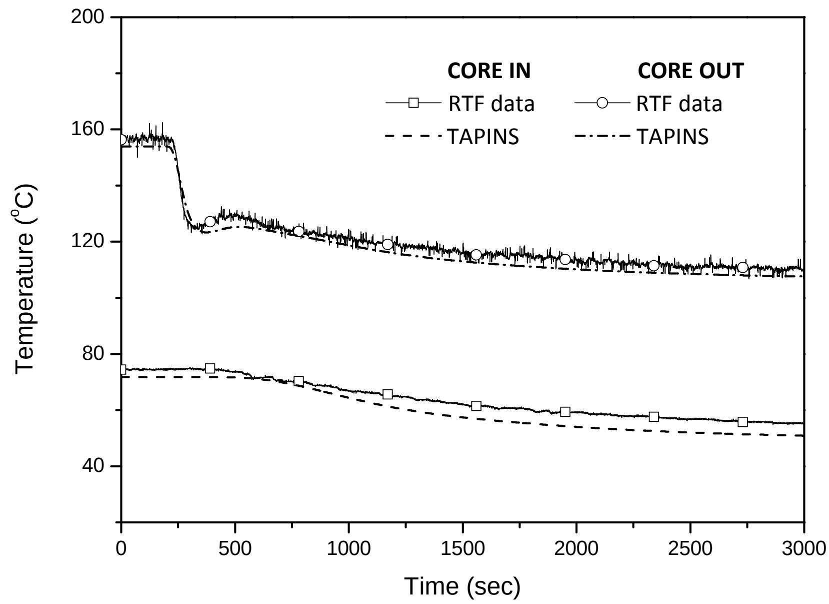

Figure 4.36 Coolant temperatures in response to a reduction in core power

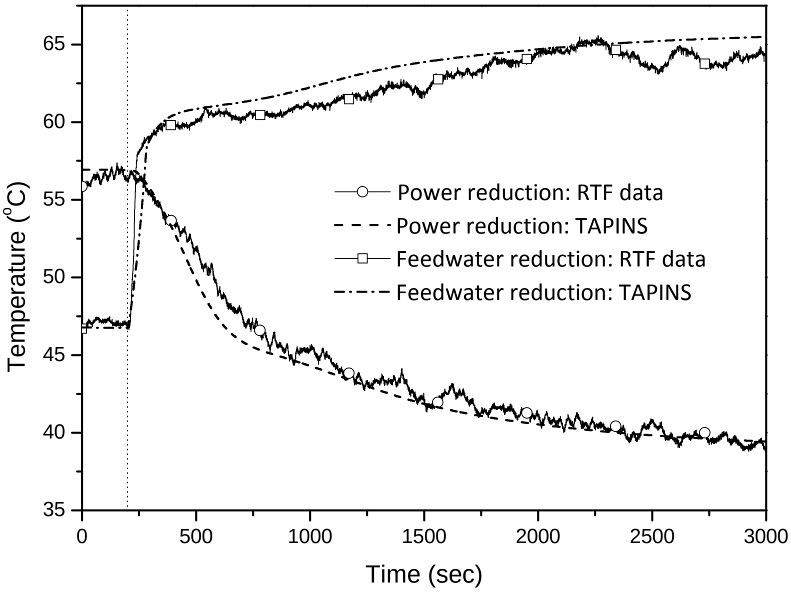

Figure 4.37 Variation in the outlet temperatures of feedwater

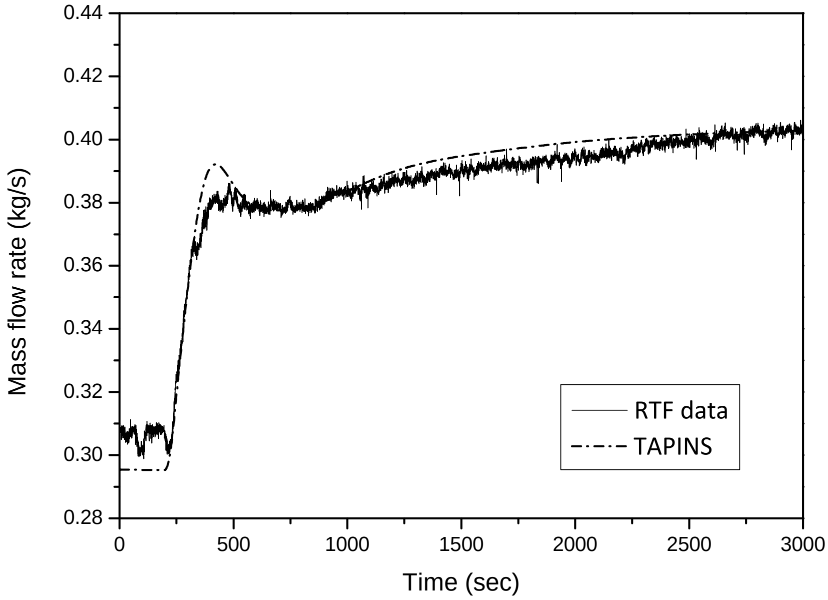

Figure 4.38 Coolant flow rate in response to an increase in core power

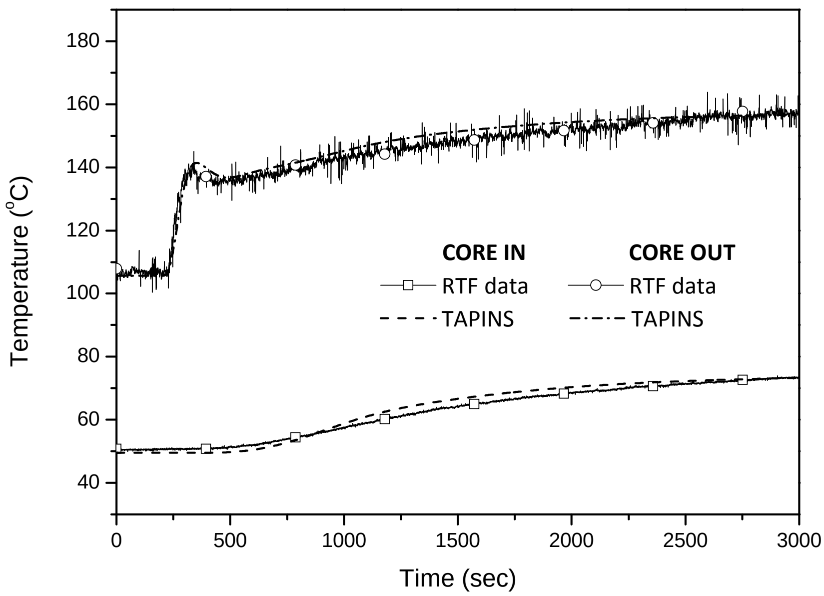

Figure 4.39 Coolant temperatures in response to an increase in core power

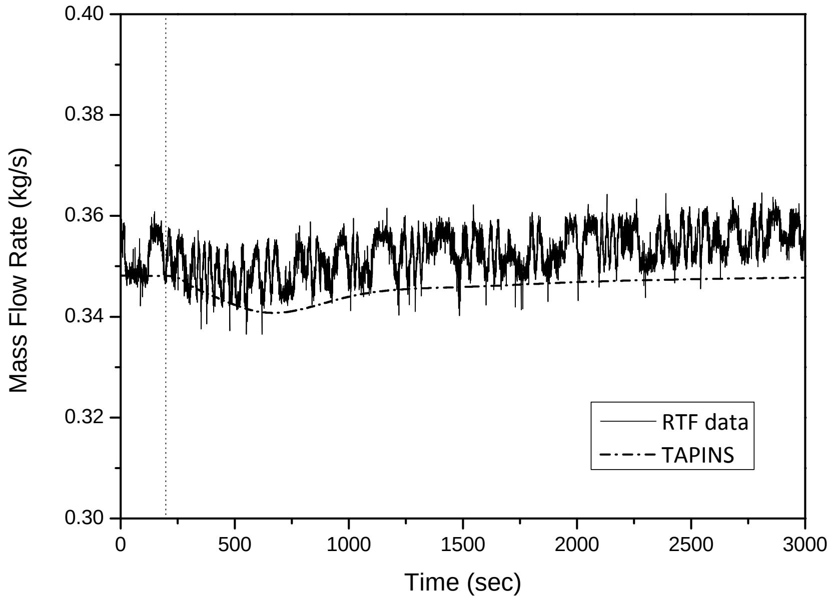

Figure 4.40 Coolant flow rate in response to a reduction in feedwater flow rate

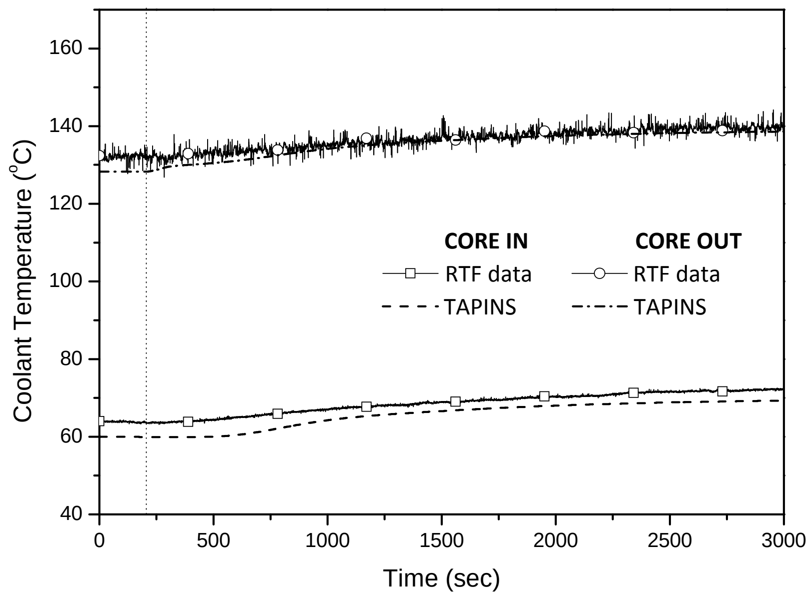

Figure 4.41 Coolant temperatures in response to a reduction in feedwater flow rate

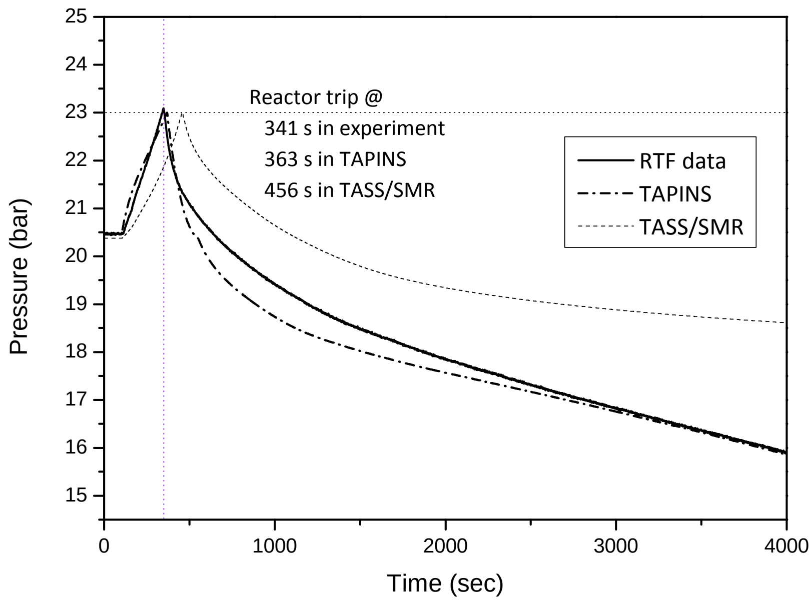

Figure 4.42 Pressurizer pressure in response to the LOFW accident

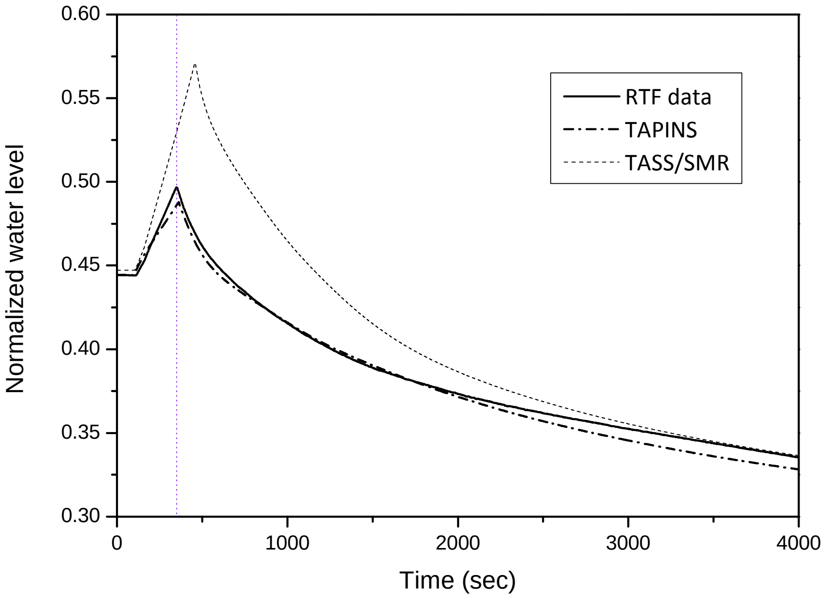

Figure 4.43 Water level of pressurizer in response to the LOFW accident

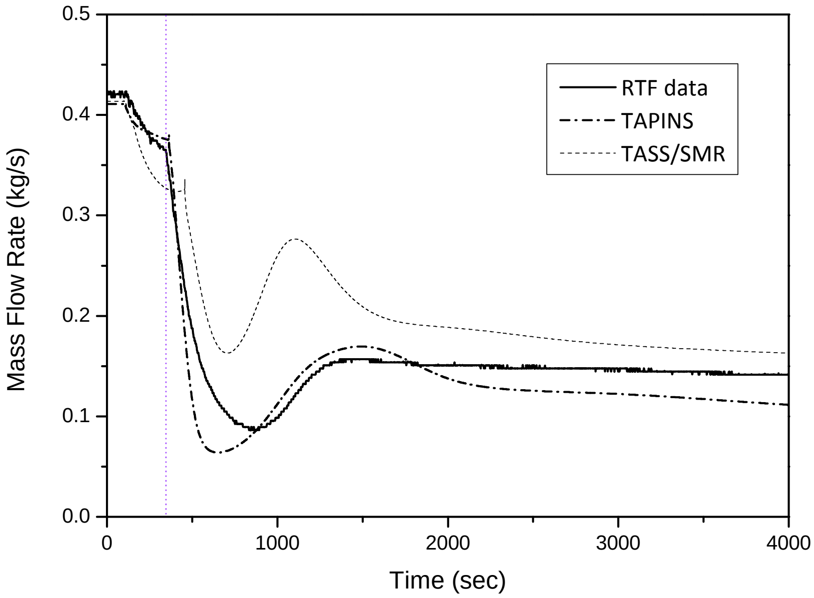

Figure 4.44 Coolant flow rate in response to the LOFW accident

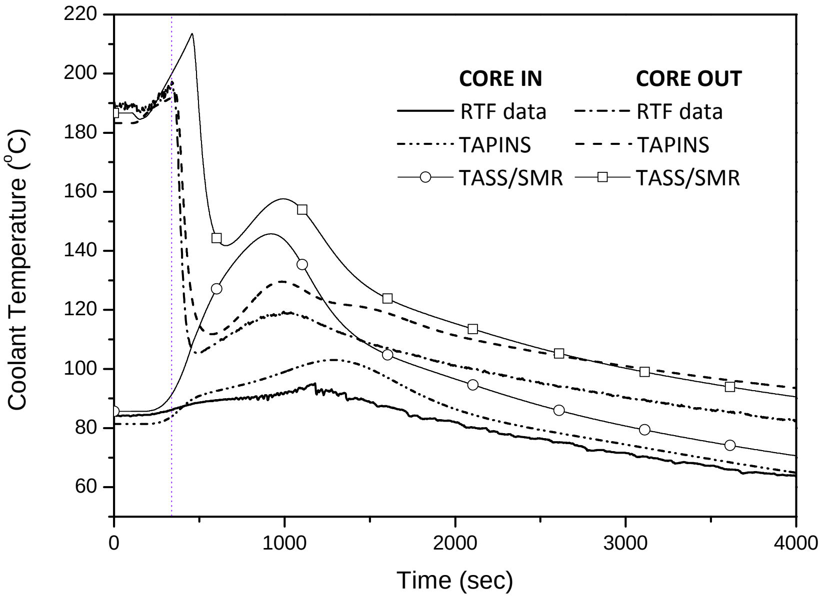

Figure 4.45 Coolant temperatures in response to the LOFW accident

Chapter 5

Selected Analyses for Reference Integral PWR

This chapter presents the computational analyses on the prototypical REX-10 to assess the design decisions and evaluate the thermal-hydraulic RCS responses under reactor transients using the TAPINS. The stabilized RCS variables are found through the steady-state calculation on the prototypical system to confirm the major design parameters of REX-10. In addition, two transient analyses are conducted for a reactivity insertion accident to simulate the behavior of core power level induced by arbitrary external reactivity, and an increase in feedwater flow event which results in a rise in the capability of the secondary system to remove the heat generated in the core. These simulations help to ascertain the system stability and the thermal-hydraulic behavior of REX-10 when encountered to a reactivity-induced accident and an inadvertent increase in heat removal leading to overpower.

The capability of the TAPINS is assessed by comparing the simulation results with the TASS/SMR predictions for these kinds of transients. While most of the hydrodynamic models incorporated into the TAPINS, including the steam-gas pressurizer model and the helical-coil steam generator model, have been basically validated in the previous chapter, the reactor kinetics model is not properly evaluated by this time. By carrying out the selected analyses on the power response to a reactivity transient for REX-10 and the effectuated time-dependent heat transfer to the coolant, in turn, by comparing the results with the predictions of the TASS/SMR, one can validate the point kinetics model and the core heat transport model of the TAPINS.

5.1 Identification of Design Parameters

5.1.1 REX-10 Models

Figure 5.1 illustrates the TAPINS nodalization diagram for REX-10. Basically the same noding is applied to the TASS/SMR model. The TAPINS system model consists of 48 control volumes that constitute the core, riser, upper head, S/G, downcomer, lower plenum and pressurizer. Note that the modeling of various piping needed for a conventional loop-type reactor is not necessary in the integral reactor system.

The core is axially divided into 10 nodes, among them 8 nodes for active heat transfer regions. This refined noding for core is prepared particularly for precise evaluation of the minimum DNBR (departure from nucleate boiling ratio). The cosine-shaped axial power profile is implemented, and the fuel rod is modeled using 8 radial meshes to solve heat conduction equations for the pellet, gap, and cladding. Each side of active helical-coil steam generator region consists of 10 nodes, and the total heat transfer area of tube bundles is set to 241.8 m^2. In both codes, the pressurizer is modeled by a single control volume.

5.1.2 Steady-state Results

The base case steady-state analysis is intended to assess the design basis of REX-10 and to implement the initial conditions for transient calculations. The resultant steady-state output parameters are listed in Table 5.1. As shown in Table 5.1, most of the system parameters predicted by the TAPINS conform to the design specifications very well. Moreover, other steady-state output variables from the TAPINS are in good agreement with the calculation results of the TASS/SMR. The stabilized coolant temperatures from the TAPINS are a little bit lower than those from the TASS/SMR, which indicates that the TAPINS slightly overestimates the heat transport through S/G tubes in establishing the heat balance equilibrium. The difference, however, seems acceptable. In the TAPINS, the core-averaged fuel temperature determined by the mean value of axial profile reduced by the weighting of 0.3 for center line temperatures and 0.7 for pellet surface temperatures, and it exhibits the deviation of 3.6 K from the calculation of the TASS/SMR.

One appreciable deviation is noted for the MDNBR. It is attributed to using different empirical correlations to calculate the critical heat flux in the TAPINS and the TASS/SMR. The TAPINS employs the correlation proposed by Bowring (1972) expressed in the form:

$$q''_{CHF} = \frac{A - Bh_{fg}x(z)/4}{C} \tag{5.1}$$

It is derived from the database covering the pressure range of 0.2 – 19 MPa, to which the operational pressure of REX-10 belongs. On the other hand, the TASS/SMR selects the maximum value between CHFs calculated by W-3 correlation and Macbeth correlation. Even though the W-3 correlation developed by Tong (1967) is the most widely used one for PWRs, it is not applicable to the system conditions of REX-10 since the correlation is valid for the pressure ranges of 6.9 – 15.9 MPa.

The steady-state results reveal that the design of REX-10 is suitable for achieving the prescribed RCS conditions, and the TAPINS can provide reasonable steady-state predictions for the prototypical integral reactor system.

5.2 Transient Simulations

5.2.1 Reactivity Insertion Accident

As the first transient analysis for REX-10, a hypothetical reactivity insertion event is simulated by the TAPINS and the TASS/SMR. This reactivity-induced accident may be caused by mechanisms such as uncontrolled withdrawal of control rods, rapid neutron poison removal, or changes in core component configurations (Lewis, 1977). Analyzed in this section is a mild reactivity transient when the external reactivity of 0.1 $ is inserted to the core in a stepwise way. Provided certain amount of reactivity is inserted by an advertent reason, a central question then becomes whether the core can returns to the critical state by the negative feedback effect of fuel and moderator without the occurrence of excessive temperature.

It is clarified that quantitative numerical values appearing in this section refers to the results of the TAPINS. In the reactor kinetics model, the following kinetics parameters are used for the core design of REX-10:

- Total delayed neutron fraction = 0.007242
- MTC = 60.2×10^{-5} / K
- FTC = 3.01×10^{-5} / K

Dependency of the MTC and the FTC on the temperature is not taken into account for simplicity. Figures 5.2 and 5.3 show the transient total reactivity and the normalized power in response to a reactivity insertion accident, respectively. Changes in the core-averaged fuel and coolant temperatures as well as the rate of heat transport to coolant are plotted in Figs. 5.4 and 5.5.

During the initial phase of the transient, the core power level begins to skyrocket to 114% as soon as the positive reactivity is inserted to the core. Instantaneously, the power approaches closely to the overpower trip setpoint of 11.5 MWth, but the reactor trip is not actuated. This overpower transient results in rapid increase of fuel and coolant temperatures; according to Fig. 5.4, the initial temperature rise of coolant is a bit above 1 K, but in a neutronic point of view, it induces a great deal of negative reactivity. Subsequently, the total reactivity is quickly reduced to null by the negative feedback effect arising from the rise in fuel and moderator temperatures.

The core returns to the criticality at 92.4 s after initiation of transient, followed by the gradual reduction of power level to the nominal value as the core stays in sub-critical state for a while. The mean fuel temperature is continuously decreased, but the coolant temperature is kept slightly higher than the initial value as long as the positive external reactivity is retained. The analysis results demonstrate that, when an overpower transient caused by reactivity insertion as much as 0.1 $ occurs, the system of REX-10 could adjust itself to a stable and safe state pursuant to the inherent feedback effect of the core.

Inspection of Figs. 5.2 – 5.5 reveals that the prediction of the TAPINS shows excellent agreement with the simulation results of the TASS/SMR. The maximum instantaneous deviation in the normalized core power is at most 1.5 %, and the transient histories, including the moment of the return-to-criticality, calculated from the TAPINS coincide well with those from the TASS/SMR. Code application to this case can provide a comprehensive insight for the capability of the TAPINS since all the component models, along with RCS model, incorporated in the TAPINS are synthetically applied to this simulation. From the comparison results, one can conclude the TAPINS provides quite reliable predictions on an reactivity-induced accident, and particularly, the point kinetics model and the core heat transport model are well coded in the TAPINS.

5.2.2 Decrease in Feedwater Flow Event

The other transient problem in this study is to describe the increased heat removal by the secondary system. The increase in feedwater flow event may be initiated by an inadvertent malfunction of the feedwater control system causing the excessive opening of control valve (Chung et al., 2008). Fig. 5.6 describes the mechanism how this heat removal transient affect the thermal-hydraulic behavior of the RCS. The increased heat transfer at S/G arising from the rise of feedwater flow causes a reduction in the coolant temperature in the primary circuit. This immediately leads to the increase of the power level by the negative feedback effect of the core, and depending on the core design and the thermal-hydraulic conditions of a reactor, the overpower trip may occur.

The assumed increase of feedwater flow rate by 20 % of normal value is simulated by the TAPINS and the TASS/SMR. The calculation results are plotted in Figs. 5.7 – 5.10. In this transient, the initial reactivity variation is determined by the competing effect between the Doppler and the moderator feedback mechanisms. As shown in Fig. 5.7, the reduction in the RCS coolant temperatures induces large positive reactivity, but it is observed a drastic rise of reactivity at the initial phase is suppressed for a while. It is because the feedback effect caused by an increase in the average fuel temperature opposes the power level change. In the situation, it is the relative magnitude of the Doppler and the moderator feedback mechanisms that becomes of primary importance.

The power level goes up to 109.7 % at 251s, followed by the recovery of the reactivity due to large negative feedback of the fuel. The core-averaged fuel temperature is maintained about 9 K over the initial value, the power stays high level as well. The increased power level drives greater natural circulation flow by 4 %, and the heat removal rate at the primary side of helical-coil S/G also rises as shown in Figs. 5.9 and 5.10.

The way of reflecting the changes in the feedwater flow rate is different for the TAPINS and the TASS/SMR. Unlike the TASS/SMR, the TAPINS does not solve the momentum equation for the secondary system. Instead, a representative flow rate is given by the table data. It results in the prompt rise of the flow rate at whole flow channel in the helical tubes in this case, and the time required for flow re-distribution is not taken into account. Notwithstanding this simplified handling of a feedwater transient, the results do not exhibit any significant deviation between the codes. It is confirmed from the comparisons that the prediction of the TAPINS on the heat removal transient by the secondary system is reasonable.

Table 5.1 Prediction results of design parameters and output variables for REX-10

Parameters	Design	TAPINS	TASS/SMR
Pressurizer pressure (MPa)	2.0	2.0	2.0
RCS flow rate (kg/s)	64.9	64.2	64.6
Core inlet temperature (^oC)	165.0	163.7	165.5
Core exit temperature (^oC)	200.0	199.0	200.5
Temperature rise across core (^oC)	35.0	35.3	35.1
Average fuel temperature (^oC)	-	294.6*	291.0
Minimum DNBR	-	24.6	20.0
Steam quality at the exit	-	0.9996	1.0
Total pressure drop in tube (kPa)	-	64.0	58.4

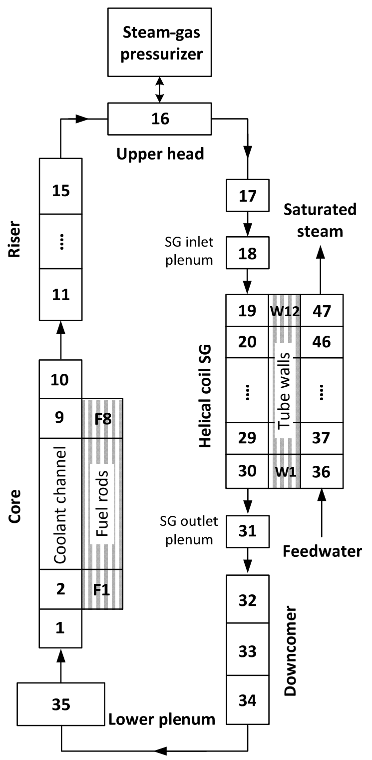

Figure 5.1 Nodalization diagram for REX-10

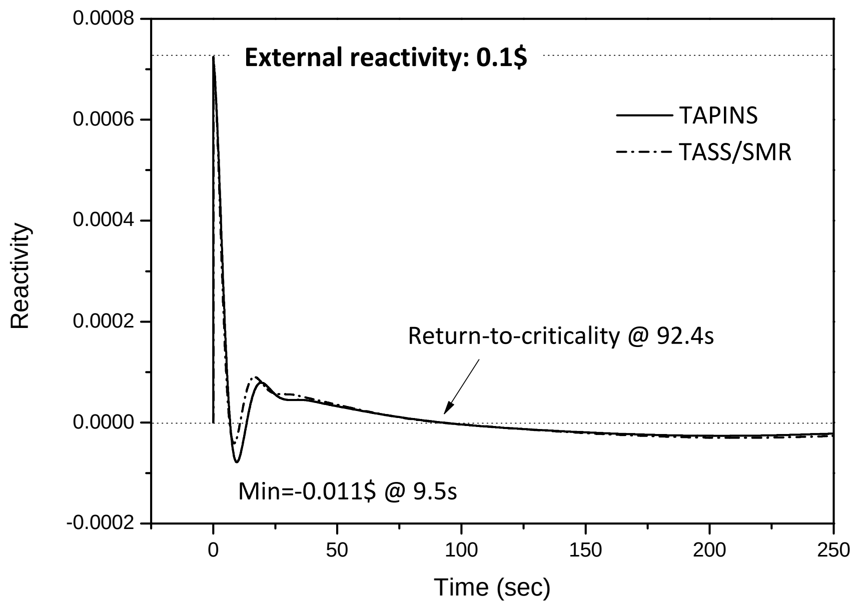

Figure 5.2 Total reactivity during a reactivity insertion accident

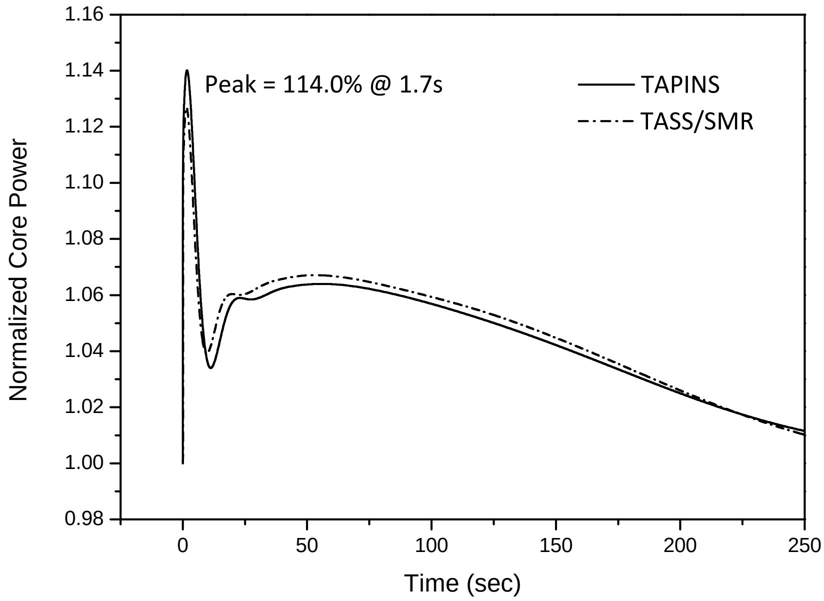

Figure 5.3 Normalized core power during a reactivity insertion accident

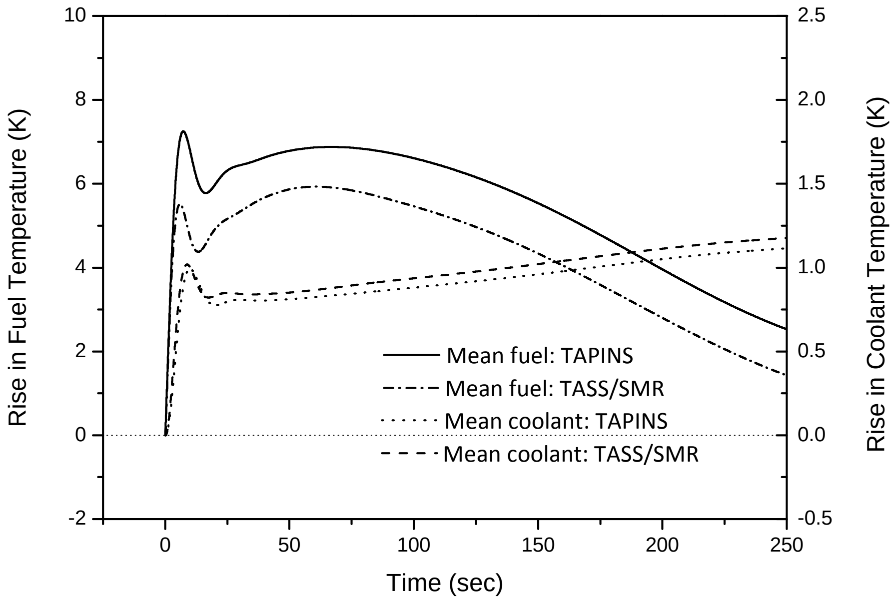

Figure 5.4 Changes in core average temperature of fuel and coolant during a reactivity insertion accident

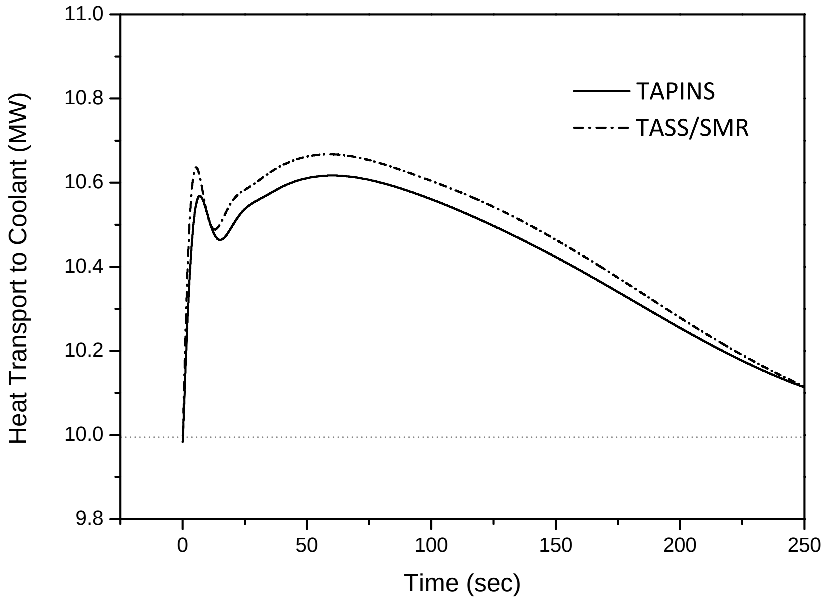

Figure 5.5 Heat transport to coolant during a reactivity insertion accident

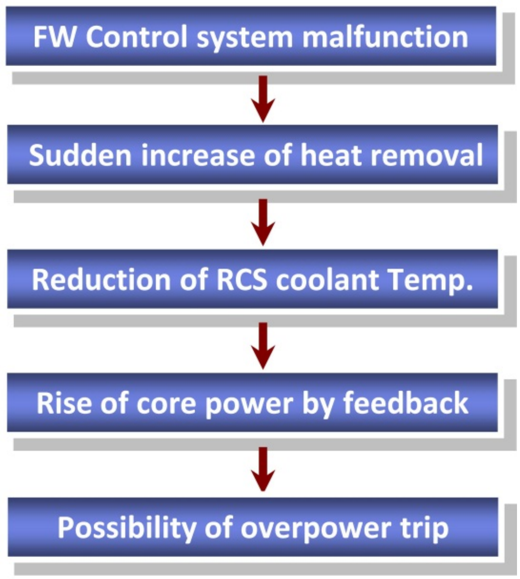

Figure 5.6 Mechanisms of overpower transient by an increase in feedwater flow

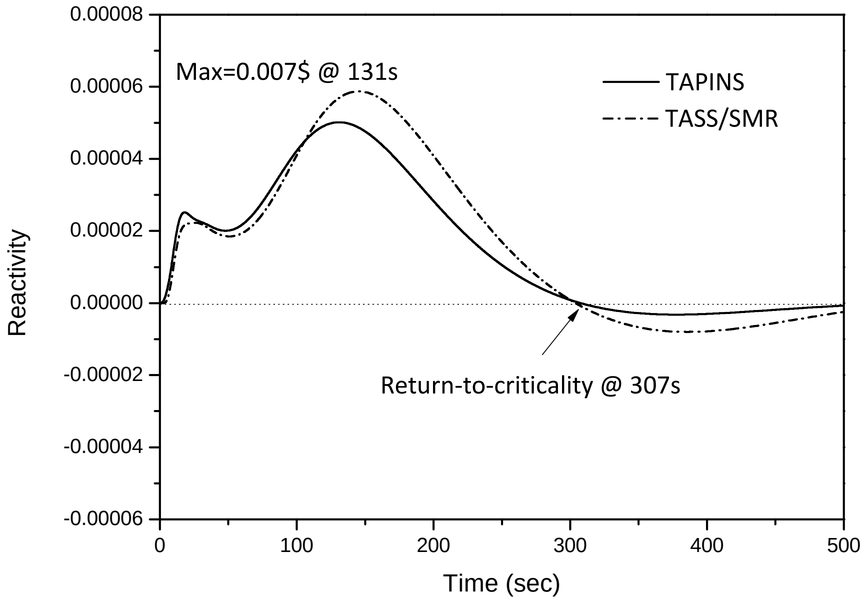

Figure 5.7 Total reactivity during an increase in feedwater flow event

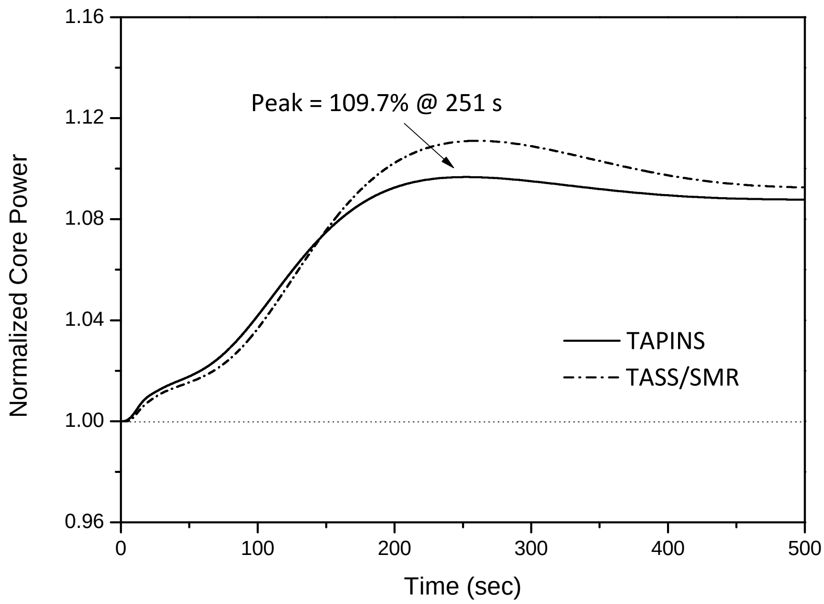

Figure 5.8 Normalized core power during an increase in feedwater flow event

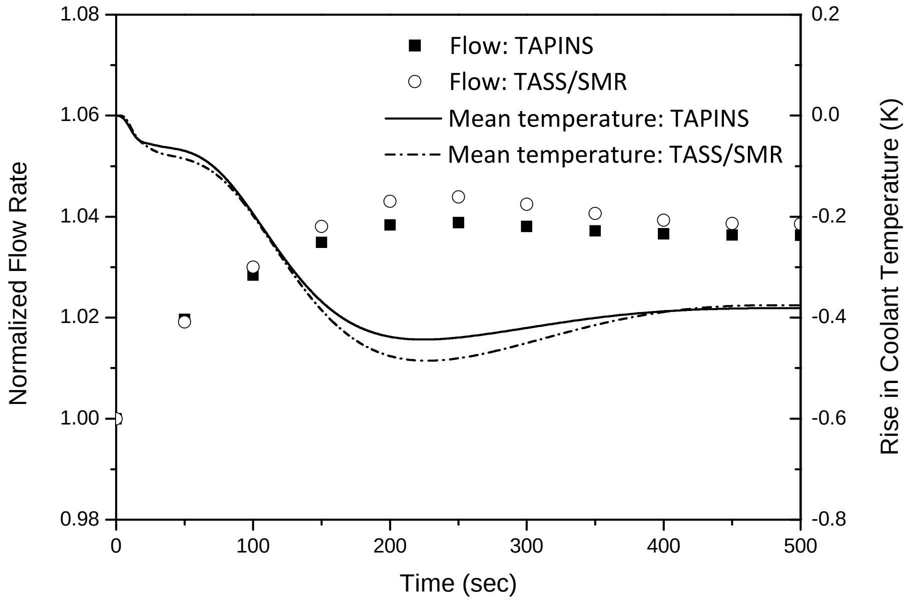

Figure 5.9 Normalized flow rate and the changes in core average temperature of coolant during an increase in feedwater flow event

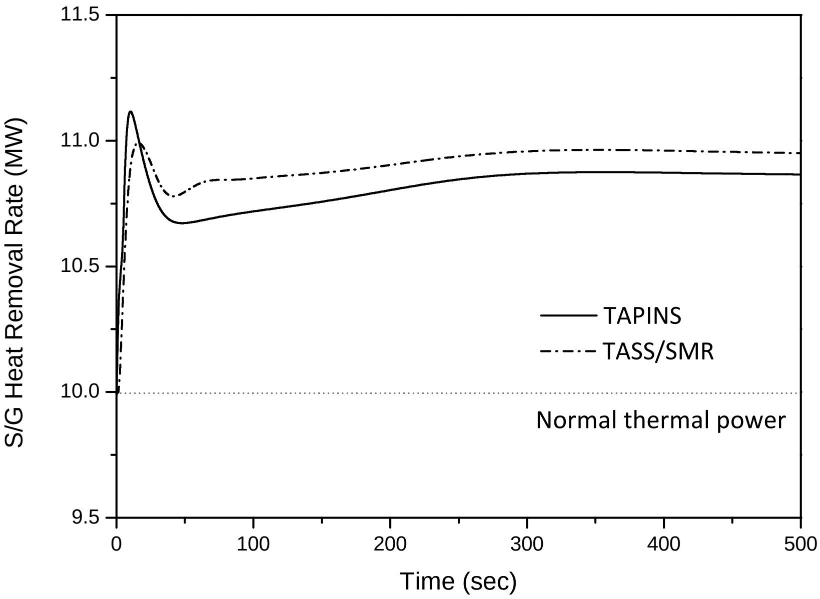

Figure 5.10 Heat removal rate of S/G during an increase in feedwater flow event

Chapter 6

Conclusions

6.1 Summary

In order to assess the design decisions and investigate the transient RCS responses of REX-10, a thermal-hydraulic system analysis code TAPINS has been developed in this study. The TAPINS was well verified and validated with 7 sets of assessment problems ranging from fundamental benchmarks to the integral effect tests performed in this study. The objective to demonstrate the code capability in predicting major thermal-hydraulic phenomena expected in DBAs of an integral reactor was accomplished.

The TAPINS was based on a one-dimensional four-equation drift-flux model as field equations to take into account the non-equilibrium effect of two-phase flow phenomena. It also consisted of component models for the core, the once-through helical-coil steam generator, and the built-in steam-gas pressurizer. In particular, a dynamic model of the steam-gas pressurizer to estimate the transient responses of the pressurizer containing the non-condensable gas was newly proposed. The three-region non-equilibrium model on the basis of the basic conservation equations of mass and energy as well as the constitutive relations for closure was established and incorporated into the TAPINS. In addition, the

TAPINS included the proper heat transfer coefficient correlations and the heat conduction model to predict the time-dependent heat transport in the core and the helical-coil S/G of a fully-passive integral PWR.

In the TAPINS, the hydrodynamic model was numerically solved using a semi-implicit finite difference scheme on the staggered grid meshes. The void fraction, pressure, mixture velocity and liquid enthalpy were selected as four primitive variables. The difference equations were solved by using the Newton Block Gauss Seidel (NBGS) method in which the fundamental unknowns were determined from 5×5 linear matrix for each mesh cell.

The TAPINS was verified and validated by carrying out various steady-state and transient analyses on the 7 assessment items. Through the calculation of the mass and energy conservation problem and the natural circulation problem, it was verified that the truncation error caused by the numerical solution scheme of the TAPINS was sufficiently small, and the calculated flow rate by natural circulation was in a high level of agreement with the analytical solutions. The TAPINS was validated against 4 sets of SETs on the MIT pressurizer tests, the subcooled boiling tests, the critical flow tests, and the Edwards pipe experiment. Moreover, a series of integral effect tests were conducted in the RTF to produce unique data of a fully-passive integral PWR utilized for code validation. The validation results demonstrated that the calculation results showed general agreement with the data, and thus, the TAPINS could provide a reasonable prediction on the performances and the transients of an integral PWR operating on natural circulation. Especially, the TAPINS could contribute to an improved prediction on the transient responses of the steam-gas pressurizer.

The TAPINS was applied to design assessment and transient simulations of the reference reactor and its results are compared to those of the TASS/SMR. The prediction indicated that the design of REX-10 was suitable for achieving the prescribed RCS conditions, and REX-10 can stay inherently safe due to a self-regulating effect by negative feedback when encountered to a reactivity-induced accident and an inadvertent increase in heat removal that lead to overpower transient.

6.2 Recommendations

Through the present study, the following further studies are suggested:

- For the practical applications to the small modular reactors that will be deployed in near future, the TAPINS has to be continuously improved to assure the reliable and robust simulations for a wide variety of transients and accidents in an integral PWR. In particular, the enhancement of code capability for the SBLOCA analysis is essentially required for the TAPINS. Then the added capability can be assessed with the SBLOCA experiment in the RTF, which is presented in Appendix B. The incorporation of GUI module for the TAPINS may help to improve user convenience.
- Passive safety systems such as the PRHRS play a crucial role in mitigating the consequence of DBAs in an SMR. The TAPINS needs to be equipped with the boiling and condensation heat transfer package applicable to simulate the safety performance of passive safety systems. The IET with an integral apparatus in conjunction with these passive safety systems are also suggested.

Nomenclature

A	Cross-sectional area (m^2), surface area (m^2)
A_s	Heat transfer area of structural wall
C_i	Neutron precursor concentration of group i (m^{-3})
C_0	Distribution parameter
C_p	Specific heat at constant pressure (J $kg^{-1}K^{-1}$)
d_o	Outer diameter of helical tube (m)
D	Diameter (m), diffusion coefficient ($m^2\ s^{-1}$)
D_h	Hydraulic diameter (m)
D_i	Inner diameter of annulus (m)
D_o	Outer diameter of annulus (m)
Eu	Euler number
f	Darcy friction factor, condensation coefficient
g	Gravitational acceleration (m s^{-2})
G	Mass flux (kg $m^{-2}s^{-1}$)
G_c	Critical mass flux (kg $m^{-2}s^{-1}$)
h	Specific enthalpy (J kg^{-1})
h_{cr}	Critical enthalpy (J kg^{-1})
h_{fg}	Latent heat (J kg^{-1})
H	Volumetric heat transfer coefficient (W $m^{-3}K^{-1}$)
j	Superficial velocity (m s^{-1})
k	Thermal conductivity (W $m^{-1}K^{-1}$)
K	Loss coefficient
L	Length (m)

M	Mass (kg), molecular weight (kg mol^{-1})
n	Polytropic exponent
N	Neutron density (m^{-3})
N_{col}	Number of columns in tube bundles
N_Z	Number of tube rows
Nu	Nusselt number
P	Pressure (Pa), total input power (W)
$\dot{P}$	Time derivative of pressure (Pa s^{-1})
Pr	Prandtl number
q''	Heat flux (W m^{-2})
R	Overall flow resistances (m^{-4}), universal gas constant (J mol^{-1}K^{-1})
Ra	Rayleigh number
s	Specific entropy (J kg^{-1}K^{-1})
Sh	Sherwood number
t	Time (s)
T	Temperature (^{o}C)
$\bar{T}$	Core-averaged temperature (^{o}C)
u	Velocity (m s^{-1})
u_b	Bubble terminal velocity (m s^{-1})
u_d	Liquid drop velocity (m s^{-1})
v	Velocity (m s^{-1})
V	Volume (m^3)
$\overline{V_{gj}}$	Drift velocity (m s^{-1})
w	Mass fraction
W	Mass flow rate (kg s^{-1})

x	Quality
z	Spatial coordinates (m)
$\bar{z}$	Elevation of midplane (m)

Greek Letters

α	Void fraction, heat transfer coefficient (W m^{-2}K^{-1})
α_T	Reactivity temperature coefficient (K^{-1}),
β	Total delayed neutron fraction
β_i	Delayed neutron fraction of group i
β_P	Volumetric expansion coefficient (K^{-1})
β_T	Isothermal compressibility (Pa^{-1})
γ	Isentropic exponent
Γ_g	Phase change rate (kg m^{-3}s^{-1})
Δh_{gf}	Enthalpy difference between phases (J kg^{-1})
$\Delta\rho$	Density difference between phases (kg m^{-3})
ε	Surface roughness (m), pumping term, fractional error
Λ	Neutron generation time (s)
λ_i	Decay constant of precursor group i (s^{-1})
μ	Viscosity (Pa s)
ρ	Density (kg m^{-3})
$\bar{\rho}$	Core-averaged density of coolant (kg m^{-3})
σ	Surface tension (J m^{-2})

υ Specific volume ($m^3\ kg^{-1}$)

ξ_h Heated perimeter (m)

Subscripts

annu	Annulus between core barrel and reactor pressure vessel
b	Bulk properties
CHF	Critical heat flux
e	Expected
E	Equilibrium
ext	Externally introduced
f	Fuel, saturated liquid
g	Saturated vapor, gaseous mixture in pressurizer
i	Delayed neutron precursor group, interface, noding index
if	Bulk interface for liquid
ig	Bulk interface for vapor
in	Insertion of non-condensable gas into pressurizer
j	Junction index for minor loss
l1	Lower liquid region of pressurizer
l2	Upper liquid region of pressurizer
l12	Between lower and upper liquid regions
m	Mixture, moderator
max	Maximum
min	Minimum
nc	Non-condensable gas

NC	Natural circulation
r	Relative difference between phases
rv	Relief of gaseous mixture
s	Structural wall, saturated state
sgp	Steam-gas pressurizer
stm	Steam
t	Throat
w	Wall
v	Vapor phase
0	Initial values, stagnation properties
∞	Free stream condition

Superscripts

k	Iteration step
n	Time level index
s	Saturation property

References

Aksan, S., D'Auria, F., and Staedtke H., "User effects on the thermal-hydraulic transient system code calculations," *Nuclear Engineering and Design*, vol. 145, pp. 159-174, 1993.

American Society of Mechanical Engineers, “Rules for Construction of Nuclear Power Plant Components” ASME Boilers and Pressure Vessel Code: An American National Standard, Section III, American Society of Mechanical Engineers, New York, 1986

Baek, S. M. and No, H. C., "A nonequilibrium three-region model for transient analysis of pressurized water reactor pressurizer," *Nuclear Technology*, vol. 74, pp. 260-266, 1986.

Baron, R., "Digital model simulation of a nuclear pressurizer," *Nuclear Science and Engineering*, vol. 52, pp. 283-291, 1973.

Bartolomey, G. and Chanturiya, V., "Experimental study of true void fraction when boiling subcooled water in vertical tubes," *Thermal Engineering*, vol. 14, pp. 123-128, 1967.

Bowring, R. W., "A simple but accurate round tube uniform heat flux, dryout correlation over the pressure range 0.7–17 MN/m^2," AEEW-R789, 1972.

Bridgman, P. W., *The Thermodynamics of electrical phenomena in metals, and condensed collection of thermodynamic formulas*, Dover Publications, New York, 1961.

Carlson, K. E., Ransom, V. H., and Wagner, R. J., “The application of RELAP5 to a pipe blowdown experiment,” *Proceedings of the ANS/ASME/NRC International Topical Meeting on Nuclear Reactor Thermal Hydraulics*, New York, USA, 1980

Chen, J. C., "Correlation for boiling heat transfer to saturated fluids in convective flow," *Industrial & Engineering Chemistry Process Design and Development*, vol. 5, pp. 322-329, 1966.

Chexal, B., Lellouche, G., Horowitz, J., and Healzer, J., "A void fraction correlation for generalized applications," *Progress in Nuclear Energy*, vol. 27, pp. 255-295, 1992.

Choi, K. Y. et al., "Parametric studies on thermal hydraulic characteristics for transient operations of an integral type reactor," *Nuclear Engineering and Technology*, vol. 38, pp. 185-194, 2006.

Christensen, H., "Power-to-void transfer functions," ANL-6385, Argonne National Laboratory, 1961.

Chung, Y. J., Jun, I. S., Kim, S. H., Yang, S. H., Kim, H. R. and Lee, W. J., "Development and assessment of system analysis code, TASS/SMR for integral reactor, SMART," *Nuclear Engineering and Design*, vol. 244, pp. 52-60, 2012.

Chung, Y. J., Lee, S. W., Kim, S. H., and Kim, K. K., "Passive cooldown performance of a 65MW integral reactor," *Nuclear Engineering and Design*, vol. 238, pp. 1681-1689, 2008.

Churchill, S. W. and Chu, H. H. S., "Correlating equations for laminar and turbulent free convection from a horizontal cylinder," *International Journal of Heat and Mass Transfer*, vol. 18, pp. 1049-1053, 1975a.

Churchill, S. W. and Chu, H. H. S., "Correlating equations for laminar and turbulent free convection from a vertical plate," *International Journal of Heat and Mass Transfer*, vol. 18, pp. 1323-1329, 1975b.

Edwards, A. R. and O'brien, T. P., "Studies of phenomena connected with the depressurization of water reactors," *Journal of the British Nuclear Energy Society*, vol. 9, pp. 125-135, 1970.

Emonot, P., Souyri, A., Gandrille, J., and Barré, F., "CATHARE-3: A new system code for thermal-hydraulics in the context of the NEPTUNE project," *Nuclear Engineering and Design*, vol. 241, pp. 4476-4481, 2011.

Finkelstein, Y. and Tamir, A., "Interfacial heat transfer coefficients of various vapors in direct contact condensation," *The Chemical Engineering Journal*, vol. 12, pp. 199-209, 1976.

Henry, R. E. and Fauske, H. K., "The two-phase critical flow of one-component mixtures in nozzles, orifices, and short tubes," *Journal of Heat Transfer*, vol. 93, pp. 179-187, 1971.

Hibiki, T. and Ishii, M., "One-dimensional drift-flux model and constitutive equations for relative motion between phases in various two-phase flow regimes," *International Journal of Heat and Mass Transfer*, vol. 46, pp. 4935-4948, 2003.

Hirt, C. W. and Romeo, N. C., “Application of a drift-flux model to flashing in straight pipes,” LA-6005-MS, Los Alamos Scientific Laboratory, 1975.

IAEA, "Integral design concepts of advanced water cooled reactors," IAEA-TECDOC-977, 1995.

IAEA, "Status of small and medium sized reactor designs," September 2011.

Ishii, M. and Hibiki, T., *Thermo-fluid dynamics of two-phase flow*, Springer, New York, 2010.

Jang, B. I., Kim, M. H., and Jeun, G. D., "Transient analysis of natural circulation nuclear reactor REX-10," *Journal of Nuclear Science and Technology*, vol. 48, pp. 1046-1056, 2011.

Jeong, J. J. and No, H. C., "An improved numerical scheme with the fully-implicit two-fluid model for a fast-running system code," *Nuclear Engineering and Design*, vol. 104, pp. 145-153, 1987.

Kim, J. W., Lee, Y. G., Ahn, H. K., and Park, G. C., "Condensation heat transfer characteristic in the presence of noncondensable gas on natural convection at high pressure," *Nuclear Engineering and Design*, vol. 239, pp. 688-698, 2009.

Kim, J. W., "Condensation heat transfer with noncondensable gas at high pressure for designing steam-gas pressurizer," Ph. D thesis, Seoul National University, 2010.

Kim, T. W., Kim, J. W., and Park, G. C., "Development of nonequilibrium pressurizer model with noncondensable gas," *Nuclear Engineering and Design*, vol. 236, pp. 375-384, 2006.

Kocamustafaogullari, G. and Ishii, M., "Scaling of two-phase flow transients using reduced pressure system and simulant fluid," *Nuclear Engineering and Design*, vol. 104, pp. 121-132, 1987.

Kozeki, M., Nariai, H., Furukawa, T., and Kurosu, K., "A study of helically-coiled tube once-through steam generator," *Bulletin of JSME*, vol. 13, pp. 1485-1494, 1970.

Lahey, R. T., "A mechanistic subcooled boiling model," *Proceedings of 6th International Heat Transfer Conference*, vol. 1, pp. 293-297, 1978.

Lahey, R. T. and Moody, F. J., *The thermal-hydraulics of a boiling water nuclear reactor,* American Nuclear Society, La Grange Park, Illinois, 1993

Lee, Y. G., Kim, J. W., and Park, G. C., "Experimental study on wall condensation with noncondensables in steam-gas pressurizer," *Proceedings of the 13th International Topical Meeting on Nuclear Reactor Thermal Hydraulics (NURETH-13)*, Kanazawa city, Japan, 2009

Lee, Y. G., Kim, J. W., and Park, G. C., "Development of a thermal–hydraulic system code, TAPINS, for 10MW regional energy reactor," *Nuclear Engineering and Design*, vol. 249, pp. 364-378, 2012.

Lee, Y. G. and Park, G. C., “Experimental investigation on SBLOCA and LOFW of 10 MW regional energy reactor in a scaled-down IET facility,” *Proceedings of* *the 9th International Topical Meeting on Nuclear Thermal-Hydraulics, Operation and Safety (NUTHOS-9)*, Kaohsiung, Taiwan, 2012.

Leonard, M. T., "The effects of a non-condensable gas on pressurizer insurge transients," Master Thesis, Massachusetts Institute of Technology, 1983.

Lewis, E. E., *Nuclear power reactor safety*, John Wiley & Sons, New York, 1977.

Liles, D. and Reed, W. H., "A semi-implicit method for two-phase fluid dynamics," *Journal of Computational Physics*, vol. 26, pp. 390-407, 1978.

Lim, S. W., "Modeling and verification of safety system for small-sized passive reactor," Master thesis, Seoul National University, 2010.

Marek, R. and Straub, J., "Analysis of the evaporation coefficient and the condensation coefficient of water," *International Journal of Heat and Mass Transfer*, vol. 44, pp. 39-53, 2001.

Mori, Y. and Nakayama, W., "Study of forced convective heat transfer in curved pipes (2nd report, turbulent region)," *International Journal of Heat and Mass Transfer*, vol. 10, pp. 37-59, 1967.

OECD/NEA, "Current status, technical feasibility and economics of small nuclear reactors," June 2011.

Paulsen, M. P. et al., "RETRAN-3D – A program for transient thermal-hydraulic analysis of complex fluid flow systems, Volume 1: theory and numerics," NP-7450, EPRI, 1998.

Petruzzi, A. and D'Auria, F., "Thermal-hydraulic system codes in nuclear reactor safety and qualification procedures," *Science and Technology of Nuclear Installations*, pp. 1-16, 2008.

PROPATH GROUP, "PROPATH: a program package for thermophysical properties of fluids, Ver. 12.1," 2001.

Ransom, V. H. et al., "RELAP5/MOD3.3 code manual Volume I: code structure, system models, and solution methods," NUREG/CR-5535/Rev 1, Idaho National Engineering Laboratory, 2001a.

Ransom, V. H. et al., "RELAP5/MOD3.3 code manual Volume III: developmental assessment problems," NUREG/CR-5535/Rev 1, Idaho National Engineering Laboratory, 2001b.

Ransom, V. H. et al., "RELAP5/MOD3.3 code manual Volume IV: models and correlations," NUREG/CR-5535/Rev 1, Idaho National Engineering Laboratory, 2001c.

Reyes, J. N. et al., "Testing of the multi-application small light water reactor (MASLWR) passive safety systems," *Nuclear Engineering and Design*, vol. 237, pp. 1999-2005, 2007.

Saha, P. and Zuber, N., "Point of net vapor generation and vapor void fraction in subcooled boiling," *Proceedings of 5th International Heat Transfer Conference*, vol. 4, pp. 175-179, 1974.

Schrage, R. W., *A theoretical study of interphase mass transfer*, Columbia

University Press, New York, 1953.

Todreas, N. E. and Kazimi, M. S., *Nuclear systems*, Hemisphere Pub. Corp., New York, 1990.

Tong, L., "Heat transfer in water-cooled nuclear reactors," *Nuclear Engineering and Design*, vol. 6, pp. 301-324, 1967.

Wulff, W., "Computer simulation of two-phase flow in nuclear reactors," *Nuclear Engineering and Design*, vol. 141, pp. 303-313, 1993.

Yoon, J. H., Kim, J. P., Kim, H. Y., Lee, D. J., and Chang, M. H., "Development of a computer code, ONCESG, for the thermal-hydraulic design of a once-through steam generator," *Journal of Nuclear Science and Technology*, vol. 37, pp. 445-454, 2000.

Zigrang, D. and Sylvester, N., "A review of explicit friction factor equations," *Journal of Energy Resources Technology*, vol. 107, pp. 280-283, 1985.

Zukauskas, A. and Ulinskas, R., "Banks of plain and finned tubes," Heat Exchanger Design Handbook, GF Hewitt Edition, Begell House, Inc., New York, pp. 2.2.4.1-2.2.4.17, 1998.

Zukauskas, A. and Ulinskas, R., "Efficiency parameters for heat transfer in tube banks," *Heat Transfer Engineering*, vol. 6, pp. 19-25, 1985.

Zvirin, Y., "A review of natural circulation loops in pressurized water reactors and other systems," *Nuclear Engineering and Design*, vol. 67, pp. 203-225, 1982.

Appendix A

Elements of Linear System for NBGS Method

The elements of a 5 × 5 linear system for the NBGS iteration to obtain the primitive variables of field equations are represented below. This matrix system is commonly applied to all mesh cells.

$$\begin{bmatrix} X & 0 & X & & & & & & \\ & \ddots & & & & & & & \\ X & 0 & A_{i11} & 0 & A_{i13} & 0 & 0 & & \\ & & A_{i21} & A_{i22} & A_{i23} & A_{i24} & A_{i25} & & \\ & & A_{i31} & A_{i32} & A_{i33} & A_{i34} & A_{i35} & & \\ & & A_{i41} & A_{i42} & A_{i43} & A_{i44} & A_{i45} & & \\ & & 0 & 0 & A_{i53} & 0 & A_{i55} & 0 & X \\ & & & & & & & \ddots & \\ & & & & X & X & & X & X \end{bmatrix} \begin{bmatrix} v_1 \\ \vdots \\ v_{i-1/2} \\ \delta\alpha_i \\ \delta P_i \\ \delta h_i \\ v_{i+1/2} \\ \vdots \\ \delta h_N \end{bmatrix} = \begin{bmatrix} \vdots \\ b_{i1} \\ b_{i2} \\ b_{i3} \\ b_{i4} \\ b_{i5} \\ \vdots \end{bmatrix}$$

Mixture momentum equation (the left cell)

$$A_{i11} = (\rho_m)^n_{i-1/2} \frac{\Delta z_{i-1/2}}{\Delta t}$$

$$A_{i13} = 1$$

$$\begin{aligned} b_{i1} = {} & (\rho_m)^n_{i-1/2} \Delta z_{i-1/2} \frac{(v_m)^n_{i-1/2}}{\Delta t} - (\rho_m)^n_{i-1/2} (v_m)^n_{i-1/2} \left[(v_m)^n_i - (v_m)^n_{i-1} \right] \\ & - \left\{ \left[\frac{\alpha\rho_v\rho_l}{(1-\alpha)\rho_m} \overline{V_{gj}}^2 \right]^n_i - \left[\frac{\alpha\rho_v\rho_l}{(1-\alpha)\rho_m} \overline{V_{gj}}^2 \right]^n_{i-1} \right\} - \left(P^k_i - P^{k+1}_{i-1} \right) - (\rho_m)^n_{i-1/2} g_z \Delta H_{z,i-1/2} \\ & - \frac{1}{2} \left(f_m \frac{L}{D} + K \right)_{i-1/2} (\rho_m)^n_{i-1/2} (v_m)^n_{i-1/2} \left| (v_m)^n_{i-1/2} \right| \end{aligned}$$

Mixture continuity equation

$$A_{i21} = -\frac{\Delta t}{V_i}(\rho_m)_{i-1/2}^n A_{i-1/2}$$

$$A_{i22} = (\rho_v)_i^k - (\rho_l)_i^k$$

$$A_{i23} = (1-\alpha_i^k)\frac{\partial \rho_l^k}{\partial P} + \alpha_i^k \frac{\partial (\rho_v^s)^k}{\partial P}$$

$$A_{i24} = (1-\alpha_i^k)\frac{\partial \rho_l^k}{\partial h_l}$$

$$A_{i25} = \frac{\Delta t}{V_i}(\rho_m)_{i+1/2}^n A_{i+1/2}$$

$$b_{i2} = (\rho_m)_i^n - (\rho_m)_i^k$$

Vapor mass conservation equation

$$A_{i31} = -\frac{\Delta t}{V_i}(\alpha\rho_v)_{i-1/2}^n A_{i-1/2}$$

$$A_{i32} = (\rho_v)_i^k$$

$$A_{i33} = \alpha_i^k \frac{\partial (\rho_v^s)^k}{\partial P} + \frac{H_{if}^n \cdot \Delta t}{(h_v^*)_i^n - (h_l^*)_i^n} \cdot \left(\frac{\partial (T^s)^k}{\partial P} - \frac{\partial T_l^k}{\partial P} \right)$$

$$A_{i34} = -\frac{H_{if}^n \cdot \Delta t}{(h_v^*)_i^n - (h_l^*)_i^n} \cdot \frac{\partial T_l^k}{\partial h_l}$$

$$A_{i35} = \frac{\Delta t}{V_i}(\alpha\rho_v)_{i+1/2}^n A_{i+1/2}$$

$$b_{i3} = \alpha_i^n (\rho_v)_i^n - \alpha_i^k (\rho_v)_i^k - \frac{\Delta t}{V_i}\left\{ \left[\frac{\alpha\rho_v\rho_l \overline{V_{gj}} A}{\rho_m} \right]_{i+1/2}^n - \left[\frac{\alpha\rho_v\rho_l \overline{V_{gj}} A}{\rho_m} \right]_{i-1/2}^n \right\}$$
$$- \frac{H_{if}^n \cdot \Delta t}{(h_v^*)_i^n - (h_l^*)_i^n}\left[(T^s)_i^k - (T_l)_i^k \right] + \Delta t \cdot \Gamma_w^n$$

Mixture enthalpy-energy equation

$$A_{i41} = -\frac{\Delta t}{V_i}(\rho_m h_m)_{i-1/2}^n A_{i-1/2}$$

$$A_{i42} = (\rho_v h_v)_i^k - (\rho_l h_l)_i^k$$

$$A_{i43} = (1-\alpha_i^k)\cdot(h_l)_i^k \frac{\partial \rho_l^k}{\partial h_l} + \alpha_i^k (h_v)_i^k \frac{\partial (\rho_v^s)^k}{\partial P} + \alpha_i^k (\rho_v)_i^k \frac{\partial (h_v^s)^k}{\partial P}$$

$$-\frac{\Delta t}{\Delta z_i}\left[v_m + \frac{\alpha(\rho_l - \rho_v)}{\rho_m}\overline{V_{gj}}\right]_i^n - 1$$

$$A_{i44} = (1-\alpha_i^k)\left[(\rho_l)_i^k + (h_l)_i^k \frac{\partial \rho_l^k}{\partial h_l}\right]$$

$$A_{i45} = \frac{\Delta t}{V_i}(\rho_m h_m)_{i+1/2}^n A_{i+1/2}$$

$$b_{i4} = (\rho_m h_m)_i^n - (\rho_m h_m)_i^k - \frac{\Delta t}{V_i}\left\{\left[\frac{\alpha \rho_v \rho_l}{\rho_m}\Delta h_{gf}\overline{V_{gj}}A\right]_{i+1/2}^n - \left[\frac{\alpha \rho_v \rho_l}{\rho_m}\Delta h_{gf}\overline{V_{gj}}A\right]_{i-1/2}^n\right\}$$

$$+\Delta t \cdot \left(\frac{q_W'' \xi_h}{A}\right) + (P_i^k - P_i^n) + \frac{\Delta t}{\Delta z_i}\left[v_m + \frac{\alpha(\rho_l - \rho_v)}{\rho_m}\overline{V_{gj}}\right]_i^n \left(P_i^k - P_{i-1}^{k+1}\right)$$

Mixture momentum equation (the right cell)

$$A_{i53} = -1$$

$$A_{i55} = (\rho_m)_{i+1/2}^n \frac{\Delta z_{i+1/2}}{\Delta t}$$

$$b_{i5} = (\rho_m)_{i+1/2}^n \Delta z_{i+1/2} \frac{(v_m)_{i+1/2}^n}{\Delta t} - (\rho_m)_{i+1/2}^n (v_m)_{i+1/2}^n \left[(v_m)_{i+1}^n - (v_m)_i^n\right]$$

$$-\left\{\left[\frac{\alpha \rho_v \rho_l}{(1-\alpha)\rho_m}\overline{V_{gj}}^2\right]_{i+1}^n - \left[\frac{\alpha \rho_v \rho_l}{(1-\alpha)\rho_m}\overline{V_{gj}}^2\right]_i^n\right\} - \left(P_{i+1}^k - P_i^k\right) - (\rho_m)_{i+1/2}^n g_z \Delta H_{z,i+1/2}$$

$$-\frac{1}{2}\left(f_m \frac{L}{D} + K\right)_{i+1/2} (\rho_m)_{i+1/2}^n (v_m)_{i+1/2}^n \left|(v_m)_{i+1/2}^n\right|$$

Appendix B

SBLOCA Experiment in RTF

This section presents the experimental investigation on the RTF SBLOCA induced by a 1/4 inch diameter break in the nitrogen injection line to the steam-gas pressurizer. The integral layout of REX-10 can eliminates the large-break LOCA in virtue of the absence of large diameter pipelines. However, one of the most severe accidents may be initiated by the rupture at the nitrogen injection line through which the gaseous mixture is immensely discharged in the event. Even though the SBLOCA experiment is not simulated by the TAPINS, it is believed that the outputs from this IET will be the priceless, unique data to understand the transient response of REX-10 during the postulated accident and to validate a thermal-hydraulic system code in the future.

The SBLOCA experiment begins with the opening of a valve located at the midway between the pressurizer and the condensing tank, which simulates the rupture of a small-diameter pipe. When the pressurizer pressure of the RTF reaches 1.7 MPa, the reactor trip is to occur. From then on, the experimental procedure is identical to that of the LOFW test. A central question then would become whether the reactor can be brought to the cold shutdown state without core uncovery. Thus one has to focus on the variation of the water level in the steam-gas pressurizer, which is a direct indication of RCS coolant inventory, by the discharge of fluid out of RPV. Figures A.1 – A.6 show the transient thermal-hydraulic parameters during the SBLOCA experiment.

The pressurizer pressure falls down to the trip setpoint in 8.1s after opening the vent valve. Then the heater power is reduced to 12.5 kW instantaneously, and the feedwater flow rate is also adjusted to a prescribed value to simulate actuation of PRHRS. Depressurization of the RTF induces radical internal flashing. Initially, the gaseous mixture of steam and N_2 quickly comes out of the pressurizer vessel, but as time passes, only the steam produced by flashing is discharged through the break.

Even though the reactor shutdown is followed by rapid drop in the core exit temperature, the coolant in the annular space above S/G region gets saturated for a while as shown in Fig. A.3. The saturation state lasts until 1700s and then the transition to single-phase (subcooled) flow occurs by the continuous cooldown of PRHRS. At this moment, the heat transport to S/G is increased in a sudden; coolant temperatures both at core exit and at S/G inlet quickly goes down in an instant while the feedwater exit temperature rises. On the contrary, the liquid in the pressurizer is saturated for the entire period of the accident. Figure A.4 shows that, by the thermal stratification, the hot liquid layer floats at the top regardless of the cooldown of the coolant in the primary circuit.

By a simulated PRHRS flow, the coolant temperatures in the RTF continue to decrease. At about 4400 s, the RTF system is brought to cold shutdown eventually. With regard to the mass flow rate, the measurement by a turbine flowmeter may be incorrect for the two-phase flow. It is confirmed, however, that the natural circulation flow rate is stabilized to ~0.15 kg/s after transition to the subcooled state when the single-phase heat transfer is established again.

One can infer from the test results that REX-10 may readily assure sufficient inventory of coolant under SBLOCA condition if a proper safety injection system is incorporated. Since just gaseous mixture is discharged in the accident, the reduction in the RCS water level is quite moderate. When the RTF reaches the cold shutdown, the pressurizer vessel is still filled with some amount of water. It indicates that the system is brought to cold shutdown before the water level goes down below the elevation of entrances to hot legs and the flow path of liquid coolant is cut off.

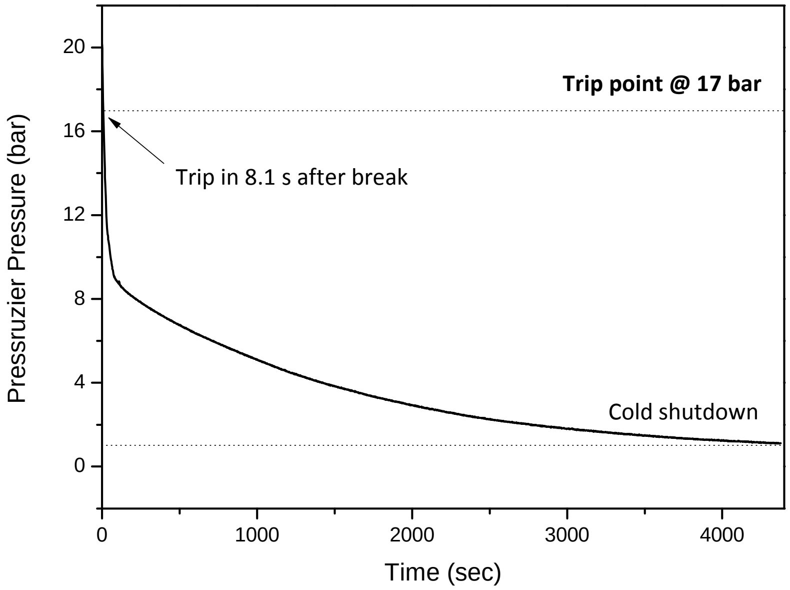

Figure A.1 Pressurizer pressure during the SBLOCA

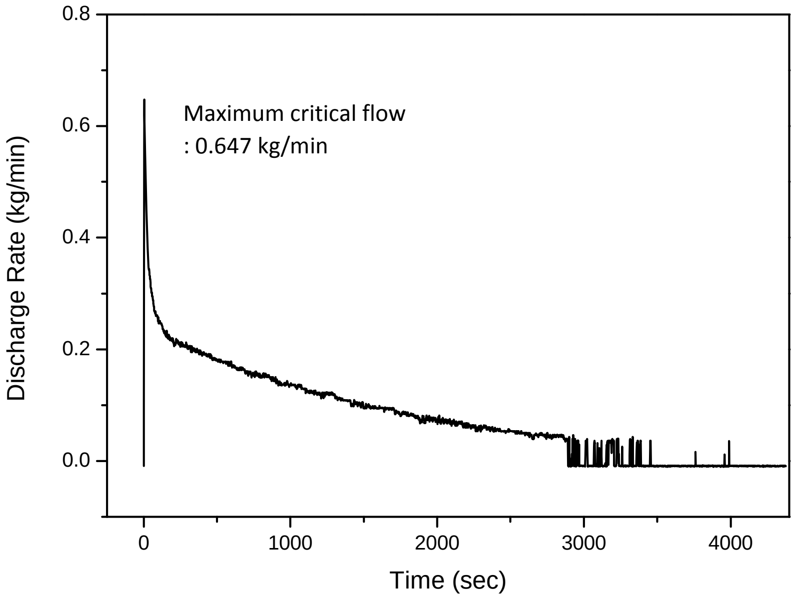

Figure A.2 Break flow during the SBLOCA

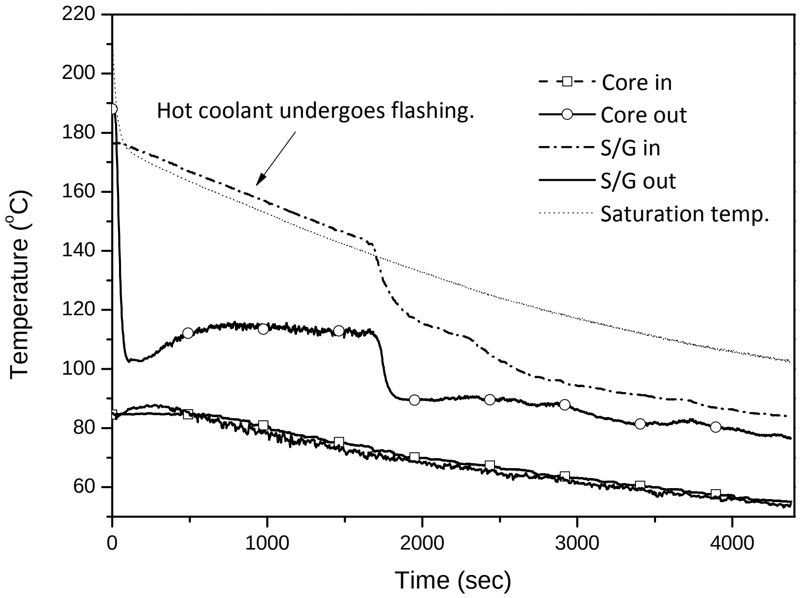

Figure A.3 Coolant temperatures during the SBLOCA

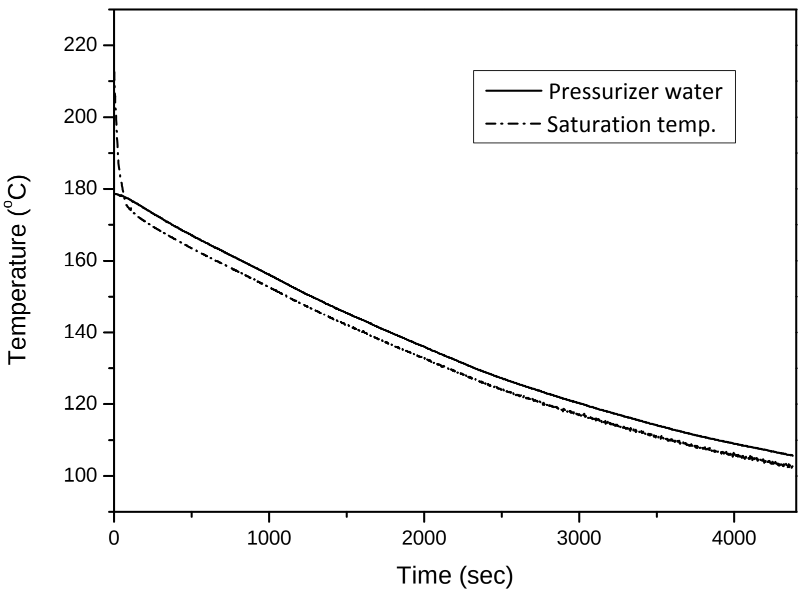

Figure A.4 Liquid temperature of pressurizer during the SBLOCA

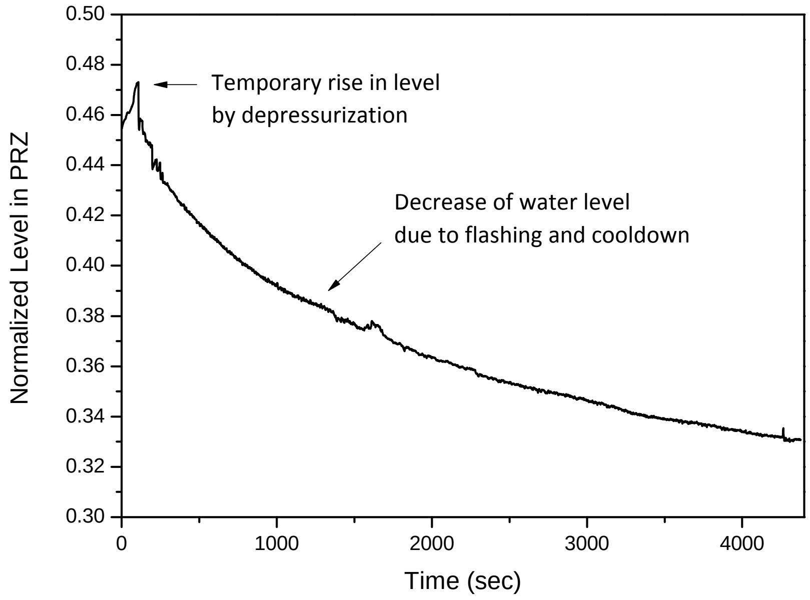

Figure A.5 Pressurizer water level during the SBLOCA

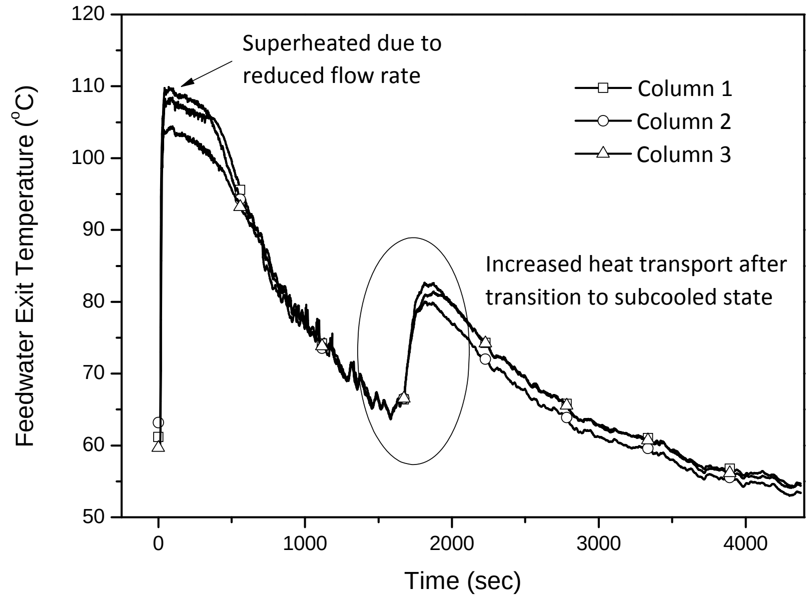

Figure A.6 Feedwater Exit Temperature during the SBLOCA

Appendix C

Supplement on LOFW Analysis of TASS/SMR

In the TASS/SMR application to the RTF LOFW accident presented in section 4.3.5, the calculation results showed considerable deviation from the data due to the prediction of the delayed core trip than measured. The analysis was originally intended to evaluate the code capability in simulating the transient pressurization in the absence of heat removal from S/G. In the practical analyses on the LOFW accident, however, the critical focus should be whether a system code is able to provide the accurate prediction on “the transient after reactor trip” during the LOFW event. Therefore, the recalculation results of the TASS/SMR on the LOFW transient from the moment of core trip are supplemented in this appendix.

In this supplementary analysis, the TASS/SMR starts to run by implementing the initial conditions same as the experimental data at the instant of overpressure trip. That is, the measured coolant temperatures in the RTF, the liquid temperature and water level in the pressurizer were used as the initial conditions for transient calculation. It was assumed that the inside of helical tube was initially filled with the saturated steam, and the heat slab model of the TASS/SMR was applied to take into account the heat loss from the structure. The calculation results of the TASS/SMR for the LOFW accident after core trip are plotted in Figs. A.7 – A.10.

The results reveal that the TASS/SMR predicts the slower decrease in the system pressure than the data at an initial transient, but the rate of decline gets relatively faster as time passes. Keeping the deviation from data lower than 1 bar, the TASS/SMR successfully predicts the long-term pressure transient after reactor trip. A notable observation is found in the analysis result without calculating the heat loss to surroundings. Unless the heat slab model for the pressurizer vessel is applied, the predicted reduction of the pressurizer pressure is much slower than the data. It indicates that, in the simulation of the TASS/SMR, the modeling of heat loss from the structural wall has a great influence in calculating the pressure transient of the steam-gas pressurizer caused by the changes in the water level or the coolant temperatures.

The calculation results of the TASS/SMR on the pressurizer water level and the mass flow rate in the RTF are generally consistent with the data. In addition, the predicted coolant temperatures show good agreement with the experimental values as shown in Fig. A.10. From the above results, it is confirmed that the TASS/SMR predicts well the transient response of REX-10 during the LOFW accident after reactor trip.

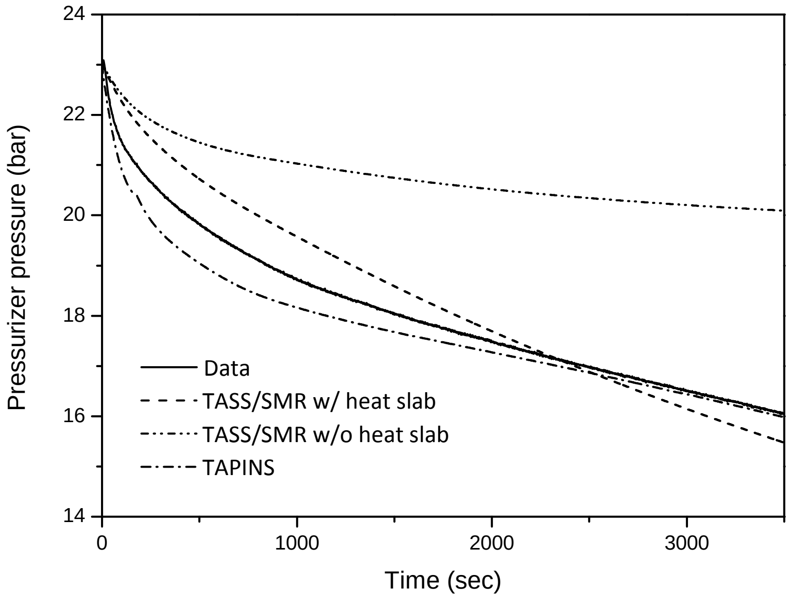

Figure A.7 Pressurizer pressure by TASS/SMR after reactor trip

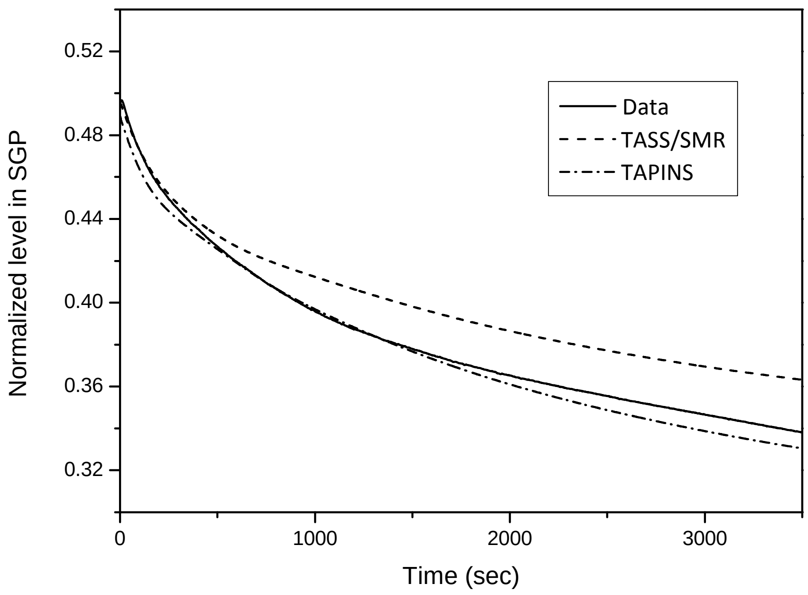

Figure A.8 Water level of pressurizer by TASS/SMR after reactor trip

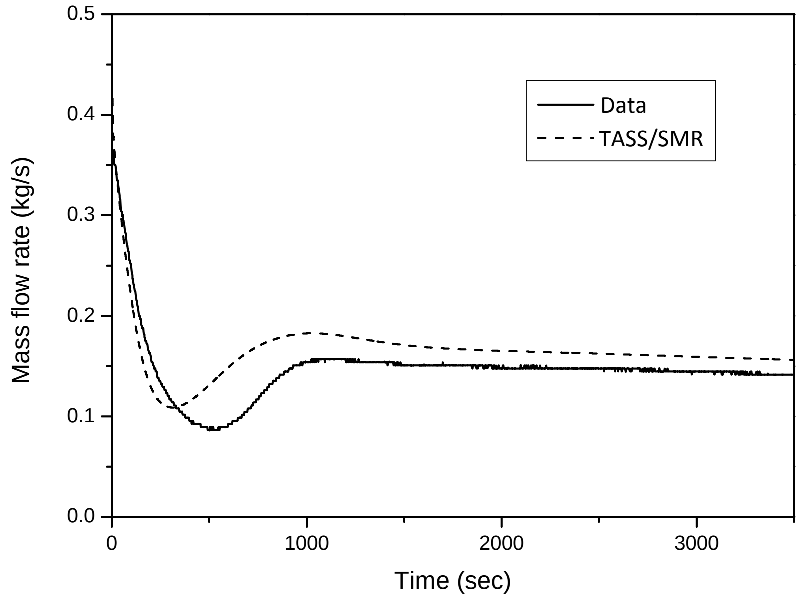

Figure A.9 Coolant flow rate by TASS/SMR after reactor trip

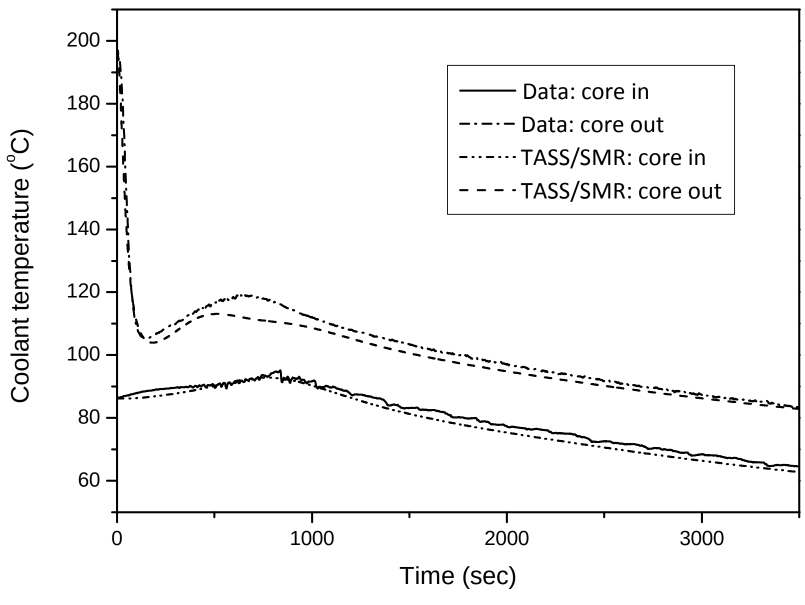

Figure A.10 Coolant temperatures by TASS/SMR after reactor trip

국문 초록

REX-10은 소규모의 전력 생산과 지역난방을 위해 개발된 소형의 일체형 가압경수로이다. 이는 펌프 없이 자연대류에 의해 노심을 냉각하고, 증기-가스 가압기를 통해 냉각재 계통의 압력을 유지하며, 피동잔열제거계통이 작동하여 노심정지 시 붕괴열을 제거하는 완전피동 일체형 원자로이다. 본 연구에서는 REX-10의 설계를 검증하고 과도 거동을 분석하기 위한 열수력 시스템 코드 TAPINS를 개발하였다. 다양한 벤치마크 문제들과 실험들과의 비교를 통해 TAPINS의 검증을 수행하였으며, 특히 REX-10의 축소규모 장치에서 종합효과실험을 수행하여 생산된 데이터를 코드 검증에 활용하였다.

TAPINS는 원자로냉각재계통, 노심, 나선형 증기발생기, 증기-가스 가압기의 모델을 갖추고 있다. TAPINS의 지배방정식으로는 이상 유동의 비평형 효과를 고려할 수 있는 four-equation drift-flux 모델을 채택하였다. 특히, 비응축성 가스를 포함하고 있는 증기-가스 가압기의 동적 모델을 본 연구에서 개발하여 이를 TAPINS에 탑재하였다. TAPINS는 또한 완전피동 가압경수로 내의 열전달을 예측하기 위한 각종 열전달 상관식과 열전도 모델을 포함하고 있다. 지배방정식은 비정렬 격자 기반의 반음해법을 적용하여 차분화하였으며 NBGS 해법을 통해 기본변수들의 해를 구하였다.

TAPINS의 확인 및 검증을 위해 다양한 정상상태 및 과도상태 해석을 수행하였다. 질량 및 에너지 보존과 자연대류에 대한 기본 검증문제에 TAPINS를 적용하였으며, 가압기 insurge 과도, 미포화 비등, 임계 유동, 파이프 블로다운 등 개별효과실험과의 비교를 통해 TAPINS의 해석능을 검증하였다. 코드 검증을 위한 종합효과실험 데이터를 생산하기 위해 REX-10의 1/50 축소 실험장치인 RTF를 구축하여 정상상태 자연대류, 노심출력 과도, 완전급수상

실사고 등에 대한 실험을 수행하였고, 이를 TAPINS의 해석결과와 비교하였다. 이와 더불어, TAPINS를 REX-10의 열수력 해석에도 적용하여, 반응도 삽입사고와 급수 증가사고 시 원자로계통의 거동을 예측하였으며 그 결과를 TASS/SMR의 해석과 비교하였다.

TAPINS의 검증 결과로부터, TAPINS 코드가 자연순환 방식으로 운전되는 일체형 원자로의 열수력 현상에 대해 신뢰성 있는 해석결과를 제공할 수 있음을 입증하였다. 특히, TAPINS가 이상 유동의 비평형 효과와 증기-가스 가압기의 과도 거동을 보다 정확성 있게 예측하는 데에 기여할 수 있을 것으로 판단된다.

주요어

REX-10, 완전피동 일체형 가압경수로, TAPINS 코드, Drift-flux 모델, 증기-가스 가압기 모델, RTF, 코드 확인 및 검증

학번: 2007-21260

감사의 글

부족한 점이 참 많았음에도 불구하고 많은 분들의 도움과 격려에 힘입어 이렇게 하나의 결실을 맺게 되었습니다. 6년 간의 쉽지 않았던 여정에 큰 힘이 되어주셨던 고마운 분들께 감사의 말씀을 전합니다.

스승으로서 큰 가르침 주시고 굳건한 믿음으로 제자의 성장을 이끌어주신 박군철 교수님께 진심으로 감사드립니다. 항상 칭찬과 격려로 저를 북돋아 주시고 큰 꿈을 품을 수 있게 도와주신 김응수 교수님께 깊은 감사를 드립니다. 엄정한 심사로 공학도로서의 자세를 깨우쳐 주신 이은철 교수님, 학부 시절부터 많은 관심을 가져주시고 선택의 기로에서 저를 이끌어주신 주한규 교수님, 인자한 웃음으로 많은 가르침과 귀중한 조언을 주신 정영종 부장님께도 진심으로 감사드립니다.

연구실에서 막내로 지내온 기간이 길었던 만큼, 우선 함께했던 선배들께 감사의 말씀을 드려야 할 것 같습니다. 후배들을 따뜻하게 대해 주시고 곧 학위를 마무리 하실 동운이형, 제가 닮고 싶은 연구자이자 학위과정 동안 항상 깊은 관심 주셨던 성진이형, 막히는 게 있을 땐 수화기를 들고 가장 먼저 찾았던 병언이형, 사수로서 함께 동고동락하며 많은 추억을 함께 나누었던 종원이형, 성실하고 차분한 모습으로 후배들에게 귀감이 되어주셨던 윤제형, 아이다호에서 새 도전을 시작한 수종이형, 다재다능한 능력과 예쁜 조카들과의 행복한 모습이 부러운 거형이형, 힘들 때 제게 가장 큰 힘이 되어주신 제 최고의 멘토 창용이형, 항상 제 고민을 귀 기울여 들어주시고 앞으로도 제가 충성을 다할 성수형, 남자다운 모습으로 연구실 분위기를 이끌어 주셨던 종수형까지 모두들 정말 감사드립니다.

학위와 팀장을 동시에 한다고 제게 많은 배려를 해 준 지금의 연구실 구성

원들에게 정말로 감사드립니다. 연구실에 큰 애착을 보여주시고 선박로 과제 하면서 함께 고생 많이 한 팀장 진석이형, 이제 자신이 즐길 수 있는 일을 찾아 새출발을 준비하는 태진이형, 항상 웃는 모습으로 연구실 분위기를 즐겁게 주도하고 제가 심적으로 가장 많이 의지했던 정훈이형, 술 한 잔에 마음 속 이야기와 인생상담을 나누었던 진화, 앞으로도 성실하고 순수한 선배로서의 모습이 기대되는 민섭이, 홍일점으로서 연구실 분위기를 부드럽게 만들어 주었던 민영이, 같이 과제하면서 학위 하느라 도움을 많이 주지 못해 미안한 일웅이, 연구든 생활이든 말 안 해도 알아서 척척 잘해서 나를 뒤돌아보게 만드는 아끼는 후배 동호. 대학원 생활하는 동안 최고의 연구실 분위기를 만들어 준 지금의 동료와 후배들 덕분에 무사히 학위를 마무리할 수 있었습니다.

졸업하고 사회에서 자리를 잡아가고 있는 준수형, 지훈이, 신국이, 수빈이 모두 앞으로도 좋은 일 가득하길 바랍니다. 함께 20대의 추억을 만들었던 03학번 동기들, 기쁜 일 슬픈 일 함께 나누는 평생 친구들인 BR 클럽의 정균, 봉권, 동현, 문규, 노주, 상주, 규철, 효석, 창봉, 같이 축구하면서 잊지 못할 순간들 함께 했던 동훈이형, 병호, 영섭 비롯한 네버스탑 식구들, TASS 해석 때문에 참 많이도 괴롭혔던 성원형, 친동생처럼 저를 잘 따라주었던 헌종이 모두들 정말 감사합니다.

오랜 시간 저를 기다려주면서 옆에서 큰 힘이 되어준 사랑하는 기선에게 특별히 고맙다는 말을 전하며, 앞으로 더 좋은 짝이 될 것을 약속합니다. 반대의 길을 걷는 형 때문에 항상 스트레스 많았을 텐데 긍정적인 모습으로 자신의 길을 걸어가는 사랑하는 동생 원건에게 앞날의 축복이 가득하길 기원합니다. 마지막으로 지금의 저를 있게 해 주시고 여태껏 자식을 위해 헌신하는 삶을 살아오신 사랑하는 아버지, 어머니께 이 논문을 바칩니다.